

NANOPOSITIVITY FORMATION IN AG-AU ALLOYS

by

Aziz Dursun

A dissertation submitted to The Virginia Polytechnic Institute and State University
in conformity with the requirements for the degree of

Doctor of Philosophy

in

Materials Science and Engineering

Sean Gerald Corcoran
Chair

William T. Reynolds

Stephen Kampe

Diana Farkas

Herve Marand

May 13, 2003
Blacksburg, Virginia

Keywords: dealloying, porous metals, critical potential, coarsening, surface diffusion

©Copyright, by Aziz Dursun

NANOPOSITIVITY FORMATION IN AG-AU ALLOYS

Aziz Dursun

ABSTRACT

Selective dissolution also known as dealloying is a corrosion process in which one component of a binary alloy system is selectively removed through an electrochemically controlled process which leads to the formation of a porous metal “sponge” with a porosity that is completely interconnected and random in direction.

Nanoporous metals are desirable since they have larger surface areas than an equal volume of non-porous material. Because of their enormous surface area per volume, these highly porous metal electrodes are superior materials for high surface area applications such as in biomedical devices, microfilters and catalysts.

Understanding the kinetic processes governing the development of porosity during dealloying and having ability to change the electrochemical conditions will allow us to better control over the average ligament size and distribution in porosity. The basic kinetic processes involved in the formation of these structures are related to such issues as environmental effects and electrochemical conditions on diffusion, microscopic coarsening phenomenon at room temperature and elevated temperatures, alloy passivation, and Gibbs-Thomson effects.

The average pore size and distribution was found to depend on the electrolyte composition, dealloying rate, applied potential and time. The porosity was found to significantly coarsen at room temperature during the dealloying process and this coarsening was highly dependent on the applied potential.

It is showed that the commonly accepted measurement of the critical potential for alloy dissolution calculated based on extrapolation of anodic polarization data results in an overestimation of this quantity. A series of constant applied potential experiments prove to be a more accurate method for critical potential determination.

To my mother and brother;

Melâhat
and
Ali Dursun

ACKNOWLEDGEMENTS

I would first like to express my deep gratitude to my advisor, Dr. Sean Gerald Corcoran for his invaluable guidance and inspiration throughout this study. Dr. Corcoran has educated, advised, and encouraged me in every possible way. Thank you very much for being so nice to me and keeping your door open every time I come to bother you. He has helped me develop my professional skills and I will emulate his drive and work ethic throughout my career.

I wish to thank my lab-mate, Dr. Dylan Pugh, group colleagues Douglas Crowson and Martha McCann and all my friends here at Virginia Tech for their friendships, experiences and encouragements during the pursuit of my degree.

A heartfelt acknowledgement goes out to my mother, Melâhat Dursun and my brother, Dr. Ali Dursun who has given me the courage and strength to make my dreams come true. I owe everything to them for what I have and for where I am now. The rest of my family has also been a large part of my success that I have experienced, through their love and support along the way.

I am equally indebted to each member of my thesis committee, Drs. Reynolds, Marand, Farkas and Kampe for their gracious participation.

I would also like to acknowledge Steve McCartney for helping me in getting SEM micrographs and John Barker for helping with SANS experiments.

I gratefully acknowledge the support of the National Science Foundation, Department of Materials Research.

TABLE OF CONTENTS

ABSTRACT	ii
ACKNOWLEDGEMENTS	vi
LIST OF TABLES	vii
LIST OF FIGURES	viii
CHAPTER 1 INTRODUCTION	1
1.1 Motivation.....	1
1.2 Research Aims and Methods.....	2
CHAPTER 2 BACKGROUND AND LITERATURE REVIEW	5
2.1 Dealloying (Selective Dissolution)	5
2.2 Thermodynamics of Selective Dissolution Process	10
2.3 Dealloying Mechanisms.....	11
2.3.1 Dissolution-Redeposition Mechanism.....	11
2.3.2 Volume Diffusion Mechanism.....	12
2.3.3 Surface Diffusion Mechanism	13
2.3.4 Percolation Model.....	17
2.4 The Critical Potential	22
2.4.1 Ambiguities in Defining the Critical Potential	23
2.4.2 Parameters affecting the Critical Potential.....	25
CHAPTER 3 EXPERIMENTAL.....	26
3.1 Electrochemical Treatment	26
3.2 Characterization of Samples Using Small Angle Neutron Scattering (SANS)	28
CHAPTER 4 DEALLOYING IN HALIDE CONTAINING ELECTROLYTES: EFFECT ON CRITICAL POTENTIAL AND PORE SIZE.....	32
4.1 Anodic Polarization Measurements.....	32
4.2 Morphology of Dealloyed Structures.....	38
4.3 What factors control the average pore size in a dealloyed structure?.....	41
4.4 Estimation of Surface Diffusivity of Gold in Halide Electrolytes	43
4.5 Effects of Halides on Critical Potential.....	43
CHAPTER 5 STEADY STATE METHOD FOR DETERMINING THE DEALLOYING CRITICAL POTENTIAL.....	46

5.1	Below the Critical Potential.....	47
5.2	Morphology Below the critical Potential.....	49
5.3	Current time Transients obtained in the Current Study	50
5.4	Morphology Above The “True” Critical Potential	58
CHAPTER 6 POTENTIAL DEPENDENT COARSENING OF POROUS AG-AU ALLOYS.....		69
6.1	Estimation of Surface Diffusivity of Gold as a Function of Dealloying Potential	69
6.2	Potential Dependent Coarsening of Porous Gold	74
6.2.1	System: Ag70Au30.....	74
CHAPTER 7 SUMMARY AND CONCLUSIONS		78
REFERENCES		82
APPENDIX A		89
VITA		107

LIST OF TABLES

Table 4-1 Critical dealloying overpotentials for $\text{Au}_{0.35}\text{Ag}_{0.65}$ and $\text{Au}_{0.30}\text{Ag}_{0.70}$ in 4 different media. The potentials in column 2 are with respect to NHE. The overpotentials, $\Delta E_{1.0\text{mA}/\text{cm}^2}$, are with respect to equilibrium potential for Ag as given in column 2.....	35
Table 4-2 Effect of electrolyte composition on the pore size for dealloyed $\text{Ag}_{0.65}\text{Au}_{0.35}$ as determined by cord length measurements of the micrographs shown in Figure 4-6. The surface diffusivity is calculated using equation (4.2).	41
Table 5-1 Critical Potentials values obtained using three different methods.....	56
Table 6-1 Effect of Dealloying Potentials on Surface Diffusivities for $\text{Ag}_{0.70}\text{Au}_{0.30}$ alloy. All samples are dealloyed in 0.1 M HClO_4 for the indicated time.	70
Table 6-2 Effect of Dealloying Potentials on Surface Diffusivities for $\text{Ag}_{0.65}\text{Au}_{0.35}$ alloy. All samples are dealloyed in 0.1 M HClO_4 for the indicated time	70
Table 6-3 Values of the Surface Diffusion Coefficients of Gold Adatoms Measured at Different Coarsening Potential Values, in the indicated solutions for $\text{Ag}_{0.30}\text{Au}_{0.70}$. ..	76

LIST OF FIGURES

Figure 1-1 The bi-continuous structure typical of dealloyed morphologies.	2
Figure 2-1 STM image of the resultant surface morphology of an $\text{Ag}_{0.16}\text{Au}_{0.84}$ alloy after selective dissolution of the Ag atoms in 0.1 M HClO_4	6
Figure 2-2 Schematic illustration of polarization behavior of a binary alloy as a function of composition, A_pB_{1-p} . Curve (1) and (2) are due to dissolution of A, and curve 3 to dissolution of B.	7
Figure 2-3 The bi-continuous structure typical of dealloyed morphologies. The fracture shows the isotropy of these structures	9
Figure 2-4 Cyclic voltammogram of Au in 0.1 M HClO_4 . Scan rate was 20 mV sec^{-1}	15
Figure 2-5 Two-dimensional illustration of percolation. At the precise composition shown, an infinite connected cluster of black atoms appears in the square lattice....	18
Figure 2-6 Current-potential behavior of the Ag–Au alloys in the 1 M $\text{AgClO}_4 + 0.1 \text{ M HClO}_4$ solution. No selective dissolution was observed for alloys containing less than 0.6 atom fraction silver. (Reproduced from [52] by permission of The Electrochemical Society, Inc).....	20
Figure 2-7 Current-potential behavior of the $\text{Ag}_{0.72}\text{Au}_{0.28}$ alloy in X M $\text{AgClO}_4 + 0.1 \text{ M HClO}_4$. (Reproduced from [52] by permission of The Electrochemical Society, Inc)	21
Figure 2-8 Summary of critical potentials as a function of the atom fraction of Au in the alloy for all alloys in X M $\text{AgClO}_4 + 0.1 \text{ M HClO}_4$. The points correspond to the data and the curves are fits using Equation (2.8). Reproduced from [52] by permission of The Electrochemical Society, Inc.	22

Figure 2-9 Schematic illustration of the current-potential behavior of pure metal “A” and “B” dissolution and the corresponding “ A_pB_{1-p} ” alloy dissolution. The dashed lines indicate the typical ambiguity in defining a critical potential.	24
Figure 3-1 The gold-silver phase diagram. (Adapted from Binary Alloy Phase Diagrams, 2nd edition, Vol. 1, T.B. Massalski, Editor-in-Chief, 1990)	28
Figure 3-2 Schematic drawing of the transmission geometry in SANS experiments.....	29
Figure 3-3 A typical SANS data for dealloyed Ag-Au alloy. The solid line is the fit obtained using leveled wave method of Berk.	30
Figure 3-4 Simulated two-dimensional slice of a three-dimensional porous structure calculated from the fits to the scattering data in Figure 3-3. The average Au ligament width calculated from the images is 11.2 nm. The black areas represent pure Au ligaments.	31
Figure 4-1 Potential dynamic scans of pure Ag, $Ag_{0.70}Au_{0.30}$ and pure gold in (a) 0.1 M $HClO_4$, (b) 0.1 M $HClO_4$ + 0.1 M KCl, (c) 0.1 M $HClO_4$ + 0.1 M KBr, and (d) 0.1 M $HClO_4$ + 0.1 M KI. Potentials were referenced to standard hydrogen scale in the indicated solutions.....	34
Figure 4-2 SEM photomicrograph showing silver salt film (AgBr in this case) formed on $Ag_{0.70}Au_{0.30}$ alloy surface after dealloying.....	35
Figure 4-3 Potential dynamic scans of $Ag_{0.70}Au_{0.30}$ in the indicated solutions. The potentials are referenced to equilibrium potential of Ag also in the indicated solutions. Scan rate is 3 mV/sec.	36
Figure 4-4 Potential dynamic scans of $Ag_{0.65}Au_{0.35}$ in the indicated solutions. The potentials referenced to equilibrium potential of Ag also in the indicated solutions. Scan rate is 1 mV/sec.	37

Figure 4-5 Current decay behavior for $\text{Ag}_{0.65}\text{Au}_{0.35}$ at (▼) 1.285 V vs. NHE in 0.1 M HClO_4 , (▲) 0.95 V in 0.1 M HClO_4 + 0.1M KCl, (●) 0.74 V in 0.1 M HClO_4 + 0.1M KBr, (■) 0.404 V in 0.1 M HClO_4 + 0.1M KI. 39

Figure 4-6 Scanning electron micrographs showing bio-continuous solid-void structure of $\text{Ag}_{0.65}\text{Au}_{0.35}$ after de-alloying at (a) 1.285 V vs. NHE in 0.1 M HClO_4 , (b) 0.95 V in 0.1 M HClO_4 + 0.1M KCl, (c) 0.74 V in 0.1 M HClO_4 + 0.1M KBr, (d) 0.404 V in 0.1 M HClO_4 + 0.1M KI. 40

Figure 5-1 Current decay behavior for $\text{Ag}_{0.70}\text{Au}_{0.30}$ held at the indicated potentials (vs NHE) in 0.1 M HClO_4 . The above data shows that the critical potential for this alloy is between 0.99 V and 1.02 V. The two sets of data taken at 1.04 V represent the typical reproducibility of the measurements. 52

Figure 5-2 Current decay behavior for $\text{Ag}_{0.75}\text{Au}_{0.25}$ held at the indicated potentials (vs NHE) in 0.1 M HClO_4 . The above data shows that the critical potential for this alloy is between 0.93 V and 0.94 V. 52

Figure 5-3 Current decay behavior for $\text{Ag}_{0.80}\text{Au}_{0.20}$ held at the indicated potentials (vs NHE) in 0.1 M HClO_4 . The above data shows that the critical potential for this alloy is between 0.79 V and 0.81 V. 53

Figure 5-4 Current-time transient for $\text{Ag}_{0.70}\text{Au}_{0.30}$ obtained at (a) 350 mV_{MSE} (b) 150 mV_{MSE} in 0.1 M HClO_4 54

Figure 5-5 Current-time transient for $\text{Ag}_{0.75}\text{Au}_{0.25}$ obtained at (a) 100 mV_{MSE} (b) 250 mV_{MSE} in 0.1 M HClO_4 55

Figure 5-6 Anodic polarization data for $\text{Ag}_{0.70}\text{Au}_{0.30}$ in 0.1 M HClO_4 . Scan rate = 1mV sec^{-1} . Region A (0.99 V – 1.02 V) corresponds to the identified region of the critical potential as determined by the potential hold data of Figure 5-1. Region B (1.1 V – 1.14 V) corresponds to the region of the critical potential determined by the extrapolation of the polarization data. 57

Figure 5-7 Anodic polarization data for $\text{Ag}_{0.75}\text{Au}_{0.25}$ in 0.1 M HClO_4 . Scan rate = 1mV sec^{-1} . Region A (0.93 V – 0.94 V) corresponds to the identified region of the critical potential as determined by the hold data of Figure 5-2. Region B (1.02 V – 1.06 V) corresponds to the region of the critical potential determined by the extrapolation of the polarization data. 57

Figure 5-8 Anodic polarization data for $\text{Ag}_{0.80}\text{Au}_{0.20}$ in 0.1 M HClO_4 . Scan rate = 1mV sec^{-1} . Region A (0.79 V – 0.81 V) corresponds to the identified region of the critical potential as determined by the hold data of Figure 5-3. Region B (0.85 V – 0.885 V) corresponds to the region of the critical potential determined by the extrapolation of the polarization data..... 58

Figure 5-9 Resultant morphology of $\text{Ag}_{0.70}\text{Au}_{0.30}$ after subjected to a potential of $1.04 V_{\text{MSE}}$ in 0.1 M HClO_4 59

Figure 5-10 Resultant surface morphology of $\text{Ag}_{0.70}\text{Au}_{0.30}$ after subjected to a potential of $0.79 V_{\text{MSE}}$ in 0.1 M HClO_4 60

Figure 5-11 Erlebacher simulation result showing integrated dissolution vs. time for $\text{Ag}_{0.75}\text{Au}_{0.25}$ and applied potentials between 1.2 eV and 0.85 eV. The true critical potential sits between 0.90 eV and 0.95 eV. 61

Figure 5-12 Charge density transients for $\text{Ag}_{0.75}\text{Au}_{0.25}$ obtained by integration of the current-time transients in Figure 5-2..... 61

Figure 5-13 Charge density transients for $\text{Ag}_{0.70}\text{Au}_{0.30}$ obtained by integration of the current-time transients in Figure 5-1..... 62

Figure 5-14 Charge density transients for $\text{Ag}_{0.80}\text{Au}_{0.20}$ obtained by integration of the current-time transients in Figure 5-3..... 62

Figure 5-15 STM Images of the resultant surface morphology of a $\text{Ag}_{0.16}\text{Au}_{0.84}$ alloy after selective dissolution of the Ag atoms in 0.1 M HClO_4 . Reprinted from [22] .. 64

Figure 5-16 Plateau current density as extracted from Figure 5-1 versus potential for $\text{Ag}_{0.70}\text{Au}_{0.30}$. Anodic polarization curve is also shown for comparison. The fit is exponential. 66

Figure 5-17 Plateau current density as extracted from Figure 5-2 versus potential for $\text{Ag}_{0.75}\text{Au}_{0.25}$. Anodic polarization curve is also shown for comparison. The fit is exponential. 66

Figure 5-18 Overpotential versus alloy composition data fitted to equation (4.3). 68

Figure 6-1 $\text{Ag}_{0.70}\text{Au}_{0.30}$ samples dealloyed at the indicated potentials in 0.1 M HClO_4 ...71

Figure 6-2 Small angle neutron scattering from porous $\text{Ag}_{0.70}\text{Au}_{0.30}$ alloy dealloyed at the indicated potentials in 0.1 M HClO_4 72

Figure 6-3 Small angle neutron scattering from porous $\text{Ag}_{0.65}\text{Au}_{0.35}$ alloy dealloyed at the indicated potentials in 0.1 M HClO_4 72

Figure 6-4 Small angle neutron scattering from porous $\text{Ag}_{0.70}\text{Au}_{0.30}$ alloy coarsened at the indicated potentials in 0.1 M HClO_4 75

Figure 6-5 Small angle neutron scattering from porous $\text{Ag}_{0.70}\text{Au}_{0.30}$ alloy coarsened at the indicated potentials in 0.5 M H_2SO_4 75

CHAPTER 1 INTRODUCTION

1.1 Motivation

Although this research did not focus on the practical applications of porous materials but the materials science of porosity formation, it will be good enough to give some examples, which encourages our efforts and make our studies worthwhile.

The important thing about porous materials is that they have enormous surface area per volume so that behavior of fluids in them is dominated by surface forces. And because of their enormous surface area, these materials have tremendous capacity to adsorb liquids and gases onto their surfaces, and they are widely used for scrubbing and separating chemicals, as microfilters in biological studies, and similar applications.

A recent study performed by Ertenberg et.al¹ showed that porous gold produced by selective leaching of silver from silver-gold alloys is a superior material for heat exchangers at microkelvin temperatures, where the relatively small surface area of sintered silver and the poor thermal conductivity of sintered platinum black present difficulties. It was reported that the surface area of these samples be $36 \text{ m}^2/\text{cm}^3$ from the BET(Brunauer-Emmett Teller) analysis of a methane adsorption isotherm at liquid-nitrogen temperature. This is about 4 times larger than the surface area of sintered silver.

Due to its large capacity to adsorb liquids and gaseous molecules onto its surface, porous gold has also been used in measurements of superfluid density and of heat capacity of ^4He in a study performed by Yoon^{2,3}.

Another promising application for nanoporous metals is high-surface area electrodes for biomedical sensing and stimulation. In the future, implantable electrode based biosensors will likely be used in closed-loop systems to control and regulate the levels of drugs in the body thus creating an artificial organ.

1.2 Research Aims and Methods

Selective dissolution (dealloying) is a corrosion process in which one or more elements are selectively removed from a binary alloy. In general dealloying can be electrochemically driven in any system as long as the dissolving element is greater than a critical composition and a large electrochemical potential difference exists between the alloying elements. It often results in development of a random interconnected porous network of the nobler element with a certain average ligament size in the range of a few nanometers to several micrometers.[See Figure 1-1].

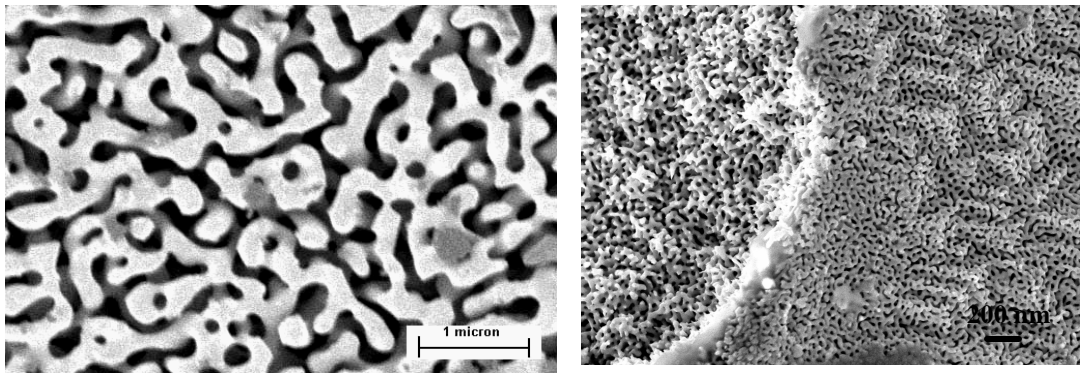


Figure 1-1 The bi-continuous structure typical of dealloyed morphologies. The fracture shows the isotropy of these structures

This bicontinuous metal-void structure is highly brittle in nature²⁸ and has been linked to stress corrosion cracking in many alloy systems^{4,5,6,7,8,9}. The seasonal cracking of α -brass in ammonia environments is perhaps the best example of stress corrosion cracking in which the selective dissolution plays an important role¹⁰. A recent study performed by Vukmirovic *et.al* showed that dealloying mechanism was indeed responsible for copper redistribution which in turn serves to enhance the kinetics of the corrosion process in copper containing aluminum alloys, such as Al2024-T3¹¹. Beyond its direct relevance to stress corrosion cracking and accelerated corrosion in Al2024-T3^{12,13}, interest in dealloying is relevant to the corrosion of austenitic stainless steel in acidified chloride containing electrolyte^{5,13} and the production of Raney Copper catalysts^{14,15}.

Although a great amount of research has been focused on the problem of stress corrosion cracking consequences of dealloyed structures, very little attention has been focused on the mechanisms and kinetics of porosity formation resulting from selective dissolution processes. The first detailed micro-morphological study of alloy dissolution was conducted by Forty *et al.* for the dealloying of Ag from Ag-Au alloys in nitric acid¹⁶. The TEM pictures of the dealloying in Au-Ag alloys showed that the morphology is qualitatively similar to the morphology seen in vapor deposition of metals such as gold on glass and that obtained by a spinodal decomposition process. In fact, the small angle neutron scattering from structures obtained through leaching of one phase of a spinodally decomposed system (e.g. porous Vycor) is quantitatively similar to that of dealloyed Au^{17,18,19}.

The mechanism of structural instability that leads to porosity formation has been the focus of recent investigations. The studies performed by other investigators support the idea that the morphology of porous metals is controlled by a competition between a surface roughening process (selective dissolution of one of the alloying element) and a surface smoothing process (mass transport of the remaining element by surface diffusion, volume diffusion, or dissolution/redeposition). The rates of both kinetic processes are affected by the electrochemical conditions. For example, the specific adsorption of the complexing ions from the electrolyte will alter the surface diffusivity. Therefore one can tailor the morphology of the resultant structure by controlling the electrochemical environment.

The physical processes that control the formation of 3-D interconnected porous structures resulting from selective dissolution remain obscure. If we can understand the kinetic processes governing the formation of porosity, we believe we can tailor not only the average pore size but also the distribution in sizes. This will give us an opportunity to change the mechanical properties of the structures as well as their “size-selectivity” to diffusing species, which will in turn affect a wide range of scientific and technological fields. For example, lifetime predictions of the corrosion resistance of various metallic alloys used in engineering structures depend on an accurate knowledge of the dealloying

kinetics. On the other hand, knowledge of the dealloying kinetics will be useful in order to apply this technique for the construction of 3-D porous structures.

The main objective of this research was to develop a basic mechanistic understanding of the electrochemical and physical conditions, which result in the formation of dealloyed bicontinuous structures in order to tailor the structures for potential applications in areas such as filtration and biomedical sensors. This objective will be met by characterizing the 3-D morphology of porosity formed under controlled conditions designed to change the relative rates of roughening and smoothing processes.

Specifically we studied

- 1) The coarsening kinetics of porous metals as a function of electrochemical environment, applied potential and alloy composition.
- 2) The range of length scales that can be obtained in porous metals through modifications to the surface diffusivity at room temperature. For this purpose we studied (a) potential dependence of diffusivity (b) electrochemical environment dependence of diffusivity
- 3) the critical potential for $\text{Au}_{0.20}\text{Ag}_{0.80}$, $\text{Au}_{0.25}\text{Ag}_{0.75}$ and, $\text{Au}_{0.30}\text{Ag}_{0.70}$ alloy systems and proposed a unique method that rules out the polarization curve .

This thesis is organized in the following manner. Chapter 2 represents a comprehensive review of selective dissolution and its mechanisms. Critical potential has been introduced and the ambiguities in determining the critical potential have been addressed in detail under a separate heading. Experimental procedure including the SANS data analysis has been explained in Chapter 3. Results and Discussion are presented in Chapter 4, 5 and 6. Conclusions are presented in Chapter 7.

CHAPTER 2 BACKGROUND AND LITERATURE REVIEW

2.1 Dealloying (Selective Dissolution)

Dealloying is defined as the selective electrolytic dissolution of one or more components from a homogeneous binary solid solution.

There are two general requirements for an alloy system to undergo selective dissolution which leads to the formation of a porous sponge with a porosity that is completely interconnected and random in direction. Firstly, the metal/metal ion electrode potential of the alloy components must differ considerably. One element is thus more noble (MN) and the other is less noble (LN). For instance, in the Ag-Au system where Au and Ag are the more and less noble elements respectively, the difference in the standard electrode potentials of Ag and Au is: $E_{Au^{3+}/Au} - E_{Ag^+/Ag} = 0.80$ Volt. This difference in the electrode potentials of the components results in anodic dissolution of the components at different rates. The MN component (in our case Au) remains insoluble in most of the environments as long as the applied potential does not noticeably exceed the equilibrium potential of the nobler element. Considering the difference in their equilibrium electrode potentials, we can expect dealloying in Au-Cu alloys, but not in Au-Pt alloys. Secondly, for selective dissolution to occur, dealloyable systems should have a certain composition of MN element above which selective dissolution does not occur. For alloys below this critical dealloying composition, the LN element will be removed from the first few atomic layers of the surface resulting in an enrichment of MN and the slowing and/or shutting off of the dissolution process. For example, the critical dealloyed composition is 18a/o²⁰ Cu for Zn (MN)-Cu (LN) and, 60a/o Ag for the Au-Ag²¹ system. Corcoran²² used in-situ scanning tunneling microscopy (STM) to characterize the morphological evolution of Ag-Au alloys below the critical dealloying composition.

Figure 2-1 shows the resultant surface of an $Ag_{0.16}Au_{0.84}$ alloy after selective removal of Ag in 0.1 M $HClO_4$ electrolyte²². As it is seen from the figure, the selective dissolution of Ag is confined to the first few atomic layers of the alloy. One can easily

count 3-4 exposed atomic planes. Each atomic plane shows up as a distinct gray level; the lighter shading corresponds to planes that are at higher heights on the surface.

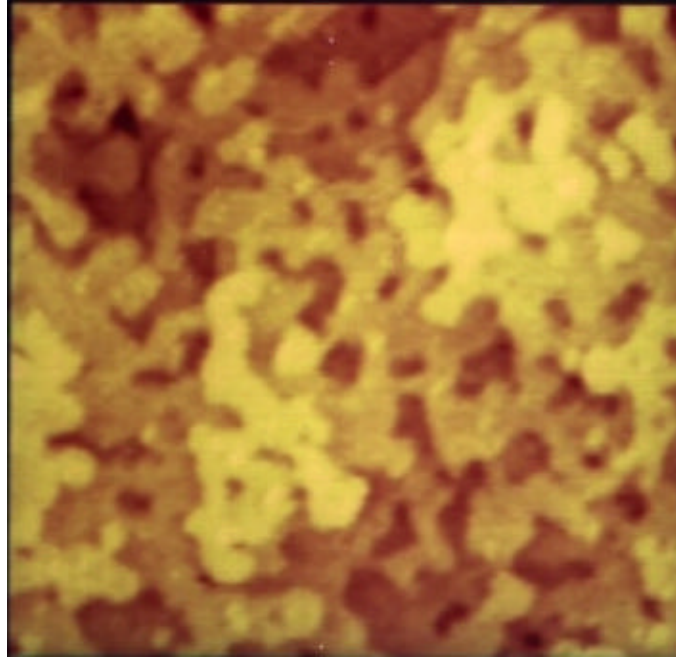


Figure 2-1 STM image of the resultant surface morphology of an Ag_{0.16}Au_{0.84} alloy after selective dissolution of the Ag atoms in 0.1 M HClO₄.

Alloy systems that share the aforementioned requirements includes Cu-Ni²³, Zn-Cu^{23,24}, Mn-Cu²³, Pd-Cu²⁵, Cu-Al^{1,15}, Cu-Au^{24,26}, Mg-Cd²⁷ and Au-Ag^{16,28,29,30}. The reduction of titanium dioxide in molten calcium chloride also meets these requirements^{31,32}.

A typical electrochemical dissolution experiment involves ramping the overpotential at a fixed rate and simultaneously measuring the (anodic) dissolution current. For a binary alloy of composition A_pB_{1-p}, with A being the LN component, a schematic of a typical potentiodynamic polarization curve is given in Figure 2-2. The current response of such a binary alloy under applied potential in electrolyte is characterized by four distinct regimes of behavior, all of which depend on the alloy composition and the difference in the standard potentials of the metals.

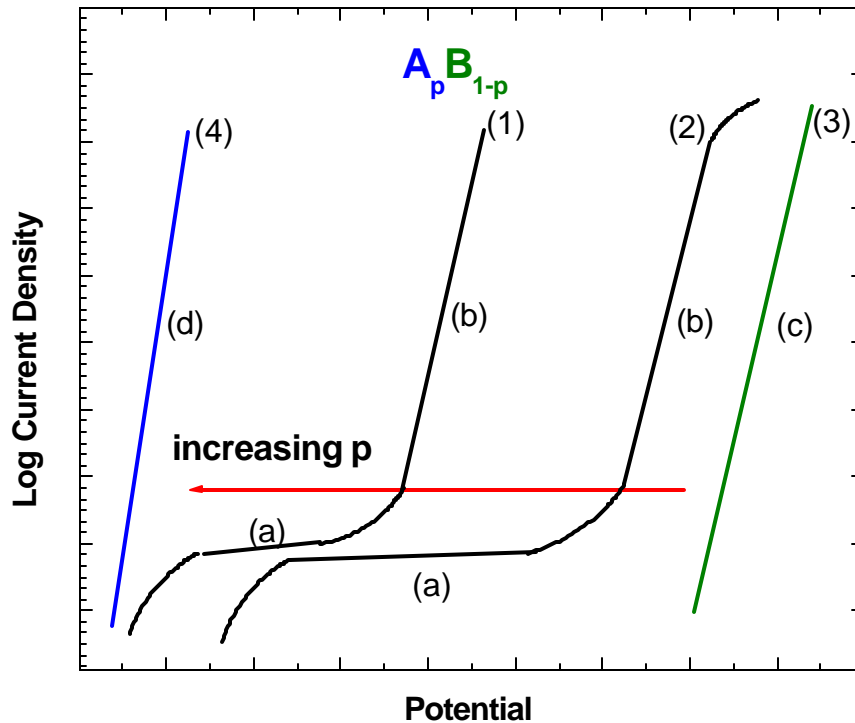


Figure 2-2 Schematic illustration of polarization behavior of a binary alloy as a function of composition, $A_p B_{1-p}$. Curve (1) and (2) are due to dissolution of A, and curve 3 to dissolution of B.

The first increase in the current density (corrosion rate) with the potential prior to region (a) is associated with dissolution of the less noble metal A from the kink sites where atoms are at least firmly bonded to the neighboring atoms. After the A atoms at the surface are exhausted and B atoms cover the surface by diffusion, an anodic limiting current density is observed. Either surface diffusion of B or volume diffusion of A have been proposed as the current limiting mechanisms^{33,34,35}. Those mechanisms will be reviewed in the following paragraphs. If the alloy is polarized to higher potentials, however, the region of roughly constant current plateau (passivation) is terminated and the current density of less noble metal dissolution increases by several orders of magnitude (region (b)), which result in an interconnected 3-D porosity in the solid as shown in the Figure 2-3. The threshold potential that marks the transition from region a to b is defined as the critical potential. The critical potential itself is shifted in the anodic

direction by increasing the noble metal concentration. Finally, at electrode potential greater than the critical potential, a second plateau of the polarization curve is observed which may be associated with the formation insoluble corrosion products.

Pickering³⁶ has identified three types of potential dependent behaviors for binary alloys in terms of: (i) tendency for selective dissolution (curve d), (ii) surface enrichment of the nobler component (curve a) and (iii) the stability of a planar surface (curve c). The alloys which are very rich in A, show region (d) type of behavior. A general type of attack similar to what would be expected from pure A is characteristic of region (d). As the concentration of B in the alloy increases, a low current potential-independent dissolution behavior develops, labeled as region (a) in curves (1) and (2). Pickering refers to the polarization curves, which contain regions (a) and (b) as Type I. A well-known example of Type I dissolution occurs in the Ag-rich Ag-Au alloy system and is of general interest in this research.

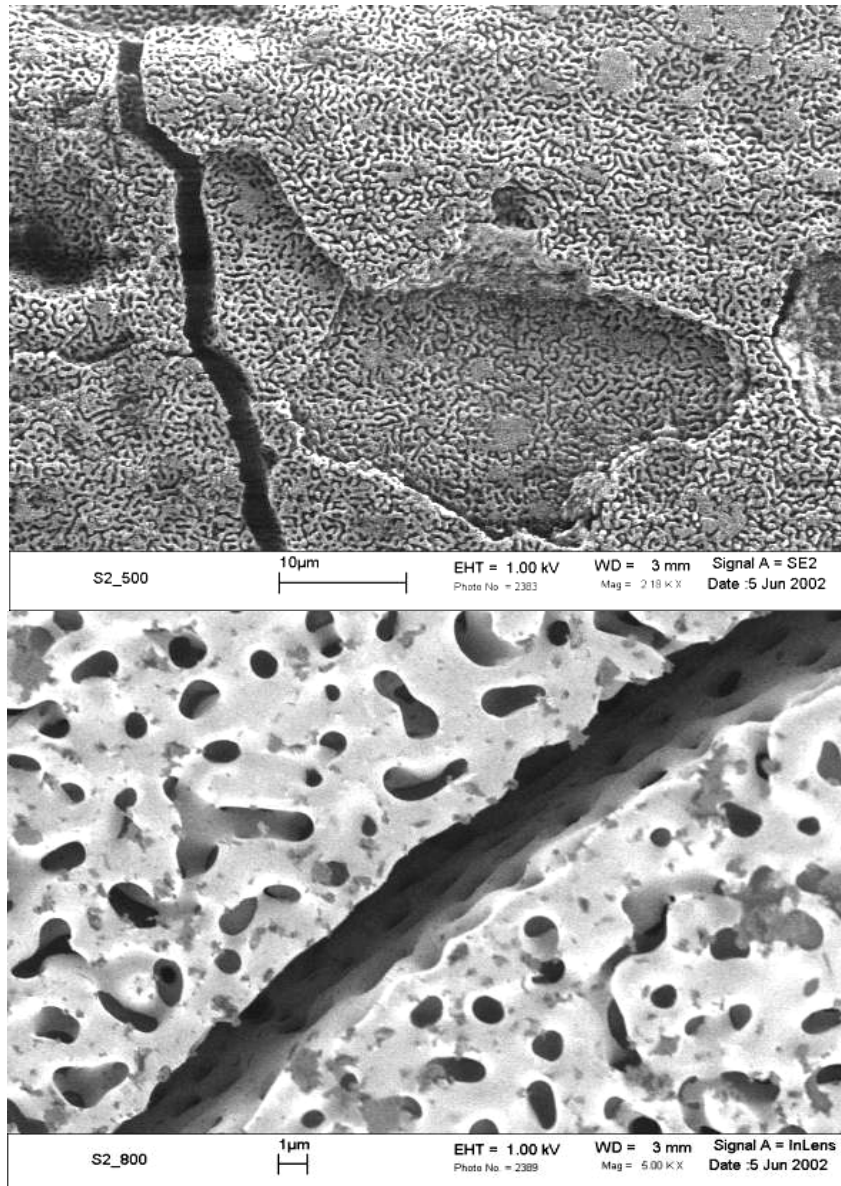


Figure 2-3 The bi-continuous structure typical of dealloyed morphologies. The fracture shows the isotropy of these structures

2.2 Thermodynamics of Selective Dissolution Process

Binary solid solutions are phases with individual thermodynamic properties, and one may expect their anodic dissolution, being the oxidation of components, in proportion to their chemical composition. The partial Gibbs free energies of the components decrease when they form an intermetallic phase. In the case of a perfect solid solution, such a decrease per mole of the i th component is given by:

$$\Delta G = RT \ln N_i \quad (2.1)$$

where N_i is the mole fraction of the component. As $\Delta G = -nF\Delta E_i$ (Energy = charge passed \times reversible potential difference, where $\Delta E_i = \bar{E}_i - E_i^\circ$ is the difference between the equilibrium electrode potential of the i^{th} component in the alloy and the corresponding potential of the same component in the individual phase), one can write

$$\Delta E_i = -\frac{RT}{n_i F} \ln N_i \quad (2.2)$$

By definition N_i is less than 1, so that $\Delta E_i > 0$, which means that the partial potentials of the alloy components are always more positive than the corresponding potentials of the individual metals. Consequently, dissolution of metals from alloys should also start at more positive potentials. This behavior can be seen in Figure 2-2. The anodic polarization curve for pure A is shifted to more positive potentials when it is alloyed with a component B. Taking into account equation (2.1), the difference between the partial potentials of the components in an alloy A-B type can be written as

$$\Delta E_{A,B} = E_B - E_A = -\frac{RT}{F} \ln \frac{N_B}{N_A} \quad (2.3)$$

Thus, the partial electrochemical properties of the alloy components virtually always differ, and there is always a nonzero thermodynamic probability of the predominant selective dissolution of the electronegative metal from the alloy.

2.3 Dealloying Mechanisms

One of the fundamental questions regarding the formation of porous metals is the mechanism by which the selective dissolution process is maintained over more than a few atomic layers leading to the 3-dimensional porous structures shown in Figure 2-3. The mechanism of dealloying has been the subject of considerable discussion in the literature^{30,37,41,49}. Several models have been proposed to explain the selective dissolution process resulting in a porous dealloyed layer with a certain average pore size. Following is a review of those mechanisms with considerable attention paid to the percolation model which to date is the only model that seems consistent with experimentally observed behaviors.

2.3.1 Dissolution-Redeposition Mechanism

For a binary alloy with A_pB_{1-p} , A being the LN component, this mechanism assumes an initial simultaneous dissolution of both components and redeposition of the nobler component B. It was one of the first mechanisms proposed for the dezincification of brass where both Cu and Zn dissolve into the electrolyte at different rates followed by redeposition of Cu at more cathodic sites^{38,39}. This model was thought to be necessary to explain how dealloying could be maintained over macroscopic depths. This mechanism, however, is not a necessary condition for dealloying observed over a wide range of systems. For instance, in both Au and Pt based systems at potentials where only selective removal of the less noble component occurs, dissolution of both Au and Pt can be thermodynamically discounted as explained before.

It is worth adding that dissolution of MN metal from the alloy may occur at values less than the standard equilibrium electrode potential of the pure MN due to curvature effects. This phenomenon is called “underpotential dissolution” In the initial

stages of dealloying, selective dissolution of Ag leaves regions of very high positive curvature, k , of the MN metal (Au) that can dissolve at an under potential given by the Gibbs-Thomson relationship:

$$\Delta E \cong \frac{g\Omega}{nq} k \quad (2.4)$$

where g is the isotropic solid/electrolyte interfacial surface free energy, Ω is the atomic volume, k is the curvature ($= 1/r$ where r is the radius of the initial curvature of the bicontinuous dealloyed structure), n is the number of electrons transferred per atom. For parameter values of Au(MN), $g = 1 \text{ J m}^{-2}$, $\Omega = 1.685 \times 10^{-29} \text{ m}^3$, $n = 1$, $q = 1.602 \times 10^{-19} \text{ Coul}$, and $r = 3 \times 10^{-9} \text{ m}$, we get a change in the equilibrium potential, ΔE of 33 mV.

Even though the above mechanism, which requires the ionization of an electropositive component at potentials far below its equilibrium potential (e.g., at an underpotential of about 0.6 V for Cu-13Au), is generally impossible, under certain electrochemical conditions (small underpotential conditions), particularly for alloys with a small separation of critical potential and equilibrium electrode potential, this mechanism could still play a role in some alloy systems (such as the Cu-rich brasses).

2.3.2 Volume Diffusion Mechanism

The volume diffusion mechanism was first introduced by Pickering and Wagner⁴⁰. This mechanism does not consider an “underpotential dissolution” of the MN component due to curvature effects. Instead the MN atoms are assumed to accumulate as mobile adatoms on the electrode surface due to formation of surface vacancies created by preferential removal of the less noble component either from kink or terrace sites. The major concept of the volume diffusion mechanism is that by the injection of surface vacancies and divancies into the crystal volume below the surface, a large vacancy supersaturation beyond the thermodynamic equilibrium concentration is developed adjacent to the alloy/electrolyte interface, which results in an enhanced diffusion of the

LN element toward the surface and the MN element away from the surface owing to the compositional gradients created by the selective removal process. Wagner⁴¹ demonstrated that if the volume diffusion controls the rate of dealloying, then geometrical instabilities will develop along the planar interface, which will grow rapidly with time. This instability is accounted for the sponge-like morphology observed in dealloyed systems.

The inherent problem with this mechanism is that at room temperature the rate of transport of the LN element to the surface is not sufficient to support the dealloying current densities ($>10 \text{ mA cm}^{-2}$) observed experimentally. The upper bound calculation of Pickering and Wagner based on a divacancy diffusion mechanism can support currents as high as 0.2 mA cm^{-2} corresponding to a divacancy diffusivity of $10^{-12} \text{ cm}^2 \text{ sec}^{-1}$. However, both the diffusivity and the mole fraction of divancies (10^{-2}) needed to support a current of 0.2 mA cm^{-2} are extreme assumptions. The diffusivity is many orders of magnitude higher than the bulk alloy diffusivity at $25 \text{ }^\circ\text{C}$. In addition, the divacancy mole fraction (10^{-2}) is 100 times larger than the equilibrium mole fraction of monovacancies just below the melting point of a metal.

The model also does not seem to support experimentally observed compositional dependences of the dealloying current, critical compositional thresholds for dealloying, and the prediction of a critical potential.

2.3.3 Surface Diffusion Mechanism

The surface diffusion model as proposed first by H.Gerisher⁴² involves the nucleation and growth of nuclei of the pure, or almost pure, MN component via a surface diffusion process. The model as it is originally proposed assumes that there is no transport of LN atoms to the electrode surface via volume diffusion. As the LN element is selectively dissolved from the surface of the alloy, the remaining MN element, which is now in a highly disordered state begins to reorder by surface diffusion resulting in nucleation and growth of gold-rich islands possibly at preferred surface sites such as structural fault boundaries, micro-twins and slip steps.

H.Gerisher developed a theoretical analysis and concluded that there is a time dependence of the partial current density of LN atom. For atomic fractions, $X_{MN} < 0.5$, the current density transient has been assumed to be given by

$$i_{LN}(t) \propto \left(\frac{1}{t}\right)^{X_{MN}/(1-2X_{MN})} \quad (2.5)$$

Theoretically, it is expected that after removal of the LN metal from kink sites where atoms are at least firmly bound and terrace sites which requires a greater activation energy (overpotential) in the surface steps, eventually the alloy becomes completely passivated when all the surface sites are occupied by MN metal. However, this is clearly contrary to practical experience, from which we must infer that this simple model of selective dissolution is incorrect. Therefore alternative mechanisms were suggested first by A.J Forty³³ and later by K.Sieradzki³⁰.

Forty et.al proposed that both volume and surface diffusion are of importance in the selective dissolution process. It is believed that selective dissolution of the LN specie of an alloy should lead to the creation of surface vacancies. These vacancies can then migrate across the surface to form pits, steps and other surface roughening features, or they can assist the migration of the residual MN atoms which leads to island growth. The coalescence of these islands by migration of more MN atoms exposes fresh alloy to the corrosive environment where further dissolution will occur leading to the formation of deep pits and tunnels. Those surface vacancies can also diffuse into the underlying alloy to assist volume diffusion of the less noble metal at the corroding surface.

A study performed by Durkin and A.J. Forty¹⁶ revealed that the surface diffusivity of Au atoms required to account for the kinetics of island growth must be several orders of magnitude greater than the value expected for Au at RT. Based on the detailed analysis of the electron diffraction patterns of $Ag_{0.75}Au_{0.25}$, the authors proposed that oxidation and solvation of gold atoms might well provide a mechanism for such rapid diffusion. Based

on the fact that the dealloying potentials are well below the potentials of gold oxidation, which occurs as high as 1.5V vs NHE (See Figure 2-4), the authors proposed that the oxidation of gold is lowered during the selective dissolution of Ag as a result of a change of chemical environment.

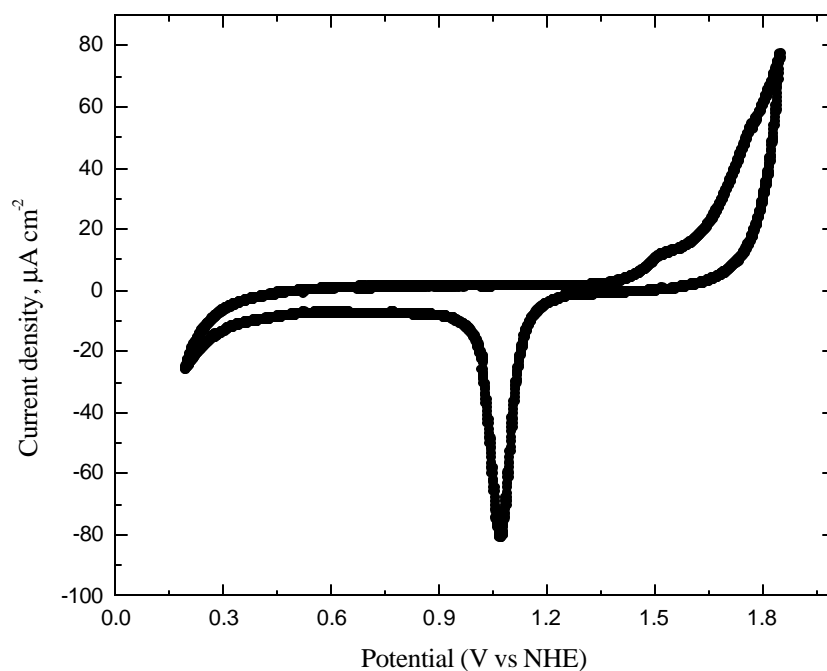


Figure 2-4 Cyclic voltammogram of Au in 0.1 M HClO₄. Scan rate was 20 mV sec⁻¹.

It is interesting that the island-channel-pit morphology was found only for Ag-Au alloys containing between 20 and 50 atomic percent gold. Based on the model developed by Forty et.al³³ it is explained as follows: in silver rich alloys, island nucleation is difficult due to the relatively small concentration of residual gold atoms, whereas, in gold rich alloys, the residual atoms being more densely packed, migrate across the surface less easily. Therefore, it is found from this simple corrosion model that those alloys containing less than 50 a% gold atom will continue to undergo selective dissolution if surface diffusion is the controlling mass transport process. On the other hand Sieradzki⁴⁹ explained the limitation in the amount of MN element by percolation model, in which the

surface diffusion model was extended to account for pre-existing interconnected paths of like elements in the binary alloy and was later extended to include curvature effects on the dissolution potential^{30,52}.

A combination of surface and volume diffusion leading to a geometrical instability of the surface during selective dissolution was also proposed by Harrison and Wagner⁴³.

The most common argument against this model is that the mechanism for sustained 3-dimensional porosity development is not clear. The model would predict an enriching MN element at the surface eventually shutting off the dealloying process and complete surface passivation. The calculations of Forty and Rowlands⁴⁴ predict the formation of pits in the alloy surface but also predict the continual decreasing of the pit radius with time at which the dealloying process ceases. This even gets worse if one consider higher surface diffusion rates with additions to the electrolyte of ions. This prediction is so far in conflict with our initial results that show significant increase in the overall diameter of the porosity owing to increase in the surface diffusion of MN metal by addition of halides to the electrolyte⁴⁵. The details of this study will be given in the forthcoming chapters. From our experimental data, it appears that the dealloying process could be maintained indefinitely.

2.3.4 Percolation Model

It was proposed by Sieradzki et.al⁴⁹ to explain the selective dissolution process. This model extends the surface diffusion model to include the importance of the atomic placement of atoms in a randomly packed way in the solid. At the present time, it is the most promising model because it can account for certain features of dealloying including critical potential thresholds for dealloying, compositional dependence of the critical potential, and the formation of a 3-D bicontinuous dealloyed morphology.

A critical composition of the LN (or MN) element, which is required for selective dissolution process to occur, has been mentioned in the previous paragraphs. Sieradzki et.al⁴⁶ have shown that there exists a critical concentration of Zn (18 + 2 at.%) in Zn-Cu alloys and Al (14 + 2 at.%) in Al-Cu alloys below which de-alloying does not occur. Based on the fact that these experimentally determined critical compositions are quite close to the fcc lattice site percolation thresholds (19.8%)⁴⁷, Sieradzki developed the percolation model.

The model suggests that the selective dissolution process is possible only if a continuous path of the more electrochemically active element (percolating cluster) exists throughout the thickness of the solid. (Figure 2-5)

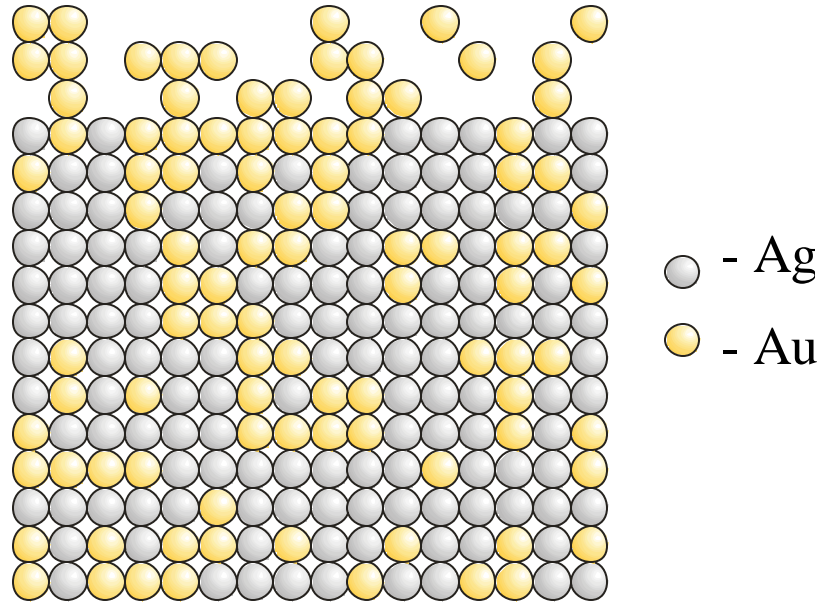


Figure 2-5 Two-dimensional illustration of percolation. At the precise composition shown, an infinite connected cluster of black atoms appears in the square lattice.

In this case, transport of the LN component to the surface by volume diffusion is not necessary for dealloying. The interconnected paths of the more active element along with the surface-diffusion-controlled coarsening process, known in the metallurgical literature as Ostwald ripening, provide continuous active pathways for electrolyte penetration into the solid. After the entire less noble element is removed, the resulting structure is a porous network of the nobler element with a certain average ligament size in the range of a few nanometers to several micrometers.

It was proposed by Sieradzki^{30,49} that surface morphology is controlled by the competition between the curvature dependent dissolution of the less noble element causing roughening and surface diffusion of the more noble metal, which tends to result in smoothening. This analysis also provides a basis for understanding the critical compositions that are not consistent with the conventional percolation thresholds such as in Ag-Au alloy systems. The deviations from the theoretical thresholds have been

attributed to the short-range ordering and surface diffusion of the MN metal alloy constituent as the LN metal is selectively dissolved out.

An expression (equation (2.8)) has been developed for the critical overpotential by combining the high field approximation of the Butler-Volmer (BV) equation (2.6) which describes how the dissolution current density or flux is related to the overpotential, and the results of Mullins⁴⁸(equation (2.7)) describing the rate at which surface roughness disappears by curvature driven surface diffusion :

$$J^{diss} = i_o \left[e^{\frac{ah}{kT}} - e^{\frac{(1-a)h}{kT}} \right] \quad (2.6)$$

$$J^{diff} = \frac{D_s N_s g \Omega}{kT} \frac{\partial^3 y}{\partial x^3} \quad (2.7)$$

$$\bar{h}_{crit} = 2 \frac{d}{a} \frac{g}{2-g} + \frac{2k_b T}{nq} \text{ArcSinh} \left[\frac{p^2 g \Omega}{nqd} \frac{D_s N_s}{J_o a^2} \left(\frac{g}{2-g} \right)^2 \right] \quad (2.8)$$

Where g is the atom fraction of Au in the alloy, k_b is the Boltzmann constant, T is the absolute temperature, n is the number of electrons involved in the dissolution process, q is the charge of an electron, g is the surface energy, Ω is the atomic volume, D_s is the surface diffusivity, N_s is the surface density of atoms, J_o is the mass flux associated with the exchange current density in units of #atoms $\text{m}^{-2} \text{sec}^{-1}$, a is the nearest neighbor distance, and d is a fitting parameter related to the compositional variation across the alloy surface.

The above equation neglects bulk diffusion and dissolution-redeposition of the nobler element. The predicted behavior of critical potential as a function of composition agrees well with that of Tischer and Gerischer²¹. This equation has been tested for a series of Ag-Au alloys as a function of alloy composition and electrolyte composition⁵². For the Ag-Au system the variables in the above equation are: $W = 1.685 \cdot 10^{-29} \text{ m}^3$, $q = 1.602 \cdot 10^{-19} \text{ C}$, $n = 1$, $a = 2.880 \cdot 10^{-10} \text{ m}$, $k_B = 1.381 \cdot 10^{-23} \text{ J K}^{-1}$, $N_s = 1.395 \cdot 10^{19} \text{ m}^{-2}$ for the (111) surface, $D_s = 2 \cdot 10^{-13} \text{ m}^2 \text{ sec}^{-1}$, $T = 298 \text{ K}$, and $\gamma \cong 1 \text{ Jm}^{-2}$. This leaves δ and J_o as fitting parameters. The alloy composition changes the value of the percolation cluster size, ξ_a , where it is defined as $\xi_a = \frac{(1+p)a}{1-p}$, p is the fraction of dissolving species “A” and equal to $1-g$, while the electrolyte composition varies the exchange current density, i_o ($i_o = J_o n q$). Figure 2-6 and Figure 2-7 show the experimentally measured I-V relationships as a function of alloy composition and electrolyte composition, respectively.

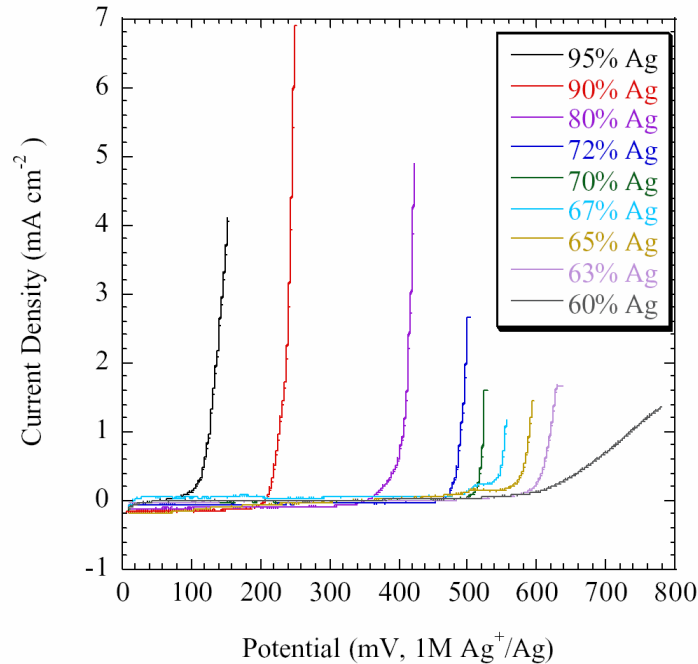


Figure 2-6 Current-potential behavior of the Ag–Au alloys in the 1 M $\text{AgClO}_4 + 0.1 \text{ M HClO}_4$ solution. No selective dissolution was observed for alloys containing less than 0.6 atom fraction silver. (Reproduced from [52] by permission of The Electrochemical Society, Inc)

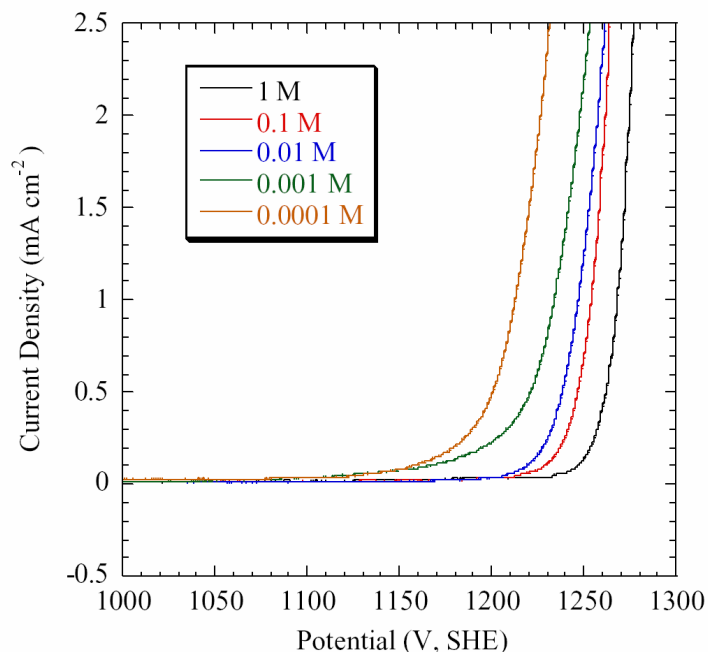


Figure 2-7 Current-potential behavior of the $\text{Ag}_{0.72}\text{Au}_{0.28}$ alloy in $X \text{ M AgClO}_4 + 0.1 \text{ M HClO}_4$. (Reproduced from [52] by permission of The Electrochemical Society, Inc)

The authors defined the critical potential as the value of the potential at which the current reaches a value of 1 mA cm^{-2} . Figure 2-8 summarizes this data for the electrolyte of $X \text{ M AgClO}_4 + 0.1 \text{ M HClO}_4$ and shows the fit to the data using equation (2.8).

One big flaw in an attempt of fitting of the above equation to the data is the value of D_s . The authors claim that the equation remarkably fits the experimental data. However, the surface diffusion coefficient used in the above equation is 7 orders of magnitude greater than that of our experimentally determined diffusion coefficients. In the following chapters we will attempt to fit our experimental data (critical potential, and D_s values) to the above equation.

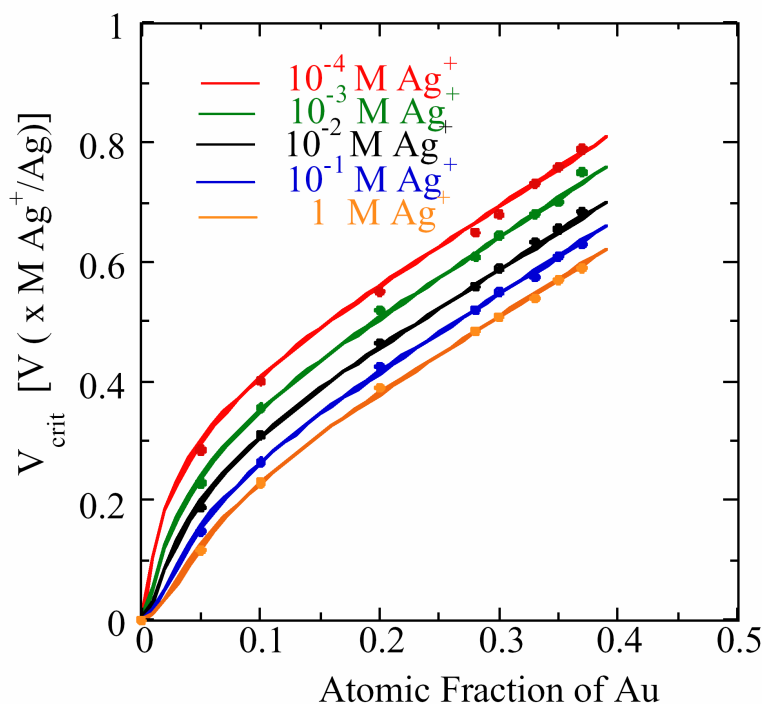


Figure 2-8 Summary of critical potentials as a function of the atom fraction of Au in the alloy for all alloys in X M $\text{AgClO}_4 + 0.1$ M HClO_4 . The points correspond to the data and the curves are fits using Equation (2.8). Reroduced from [52 by permission of The Electrochemical Society, Inc].

2.4 The Critical Potential

In some cases, an alloy does not undergo selective dissolution below a certain potential known as critical potential, even if it meets the requirements for dealloying. Critical potential is one way to measure the susceptibility of an alloy to selective dissolution. It can simply be defined as the onset of selective dissolution which is characterized by an abrupt increase in the current density on the quasi-steady-state $\log i_A$ vs. E curve at potentials higher than critical value. See Figure 2-9.

Sieradzki⁴⁹ offered two interpretations for the critical potential. According to the first definition, critical potential (E_c) is determined by the competing kinetics of curvature dependent dissolution (roughening) and that of surface diffusion smoothening. Depending on the relative rates of these processes, surface diffusion may act to passivate the surface or unblock dissolution sites. According to this description, E_c can be defined

as the transition point at which the curvature driven surface diffusion of the MN metal resulting in a surface smoothening shift to the dissolution of the more active component leading to surface roughening.

According to the second explanation, E_c is determined by the number and type of the nearest neighbors of the LN element. Alloys richer in the more active element will have larger high density clusters of this type of atom, and the dissolution potential will be lower, i.e. E_c decreases with increasing mole fraction of less noble elements. Therefore, E_c is the potential required to dissolve the largest percolating cluster that exist in the alloy.

The dealloying process has most recently been treated as a kinetically controlled morphological transition⁵² and as a phase separation process⁵⁰. At potentials below the critical potential the noble component covers the active dissolution sites leading to surface diffusion-limited current density and thereby a macroscopically flat surface. Above the critical potential, on the other hand, the rate of dissolution overcomes the rate of surface diffusion of noble component and the current increases steeply with the potential.

2.4.1 Ambiguities in Defining the Critical Potential

There are some ambiguities in defining the critical potential (CP) from anodic polarization curves. Figure 2-9 is a typical alloy polarization curve that reveals these ambiguities. The critical potential is taken as either the onset of the rapid rise in the current with potential, $E_{\text{critical-2}}$, or the “knee” in the polarization curve, $E_{\text{critical-1}}$.

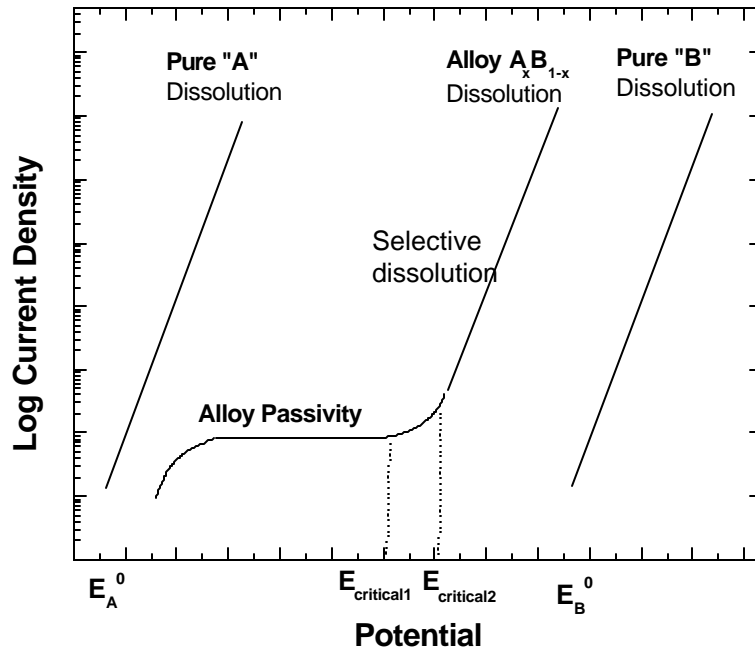


Figure 2-9 Schematic illustration of the current-potential behavior of pure metal “A” and “B” dissolution and the corresponding “ A_pB_{1-p} ” alloy dissolution. The dashed lines indicate the typical ambiguity in defining a critical potential.

After a study performed by Pickering³⁶ in 1983, it is generally accepted that the critical potential is determined by locating the onset of the rapidly rising current through extrapolation to the baseline current of the passivation region. Both the value of the critical potential obtained by this method, which we will refer it as E_c for the rest of the thesis, and that determined by two methods mentioned above is not very well defined and raises some questions due to the nature of the experimentally determined anodic polarization scans. Our anodic polarization curves for Ag-Au alloys revealed that there is not a very well defined plateau current of the passivation region. In addition to that, since current rises exponentially according to equation (2.6) beyond the critical potential, extrapolating a line through the onset of the rapidly rising current will create unavoidable errors in determining the exact CP. A recent study done by Sieradzki⁵² also showed that E_c is very sensitive to the rate of application such as the potential sweep rate used to generate the polarization data. It means that the amount of time an alloy sits in a

particular potential range during a potential sweep is actually quite important. The authors reported as much as 170 mV shift in the CP for a change of $\sim 300 \text{ mV s}^{-1}$ in scan rate.

This thesis proposes a more accurate method for the determination of the critical potential in binary alloys. This method eliminates the ambiguities in defining the critical potential based on anodic polarization curves that arise owing to the sensitivity of alloy polarization data on scan rate. The method is explained in detail in Chapter 5.

2.4.2 Parameters affecting the Critical Potential

The critical potential is dependent on a number of parameters. As might be expected from the percolation theory, critical potential decreases with increasing mole fraction of LN metal. Alloys richer in the more active element will have larger high-density clusters of this atom type, which results in significant reduction in dissolution potential. Increasing concentrations of LN metal ions in solution results in an increase in exchange current density, thereby a decrease in the critical potential. Both γ and D_s have proportional effects on the CP, yet, without knowing how impurities and adsorbed ions affect each quantity, it is not clear how different species in solution would affect E_c . Other parameters that have been found to affect the E_c value include defect density caused by cold work³⁴, degree of atomic ordering of the alloy⁵¹, temperature, composition of the solution and the rate of application known as the potential sweep rate⁵². Parameters that do not have a measurable effect on E_c include electrode potential, time in the passive region ($E < E_c$)³⁴ and pH.

CHAPTER 3 EXPERIMENTAL

3.1 Electrochemical Treatment

Polycrystalline silver-gold alloys with compositions of $\text{Ag}_{0.80}\text{Au}_{0.20}$, $\text{Ag}_{0.75}\text{Au}_{0.25}$, $\text{Ag}_{0.70}\text{Au}_{0.30}$, and, $\text{Ag}_{0.65}\text{Au}_{0.35}$ alloy sheets with 0.2 mm thick were used for this work. The foil stock was prepared by Ames Laboratory, Ames, IA by encapsulating 99.999% pure elements in a quartz ampoule sealed under inert gas. The ampoules are heated above the melting point of the metals, mixed well by rotating the ampoule within the furnace, withdrawn from the furnace and quenched in H_2O . The alloys are then cold rolled to a thickness of 0.2 mm and annealed following fabrication to remove any residual stresses. Composition of the alloy samples was confirmed by Wavelength Dispersive Spectroscopy (WDS) utilizing a Cameca SX-50 electron microprobe operating at 15kV and 20nA. The X-ray intensities were calculated using the PAP general method which uses a modified version of the $\Phi(\rho z)$ polynomial used in the standard ZAF correction scheme. As shown in the Ag-Au phase diagram, Figure 3-1, this alloy system forms a single-phase random solid solution over the entire composition range so that the dealloying process is not complicated by dissolution or formation of different phases. The lattice parameters of Ag and Au are almost identical with a lattice mismatch of only 0.2 %. This allows us to ignore complications arising from structural rearrangements driven by lattice strains as Ag is selectively dissolved from the lattice.

Prior to use in the electrochemical cell, samples of approximately 1cm \times 1 cm were cut from 0.2 mm thick foils. After the samples are mechanically polished with $\text{g-Al}_2\text{O}_3$ to a 1.0 μm finish using Buehler Carbimet polishing paper, they are masked with Teflon tape to a known exposed area. The polishing residue was removed by rinsing the samples with Nanopure water. These surfaces were not annealed after polishing in order to avoid issues related to the surface segregation of Ag.

Electrolytes of 0.1 M HClO_4 , 0.1M HClO_4 + 0.1M KI, 0.1M HClO_4 + 0.1M KBr and 0.1M HClO_4 + 0.1M KCl were prepared from reagent-grade chemicals and deionized

water with a Barnstead Nanopure system with a specific resistance of $>18 \text{ M}\Omega$. A saturated mercury/mercurous sulphate electrode was chosen as a reference to avoid unwanted chloride contamination of the electrolytes

$$E_{\text{MSE}} = E_{\text{SCE}} - 0.4 \text{ V} = E_{\text{NHE}} - 0.64 \text{ V}$$

Two Pt foils were used as counter electrodes placed parallel to either side of the alloy foil. Each of the alloy samples listed above was used as the working electrode. The stability of the reference electrode was checked against an unused MSE reference electrode chosen as “the standard” and found to be within 5mV over several hours period. All the potentials quoted in the following sections are with respect to NHE unless otherwise noted.

The electrochemical cell consisted of a 150 ml crystallizing dish with an electrolyte volume of approximately 100 ml. All cells and glassware used were cleaned in 50:50 mixtures of HNO_3 and H_2SO_4 that was heated at 60°C followed by multiple rinsing in double distilled and Barnstead Nanopure water.

All electrochemical experiments were performed at room temperature. Electrolytes were not deaerated as this was found to have no effect on the electrochemical characteristics of dealloying in Ag-Au systems.

Electrochemical studies were carried out using both a PAR model 273 potentiostat and a Gamry Potentiostat with a Model PC4/750.

Micrographs of the samples were obtained using a LEO 1550 field emission scanning electron microscope with a typical accelerating voltage of 10 kV.

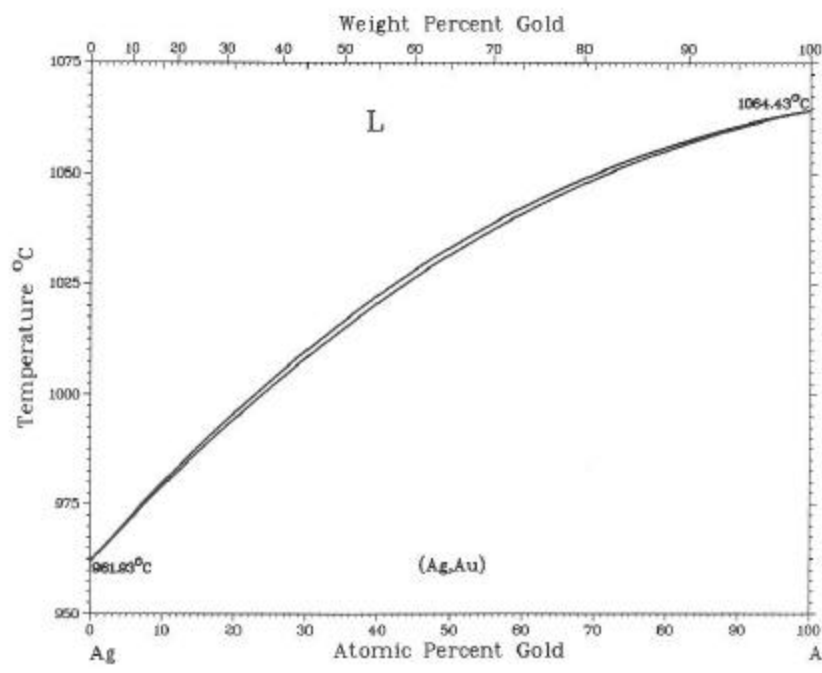


Figure 3-1 The gold-silver phase diagram. (Adapted from Binary Alloy Phase Diagrams, 2nd edition, Vol. 1, T.B. Massalski, Editor-in-Chief, 1990)

3.2 Characterization of Samples Using Small Angle Neutron Scattering (SANS)

Following the study performed by Corcoran et.al⁵³, small angle neutron scattering (SANS) was used for characterizing the average ligament size and distribution of our dealloyed structures.

Small Angle Neutron Scattering (SANS) measurements were carried out on the 30 m long National Science Foundation SANS instrument (typically NG3) at the National Institute of Standards and Technology (NIST) 20MW reactor in Gaithersburg, MD. The samples were placed in an evacuated chamber in transmission geometry. (See Figure 3-2) Data were collected over Q ranges extending from about 0.009 to 0.174\AA^{-1} . The magnitude of the scattering vector, Q is $(4\pi / \lambda_{neutrons}) \sin\Theta$, where λ is the neutron wavelength and 2Θ the scattering angle. The wavelength of the incident neutrons was 6\AA and sample-to-detector distances were 1.3 m (small configuration), 4.5 m (medium

configuration), and 13.2 m (large configuration). The raw SANS data was corrected for background and empty cell scattering.

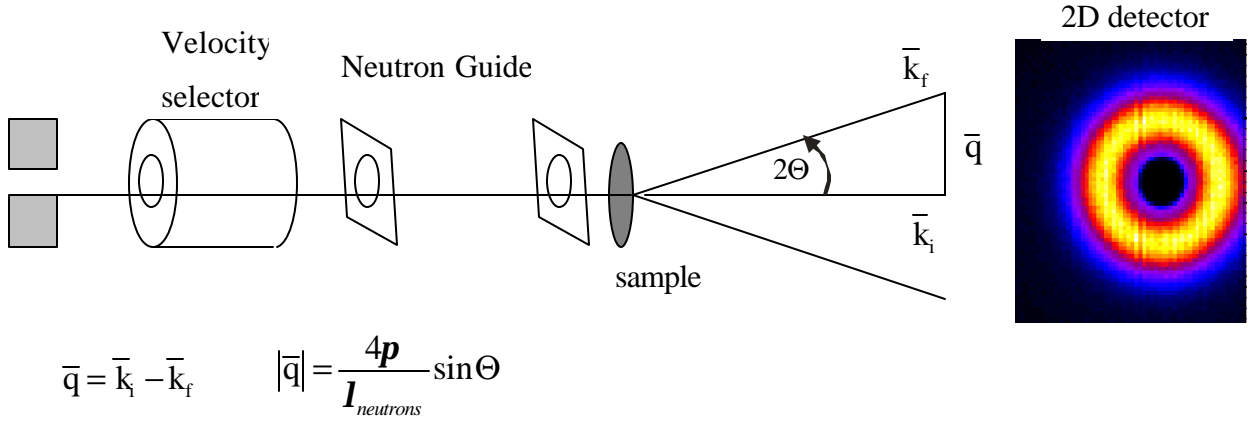


Figure 3-2 Schematic drawing of the transmission geometry in SANS experiments.

The SANS measurements allow us to generate full 3-D simulations of the structures by which we can characterize a variety of properties. SANS from nanoporous metals is very much similar to that of scattering from microemulsions⁵⁴ and spinodally decomposed materials⁵⁵ all of which display a bi-continuous morphology. A typical SANS intensity data for a porous Au metal is shown in Figure 3-3. The data exhibits a pronounced peak at some finite Q_m with its associated intensity $I(Q_m)$, followed by an extended tail decaying exponentially as Q^{-4} (Porod law), at large enough values of Q . The presence of a peak is a good evidence for a structure consisting of disordered interpenetrating porous structure with a well-defined average length scale approximated as $2\pi/Q_m$.

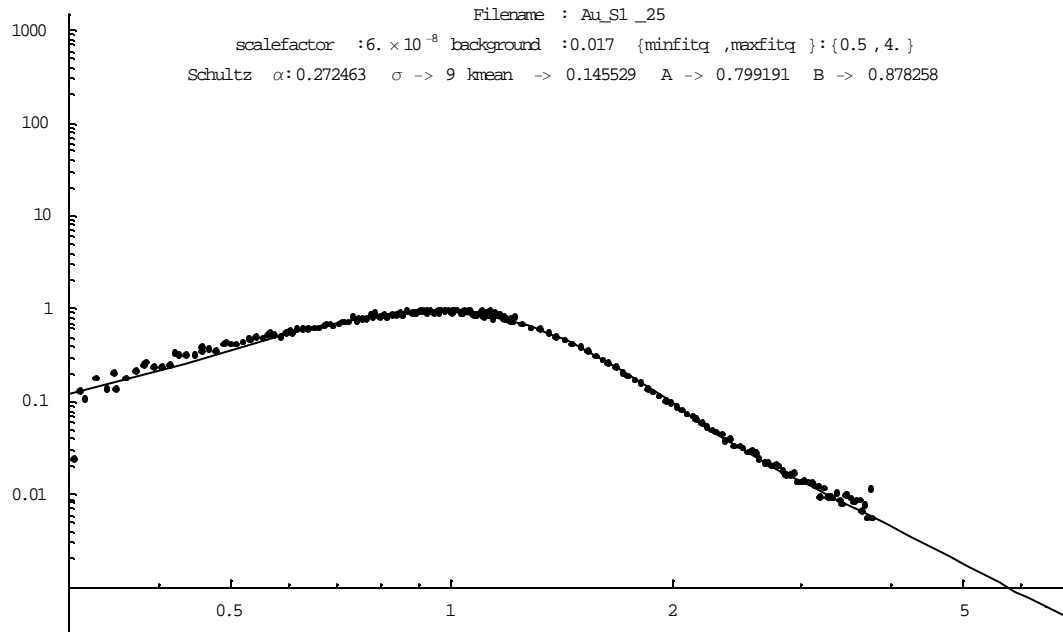


Figure 3-3 A typical SANS data for dealloyed Ag-Au alloy. The solid line is the fit obtained using leveled wave method of Berk.

The scattering from bi-continuous structures has been analyzed extensively by Berk^{56,57} and Chen et.al.^{58,59}. In our study, the leveled wave method of Berk has been chosen to analyze the SANS data because one of the advantages of this model is that it can generate the three dimensional microstructures of the two-phase (metal-void) morphology. In this model, random porous morphologies are mathematically modeled as two-dimensional continuous contours of a stochastic standing wave generated by summing a large number of plane waves with random amplitudes, wavevector directions, and phase constants but with defined wavevector magnitudes. Once the dealloyed structure is modeled, the scattering from the mathematically modeled structure can then be calculated and compared with the experimental data. The result is a fit to the data and a 3-D image of the bi-continuous structure that can be analyzed directly for determining ligament size and distribution, and surface area. See Figure 3-4.

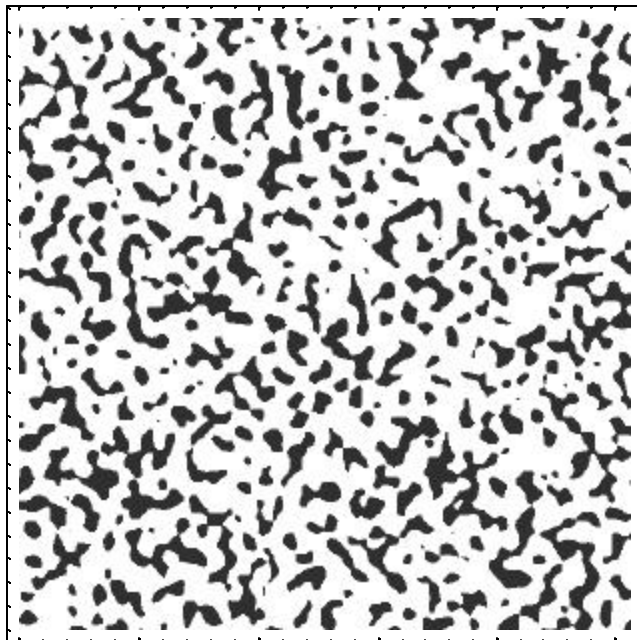


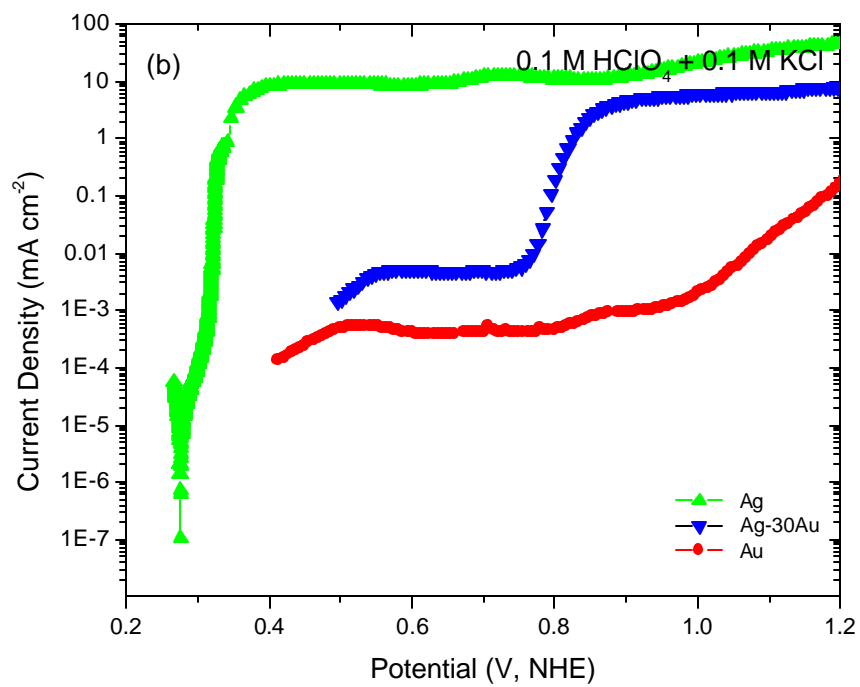
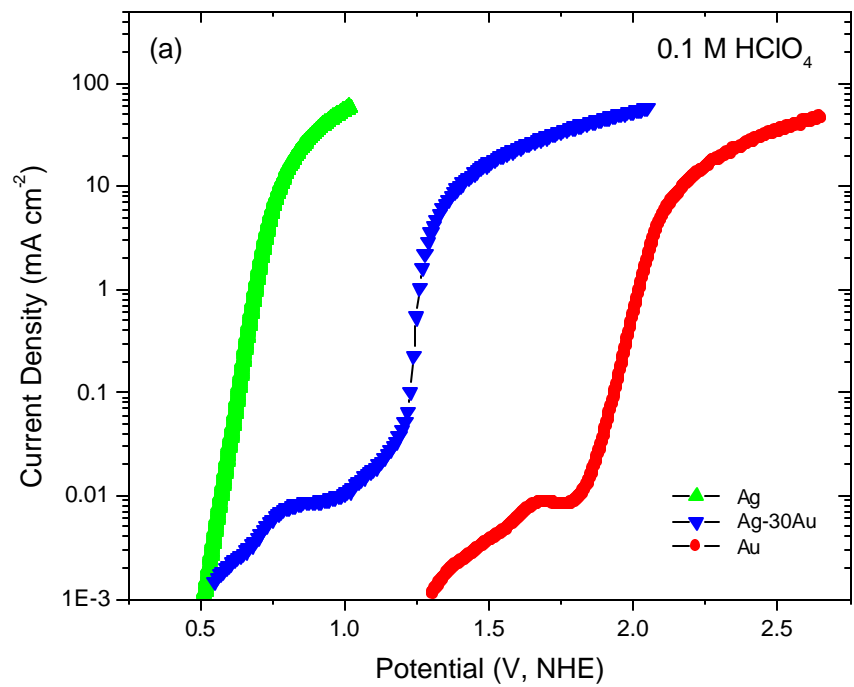
Figure 3-4 Simulated two-dimensional slice of a three-dimensional porous structure calculated from the fits to the scattering data in Figure 3-3. The average Au ligament width calculated from the images is 11.2 nm. The black areas represent pure Au ligaments.

CHAPTER 4 DEALLOYING IN HALIDE CONTAINING ELECTROLYTES: EFFECT ON CRITICAL POTENTIAL AND PORE SIZE

In this part of the study, we examined the effect of halides on the resultant size scale of porous gold and the critical overpotential obtained through room temperature dealloying of $\text{Ag}_{0.70}\text{Au}_{0.30}$ and $\text{Ag}_{0.65}\text{Au}_{0.35}$ alloys in 0.1 M HClO_4 with and without halide additions.

4.1 Anodic Polarization Measurements

Figure 4-1 a-d shows the anodic polarization behavior of pure Ag, $\text{Ag}_{0.7}\text{Au}_{0.3}$, and pure Au in 0.1 M HClO_4 , 0.1 M HClO_4 + 0.1 M KCl, 0.1 M HClO_4 + 0.1 M KBr, and 0.1 M HClO_4 + 0.1 M KI, respectively. The Ag equilibrium potentials in these electrolytes as determined from open circuit measurements and Tafel analysis of the above curves were in agreement and shown in Table 4-1. These values were used to correct all potentials in Figure 4-3 and Figure 4-4 such that the dealloying data could be plotted as a function of overpotential relative to the Ag equilibrium potential in the corresponding electrolyte. As shown, the Ag equilibrium potential decreases with the addition of halides to the electrolyte. The addition of 0.1 M KI gave the least value of -0.077 NHE. Figure 4-1 also demonstrates that Au is not undergoing significant electrochemical reactions at the dealloying potentials used in this work, i.e. for a potential corresponding to a dealloying current of 1 mA/cm^2 , the electrochemical reactions on the Au electrode were less than $1 \text{ }\mu\text{A/cm}^2$. Also note that the slope, dI/dE , at small overpotentials is nearly vertical for Ag dissolution in the halide electrolytes and then quickly becomes diffusion limited at slightly greater overpotentials. This rapid rise in the current seen at small overpotentials is indicative of a much larger value for the exchange current density in the halide electrolytes. The limiting current density seen at higher overpotentials was believed to be due to limiting of ion transport across a silver halogen salt film formed on the alloy surface. The presence of a deposit of Ag salt was confirmed by surface analysis performed using an electron microscope (Figure 4-2).



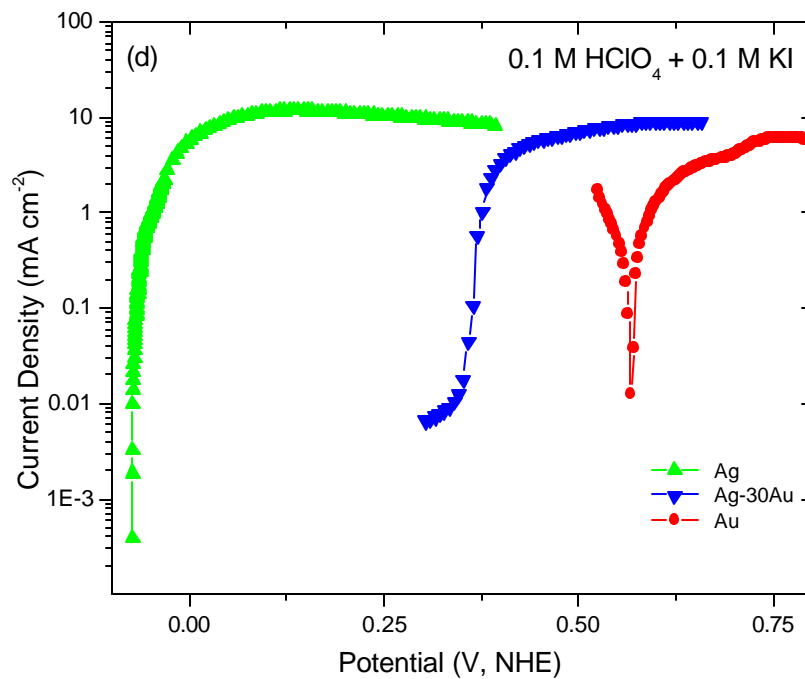
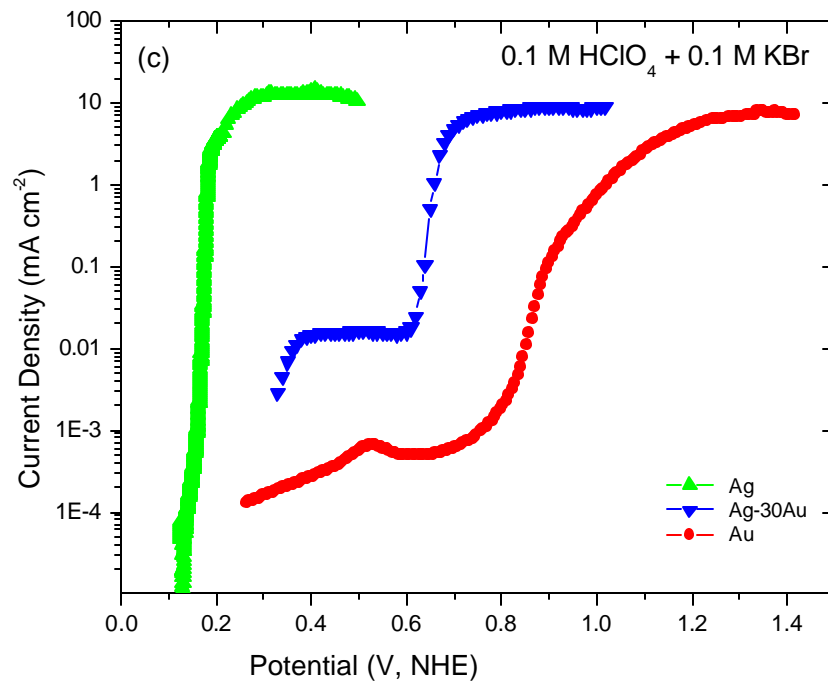


Figure 4-1 Potential dynamic scans of pure Ag, Ag_{0.70}Au_{0.30} and pure gold in (a) 0.1 M HClO₄, (b) 0.1 M HClO₄ + 0.1 M KCl, (c) 0.1 M HClO₄ + 0.1 M KBr, and (d) 0.1 M HClO₄ + 0.1 M KI. Potentials were referenced to standard hydrogen scale in the indicated solutions.

Table 4-1 Critical dealloying overpotentials for $\text{Au}_{0.35}\text{Ag}_{0.65}$ and $\text{Au}_{0.30}\text{Ag}_{0.70}$ in 4 different media. The potentials in column 2 are with respect to NHE. The overpotentials, $\Delta E_{1.0\text{mA}/\text{cm}^2}$, are with respect to equilibrium potential for Ag as given in column 2.

Electrolyte	$E_{\text{Ag}}^{\text{equil}}$	$\Delta E_{1.0\text{mA}/\text{cm}^2}$, V ($\text{Au}_{0.35}\text{Ag}_{0.65}$)	$\Delta E_{1.0\text{mA}/\text{cm}^2}$, V ($\text{Au}_{0.3}\text{Ag}_{0.7}$)
0.1 M HClO_4 + 0.1 M KI	-0.077	0.481	0.453
0.1 M HClO_4 + 0.1 M KBr	0.135	0.593	0.524
0.1 M HClO_4 + 0.1 M KCl	0.280	0.602	0.542
0.1 M HClO_4	0.445	0.864	0.813

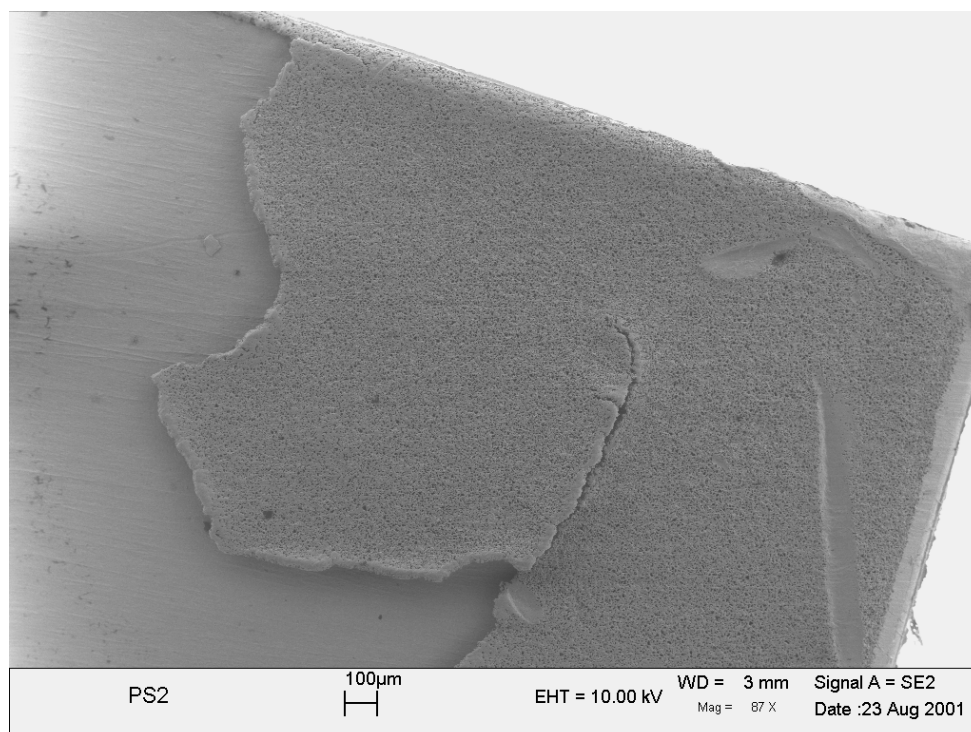


Figure 4-2 SEM photomicrograph showing silver salt film (AgBr in this case) formed on $\text{Ag}_{0.70}\text{Au}_{0.30}$ alloy surface after dealloying.

Figure 4-3 and Figure 4-4 summarize the results for the electrochemical behavior of $\text{Ag}_{0.7}\text{Au}_{0.3}$ and $\text{Ag}_{0.65}\text{Au}_{0.35}$ as a function of halide addition to the electrolyte. They are plotted as overpotential relative to the Ag equilibrium potential measured in Figure 4-1 a-c. Plotting as overpotential is necessary to separate the relative reduction in critical potential from the reduction in equilibrium potential for Ag dissolution. The addition of halide to the electrolyte decreased the critical overpotential necessary for dealloying. The greatest change (almost 50% reduction) was observed for the KI containing electrolyte.

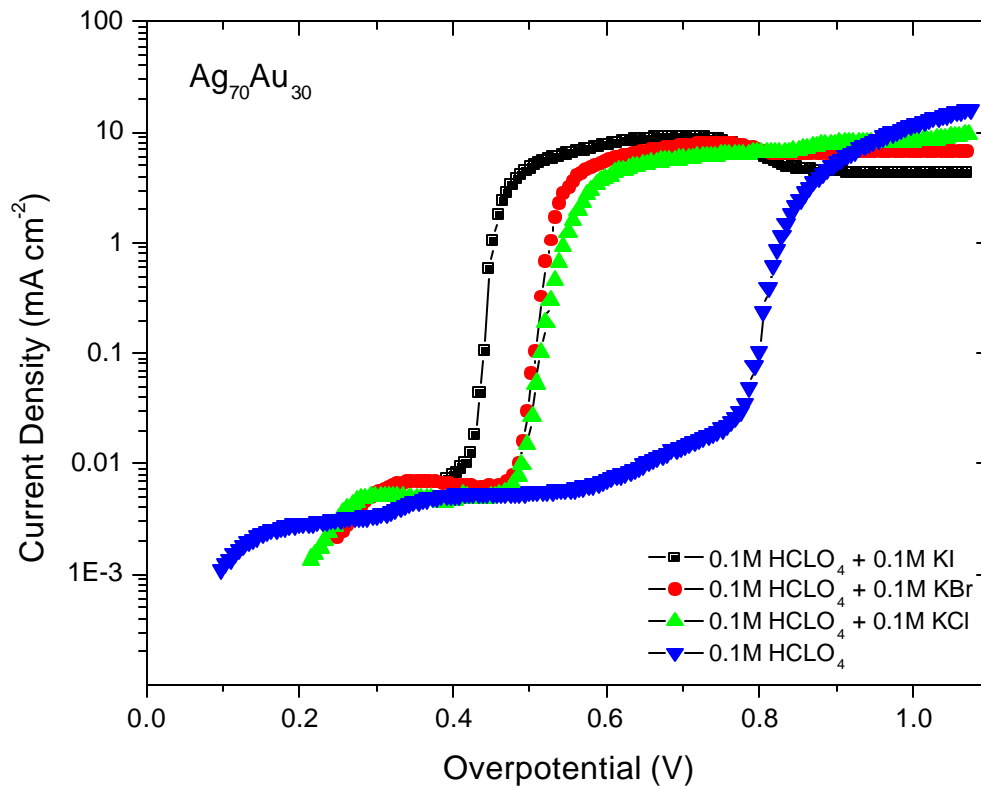


Figure 4-3 Potential dynamic scans of $\text{Ag}_{0.70}\text{Au}_{0.30}$ in the indicated solutions. The potentials are referenced to equilibrium potential of Ag also in the indicated solutions. Scan rate is 3 mV/sec.

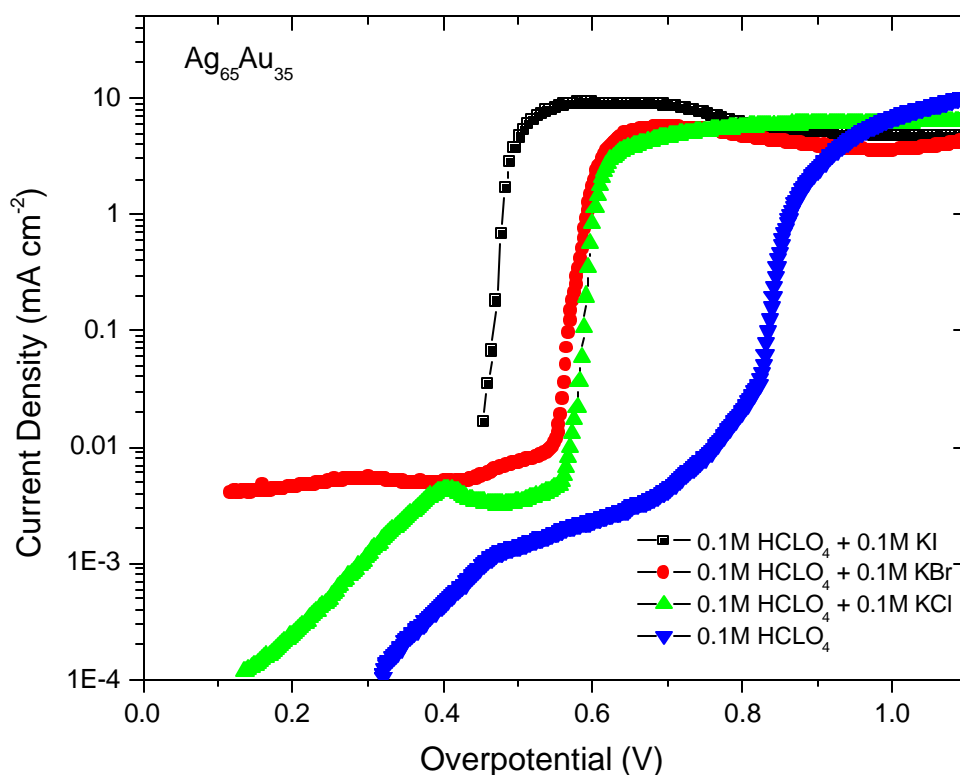


Figure 4-4 Potential dynamic scans of $\text{Ag}_{0.65}\text{Au}_{0.35}$ in the indicated solutions. The potentials referenced to equilibrium potential of Ag also in the indicated solutions. Scan rate is 1 mV/sec.

Some ambiguities exist in defining the critical potential. It is associated either with the onset of the rapid rise in current with potential or “knee” in the polarization curves as seen in Figure 4-1, Figure 4-3 and Figure 4-4. If we consider Figure 4-1(a) for example, we can see that this knee is not well defined for the $\text{Ag}_{0.70}\text{Au}_{0.30}$ alloy. The critical potential is obtained either by determining the potential value corresponding to the very first rise in current or by extrapolating the rapidly increasing current portion of the curve to the baseline. An approximately 0.2 V difference has been found between the two methods. This discrepancy is even worse if one considers that this “knee” is also sensitive to the scan rate used to generate the polarization data. Recently Sieradzki et al⁵² performed a detailed investigation of the critical potential for a series of Ag-Au alloys in HClO_4 acid electrolytes. For the sake of direct comparison to his work, we adopted the same method for defining a critical potential. We took the critical potential as that potential corresponding to a current density of 1.0 mA/cm^2 . However, we should point

out that dealloying (as determined by potential hold measurements) will occur at potentials as much as 150 mV below this value⁴⁵. The results of this study will be given in Chapter 5. To avoid confusion we will denote these overpotentials as, $\Delta E_{1.0\text{mA}/\text{cm}^2}$, rather than as E_c .

The estimated values of $\Delta E_{1.0\text{mA}/\text{cm}^2}$ determined from the polarization data in Figure 4-3 and Figure 4-4 are tabulated in Table 4-1. The value of $\Delta E_{1.0\text{mA}/\text{cm}^2}$ decreased as the Ag content of the alloy was increased by 5 % for all the electrolytes. It is obvious from the results that $\Delta E_{1.0\text{mA}/\text{cm}^2}$ is strongly dependent on the nature of the electrolyte. The susceptibility of Ag-Au alloys to dealloying followed the sequence $\Gamma^- > \text{Br}^- > \text{Cl}^- > 0.1 \text{ M HClO}_4$. We have conducted a series of potential hold experiments to determine a precise value for the dealloying critical potential for these systems. Preliminary data suggest that dealloying in 0.1 M HClO_4 for $\text{Ag}_{0.70}\text{Au}_{0.30}$ occurs at overpotentials as low as 0.605 V compared to the value of $\Delta E_{1.0\text{mA}/\text{cm}^2} = 0.813 \text{ V}$ given in Table 4-1. It is interesting to note that the typical “plateau” region observed in alloy polarization curves (see for example Figure 4-1a) is absent in the KI containing electrolyte. We believe this is indicative of systems with very large exchange current densities. The effect of halides on the electrochemical data shown in Figure 4-1, Figure 4-3 and Figure 4-4 is similar to that measured previously by Galvele et al.⁶⁰ A direct comparison is difficult since their electrochemical conditions were different (neutral 1 M halide containing electrolytes). But the same absence of a plateau region for iodide containing electrolytes was noted by the authors.

4.2 Morphology of Dealloyed Structures

In order to minimize the effect (if any) of dissolution rate on pore morphology, we performed a series of potential hold experiments until we were able to identify applied potentials that displayed similar current decay behavior over the range of our experiments. These potentials were then used to hold the alloys in the various halide electrolytes. Figure 4-5 shows the current decay response corresponding to the applied potentials used. The HClO_4 acid electrolyte did not display a current decay so we chose a

potential that best represented the tail of the halide containing data. This lower current, if anything, would result in perhaps a slightly larger than expected pore size but since this sample clearly had the smallest pore size of all samples we assume that the dissolution rate effect is secondary for this set. The current decay behavior for the halide electrolytes approached a power law decay of $t^{0.5}$ indicating the current was controlled by the build-up of a Ag-halide salt on the alloy surface.

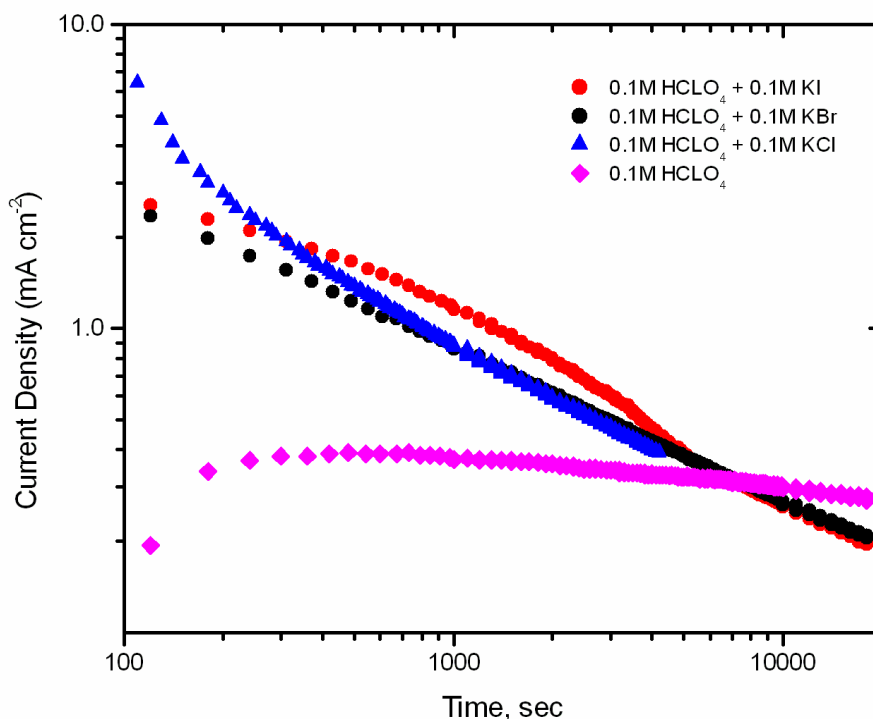


Figure 4-5 Current decay behavior for $\text{Ag}_{0.65}\text{Au}_{0.35}$ at (\blacktriangledown) 1.285 V vs. NHE in 0.1 M HClO_4 , (\blacktriangle) 0.95 V in 0.1 M HClO_4 + 0.1M KCl, (\bullet) 0.74 V in 0.1 M HClO_4 + 0.1M KBr, (\blacksquare) 0.404 V in 0.1 M HClO_4 + 0.1M KI.

SEM photomicrographs reveal dramatic differences in pore size of dealloyed $\text{Ag}_{0.65}\text{Au}_{0.35}$ as a function of the electrolyte as shown in Figure 4-6. The applied potential and current versus time behavior for these samples are shown in Figure 4-5. The average pore size as estimated from the SEM micrographs are shown in Table 4-2 and varies from 8 nm in 0.1 M HClO_4 to 67 nm in 0.1 M HClO_4 + 0.1 M KI.

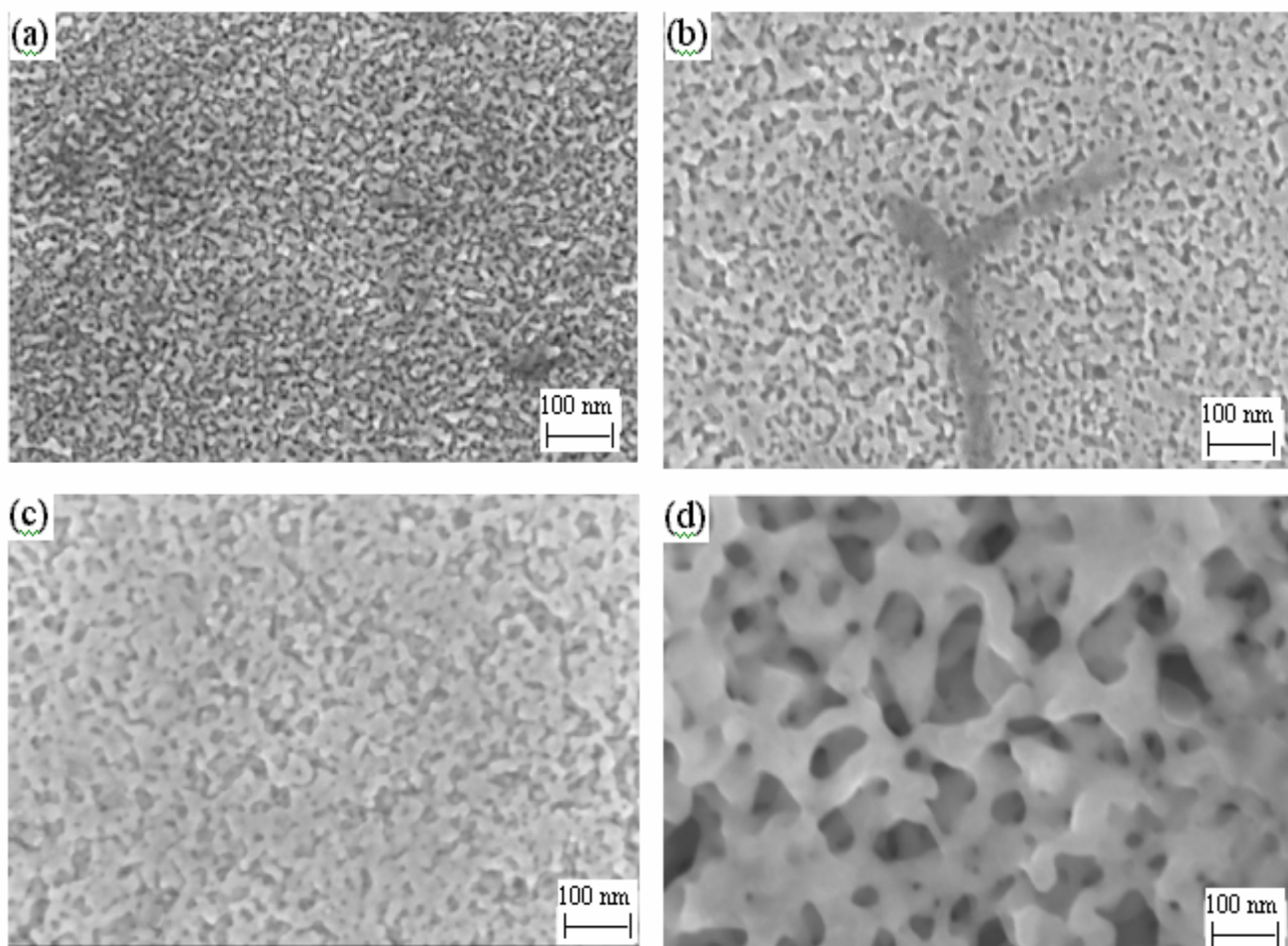


Figure 4-6 Scanning electron micrographs showing bio-continuous solid-void structure of $\text{Ag}_{0.65}\text{Au}_{0.35}$ after de-alloying at (a) 1.285 V vs. NHE in 0.1 M HClO_4 , (b) 0.95 V in 0.1 M HClO_4 + 0.1M KCl, (c) 0.74 V in 0.1 M HClO_4 + 0.1M KBr, (d) 0.404 V in 0.1 M HClO_4 + 0.1M KI.

Table 4-2 Effect of electrolyte composition on the pore size for dealloyed $\text{Ag}_{0.65}\text{Au}_{0.35}$ as determined by cord length measurements of the micrographs shown in Figure 4-6. The surface diffusivity is calculated using equation (4.2).

Electrolyte	Hold Potential for 5 hrs mV vs. NHE	Pore size , nm	D_s ($\text{cm}^2 \text{sec}^{-1}$)
0.1 M HClO_4 + 0.1M KI	404	67 ± 18	8×10^{-13}
0.1 M HClO_4 + 0.1M KBr	740	16 ± 0.08	3×10^{-15}
0.1 M HClO_4 + 0.1M KCl	950	17 ± 1.8	3×10^{-15}
0.1 M HClO_4	1285	7.8 ± 0.54	2×10^{-16}

4.3 What factors control the average pore size in a dealloyed structure?

Following the percolation model proposed by Sieradzki et al.^{30,49} (recently reanalyzed and extended by the same authors⁵²), we argue that the surface diffusivity of the remaining element (Au in this case) dominates the resultant size scale of porosity created during dealloying. We expect the rate of dealloying to have very little effect on the average pore size. In many cases, the change in size scale that one may observe with changes in dealloying rate (i.e. through changing the dealloying potential) is most likely a result of the potential dependence of the diffusivity. The dealloying rate only has the effect of establishing the initial pore size, r_o , created during the roughening instability that leads to the dealloyed bicontinuous structure. This instability is a result of competition between the surface diffusion smoothing process and the selective dissolution roughening process⁵² with the constraint that the instability wavelength can not be arbitrarily large and in fact must be less than some preexisting compositional length-scale, ξ , in the alloy. Statistically, one can identify a percolation cluster size of interconnected atoms of the active component as $x^{Perc} = a_m \left(\frac{1+p}{1-p} \right)$ where a_{mn} is the

nearest neighbor distance and p is the atom fraction of the less noble element. The wavelength ξ , should then be related to the separation of clusters, which can be approximated as $2x^{Perc}$ and the initial pore size, r_o , will be approximately given by x^{Perc} . For $Ag_{0.70}Au_{0.30}$ and $Ag_{0.65}Au_{0.35}$, x^{Perc} hence r_o is equal to 1.6 nm and 1.4 nm respectively. This is considerably smaller than most experimentally measured pore sizes in gold indicating that significant coarsening is occurring during the dealloying process. If these percolation concepts are correct, then we should be able to approach x^{Perc} for an alloy where the noble component has a high melting point, i.e. very low value of diffusivity at room temperature. In fact for the system $Cu_{0.70}Pt_{0.30}$, the selective dissolution of Cu leads to the formation of porous Pt with an average pore size of approximately 3 nm⁴⁵ which is reasonably close to x^{Perc} for this system of 1.6 nm.

Corcoran et.al¹⁸ found that the kinetics of evolution of porosity fits linear ligament size (pore size) vs. $t^{0.25}$ relationships which are similar to those describing the evolution of particle size in coalescence phenomena⁶¹. This is in agreement with the literature for the relaxation of roughened gold surfaces^{62,63,64,65,66}. The coalescence process is thought to proceed by surface diffusion of adatoms from sites of higher to sites of lower chemical potential, i.e., a surface diffusion process from small to large size particles. Following a similar analysis we can describe the coarsening process of dealloyed Au as:

$$r^4 - r_o^4 = \frac{2\gamma a^4 D_s t}{kT} \quad (4.1)$$

where r is the average pore radius at time t , r_o is the initial pore size, γ is the surface energy, a is the lattice parameter, D_s is the surface diffusivity, k is the Boltzmann constant, and T is the absolute temperature. Owing to the power law dependence, r_o represents a less than 7 % correction to the calculation for D_s when r is larger than $2 r_o$. Therefore, even for the smallest pore size measured in this study of 7.8 nm, we don't expect a significant correction to the value of D_s considering that our value of r_o is expected to be of order 1.5 nm.

4.4 Estimation of Surface Diffusivity of Gold in Halide Electrolytes

Table 4-2 gives the average pore size measured after dealloying for 5 hours in the indicated electrolytes as taken from the SEM micrographs in Figure 4-6. Rewriting equation (4.1) for Au, with the parameters $t = 5$ hours, $r_o = 1.5 \times 10^{-9}$ m, $\gamma = 1 \text{ J m}^{-2}$, $a = 4.08 \times 10^{-10}$ m, $k = 1.3806 \times 10^{-23} \text{ J K}^{-1}$, and $T = 300 \text{ K}$ we get:

$$D_s = -2.10 \times 10^{-19} + 4.15 \times 10^{16} r^4 \quad (4.2)$$

where r is in units of m and D_s is in units of $\text{cm}^2 \text{ sec}^{-1}$.

Table 4-2 gives the surface diffusivity calculated for the different electrolytes using equation (4.2). The surface diffusivity for gold has been measured via relaxation of roughened surfaces and has been shown to depend strongly on the electrochemical conditions but generally varies in the range of 10^{-15} to $10^{-13} \text{ cm}^2 \text{ sec}^{-1}$ depending upon the applied potential and the electrolyte composition^{64,66}. The presence of chloride has been shown to increase the value of diffusivity⁶⁶. A direct comparison of diffusivities is difficult since the potentials we use during dealloying are much greater than the potentials used in the literature for surface diffusivity measurements. Nonetheless, the order of magnitude of our results is consistent with that reported.

4.5 Effects of Halides on Critical Potential

The critical overpotentials taken from the alloy polarization data are summarized in Table 4-1. The values of the critical overpotential, $\Delta E_{1.0 \text{ mA/cm}^2}$, in the 0.1 M HClO_4 electrolyte are in good agreement with those measured recently by Sieradzki et al⁵². The authors measured values of critical potential as a function of Ag ion concentration. Extrapolating their results to a Ag ion concentration of 10^{-6} M (approximating our electrolytes) we get a value of 1.23 V for $\text{Ag}_{0.70}\text{Au}_{0.30}$ and 1.3 V for $\text{Ag}_{0.65}\text{Au}_{0.35}$. We

measure values of 1.26 V (0.445 + 0.815 V) and 1.31 V (0.445 + 0.864 V) respectively for the same alloy compositions.

As discussed previously, the addition of halides results in an increase in size scale of the porosity as a result of increasing the surface diffusivity. Based only on surface diffusivity considerations, we would expect dealloying in the halide containing electrolytes to display a larger value of critical overpotential since the kinetics of the smoothening process has increased. This is clearly not what the data shows. We see an almost 50% reduction in the critical overpotential with the addition of 0.1 M KI into the electrolyte. Considering the dealloying critical potential as a roughening instability driven by a competition between surface diffusion smoothening and alloy dissolution roughening, Sieradzki et al.⁵² recently developed the following equation for the critical overpotential, \bar{h}_{crit} :

$$\bar{h}_{crit} = 2 \frac{\mathbf{d}}{a} \frac{g}{2-g} + \frac{2k_b T}{nq} \text{ArcSinh} \left[\frac{\mathbf{p}^2 \mathbf{g} \Omega D_s N_s}{nq \mathbf{d} J_o a^2} \left(\frac{g}{2-g} \right)^2 \right] \quad (4.3)$$

where g is the atom fraction of Au in the alloy, k_b is the Boltzmann constant, T is the absolute temperature, n is the number of electrons involved in the dissolution process, q is the charge of an electron, \mathbf{g} is the surface energy, Ω is the atomic volume, D_s is the surface diffusivity, N_s is the surface density of atoms, J_o is the exchange current density in units of #atoms $\text{m}^{-2} \text{sec}^{-1}$, a is the near neighbor distance, and \mathbf{d} is a fitting parameter related to the compositional variation across the alloy surface.

Considering this equation, we see that the competition between the smoothening and roughening terms are expressed as the ratio D_s/J_o in the ArcSinh. This equation predicts a decreasing value of the critical overpotential as this ratio decreases. For our halide containing electrolytes, this means that the value of exchange current, J_o , must be increasing at a faster rate than the increasing surface diffusivity, D_s . Considering the Tafel behavior of pure Ag in Figure 4-1 for the various electrolytes, we can at least

confirm qualitatively that the exchange current is increasing considerably, i.e. the slope dI/dE is nearly vertical in the iodide containing electrolyte as compared to the 0.1 M HClO_4 electrolyte. However, in order to make a quantitative estimate for the exchange current density in the above equation, we need an accurate measurement of the critical overpotential. The values measured in this part of the study are function of scan rate and are not accurate enough for use in the above equation. We found that the best measure of the critical potential appears to be through potential hold experiments. We have observed that through analysis of the shape of the current transient following a potential hold, we can determine whether or not we are above the critical potential. Through multiple potential hold experiments, one can “zero – in” on the value of the critical overpotential for a given system. These experiments were already performed in our laboratory and will be discussed in subsequent chapters.

CHAPTER 5 STEADY STATE METHOD FOR DETERMINING THE DEALLOYING CRITICAL POTENTIAL

The general consensus in the literature is that while the surface of the alloy remains planar below CP ($E < E_c$), gross surface roughening occurs and the alloy evolves into interconnected porous network at applied potentials above the CP ($E > E_c$). However, the situation at potentials near critical potential is less clear and it did not get much attention in the literature. We studied the time dependence of the dissolution behavior of AgAu alloys at potentials below and in the vicinity of the critical potential. The current study will provide experimental data which can be tested by theoretical model calculations. The study should thus contribute to a better understanding of the mechanisms controlling the selective dissolution in the subcritical potential region.

To our knowledge, the results presented here-in represent the first report on current transients below the critical potential, E_c over significantly longer times. These results along with scanning electron microscopy were used to demonstrate that the measurement of the critical potential for alloy dissolution calculated based on extrapolation of anodic polarization data results in an overestimation of this quantity. A series of constant applied potential experiments proved to be a more accurate method for critical potential determination. For the rest of the thesis, while E_c will refer to conventionally defined critical potential, E_{crit}^* will refer to what we call the “true” critical potential.

As this thesis was being prepared it came to our attention that Jonah Erlebacher⁷⁴ has developed a Monte Carlo simulation to demonstrate the main atomistic features of a percolation model for passivation of binary alloys. The author performed a series of dealloying simulations on the Ag/Au system pulsed to fixed potentials quite similar to the experimental results presented here. These new simulation results are fully consistent with our experimental results. This is also an important validation of our understanding of critical potential.

Before we go into the results and discussion section, a brief review of literature on dealloying studies below the critical potential was presented.

5.1 Below the Critical Potential

Several investigators have examined the form of current transients below E_c ^{34,71,69,67}. Typically, the current transients are only monitored over a period of minutes or at the most several hours. It has been typically accepted that a potential hold below (but in the vicinity of) E_c would result in a potential independent current transient which follows a power-law decay, $i \propto t^{-m}$, with m in the range of 0.5 and 1.0.

Based on the value of the exponent, m , different mechanisms have been proposed to explain the breakdown of the protective more noble (MN) rich layer over the surface and to support the small but measurable currents that exist below the critical potential. Wagner et.al⁶⁸ argued that the current decay is a result of reduction of mobility of vacancies due to coalescence and growth of vacancy clusters with continued dissolution of active metal at step edges and a few large clusters of active atoms existing on the surface. In situ STM results support the mechanism of vacancy clustering and preferential attack at step edges. The author found three different regimes of power-law current decay behavior below E_c . The first deep step decrease in the current time transients prior to power-law decay of the current is attributed to the exhaustion of a surface enriched Ag layer which probably resulted from segregation processing. Their analysis revealed that the current follows $t^{5/8}$, $t^{1/2}$, and $t^{1/4}$ behaviors, respectively, for surface-vacancy-controlled periphery diffusion (PD), terrace diffusion (TD), and evaporation-condensation (EC). It was concluded that the PD mechanism of vacancy motion, in which the mass transport occurs via diffusion along the boundary or edge defining the vacancy, is dominant in systems they examined.

Forty and Rowlands⁴⁴ developed a surface-diffusion-controlled, layer by layer model based on TEM micrographs of chemically etched binary alloys. Based on their experimental study on AgAu and CuAu system, the authors suggested that the corroding alloy surface becomes covered by a gold layer. This layer forms initially from island nuclei which grow and eventually merge to form a connected structure enclosing channels and pits where the merger was incomplete. This model predicts a current-time

transient of the type: $i \propto (1/t)^{c/(1-2c)}$, where c is the atom fraction of the MN component. This prediction however does not fit the observed behavior in the current-decay at potentials below E_c , since some investigators^{69,70} have applied this model for the potentials below E_c , even though the original model was developed for potentials above E_c .

Ateya et.al⁷⁰ considered the evolution of concentration gradients near the surface as surface atoms of less noble (LN) metal are dissolved into the electrolyte. Continued dissolution results from the diffusion of LN atoms from the bulk of the alloy driven by the developing concentration gradient. Equating the kinetics of dissolution and diffusion, the authors have developed analytical equations for the decaying current with time.

The solid-state diffusion model of Pickering and Wagner⁴⁰ postulated an indefinite decrease of the dissolution current with time ($m = 0.5$) and the development of a characteristic depth concentration profile within the solid. The authors suggested that interdiffusion is enhanced by the presence of an excess of divancies injected into the surface layer during the dissolution process. Marshakov et.al⁷¹ measured current time-transients at various subcritical potentials on $Zn_{0.70}Cu_{0.30}$ alloy in acid chloride solution and on $Ag_{0.30}Cd_{0.70}$ alloy in acid nitrate solution. Postulating that the concentration of divancies within the surface layer decreases with polarization time, their experimental results agrees well with the diffusional theory of Pickering and Wagner⁴⁰.

Fritz and Pickering⁷² studied the current behavior below critical potentials on CuAu alloy system. Current-time transient was found to follow the relationship, $i \propto t^{-0.5}$ in the initial portion (< 1 min) of the dissolution process. This is consistent with diffusion normal to the surface on the alloy side of the alloy/solution interface as the rate determining step of the selective copper dissolution process. However, departure from initial current-time behavior at ~ 1 min of the selective dissolution at potentials well below E_c has been observed. This is attributed to the onset of random (low-density) pit formation.

5.2 Morphology Below the critical Potential

At potentials below the critical potential, dissolution of the LN metal results in enrichment of the MN metal on the alloy surface. This prevents further dissolution of LN specie and results in a microscopically flat surface except for occasional well-separated pits. In a study performed by Fritz et.al.⁷², both the current-time behavior and TEM micrographs of the Cu-18 a/o Au samples after anodic treatment at potentials below E_c confirms that a planar surface is stable, although some isolated random pit formation and localized breakdown of the protective gold rich layer has been observed in the later stages of the dissolution period. After the potential was increased near E_c , the authors observed Moire fringe pattern which means that the surface layer has a three-dimensional interconnected porous character.

TEM examinations of Cu-Pd²⁵ and Cu-Au⁷² alloy surfaces, after selective removal of Cu by potentiostatic control at $E < E_c$, have revealed low density random pits with the 5-20 nm diameter. In-situ STM was utilized to investigate the evolution of the alloy interface at potentials in the passive region⁷³ ($E < E_c$). Several bumps and hills with 10 Å height has been observed at $-0.48V_{MSE}$ which is below E_c ($= 0.25 V_{MSE}$). Penetration of porous structure, measured by chronoamperometry, does not begin until near the critical potential. It has been suggested though that the currents measured in the passive region may be due to continued dissolution or local penetration of pit nuclei (on the order of 50 Å beneath the surface) from roughened regions due to possible dislocations and solid-state defects on the surface^{72,73}.

5.3 Current-time Transients obtained in the Current Study

Figure 5-1, Figure 5-2 and Figure 5-3 show the anodic current response of $\text{Ag}_{0.70}\text{Au}_{0.30}$, $\text{Ag}_{0.75}\text{Au}_{0.25}$, $\text{Ag}_{0.80}\text{Au}_{0.20}$ respectively, held at the indicated potentials in 0.1 M HClO_4 for typically 1 to 5 days. Alloys held above the conventionally defined critical potential ($\sim E_c + 150$ mV) display a constant mean dealloying current with time and sometimes a steadily increasing current. Alloys held well below E_c on the other hand ($\sim E_c - 150$ mV) display a rapidly decaying current following a power law behavior with an exponent of approximately $-3/4$ as shown for the holds at 0.79 and 0.99 in Figure 5-4 (a) and (b). The value of the exponent varied from -0.75 to -1 for the current time transients of alloy $\text{Ag}_{0.75}\text{Au}_{0.25}$ obtained at potentials 0.74 V, 0.890 V, 0.915 V and 0.930V as shown in Figure 5-5 (a) and (b). The same range of slope has been reported by Laurent and Landolt⁶⁹ for CuAu and AgPd alloys in 12 M LiCl and 1 M $\text{Na}_2\text{SO}_4 + 0.02$ M H_2SO_4 solutions. The solid-state diffusion model of Pickering and Wagner⁴⁰ as well as the surface diffusion model of Forty and Rowlands⁴⁴, predicts a slope of -0.5 for these transients.

In the intermediate region ($\sim E_c \pm 150$ mV), the current transient undergoes an initial current decay followed by the development of a mean steady state value with fluctuations as shown for the hold potentials of 1.02 and 1.04 V for $\text{Ag}_{0.70}\text{Au}_{0.30}$. The transition in behavior from purely decay to a decay which develops a steady-state current was observed between potentials of 0.99 and 1.02 V. At a potential of 1.02 V, the current reaches a plateau after approximately 5400 seconds. The same transition for $\text{Ag}_{0.75}\text{Au}_{0.25}$ is observed between potentials 0.93 and 0.94 V. The “incubation time” for current to reach a plateau was much less than that observed for $\text{Ag}_{0.70}\text{Au}_{0.30}$. The plateau is reached approximately after 1500 seconds for $\text{Ag}_{0.75}\text{Au}_{0.25}$. Prior to this plateau, the current is potential independent in agreement with statements in the literature^{69,73}. However, if one holds long enough to observe the steady-state current of the plateau, we find that the current is in fact potential dependent. As the potential is increased from 1.02 V to 1.04 V for $\text{Ag}_{0.70}\text{Au}_{0.30}$, from 0.94V to 0.95 V for $\text{Ag}_{0.75}\text{Au}_{0.25}$ and from 0.79V to 0.82 V for $\text{Ag}_{0.80}\text{Au}_{0.20}$, the plateau current more than doubles and the time to reach the plateau

shortens by a factor of more than 2. We should point out that both of these potentials are below conventionally defined E_c (see Figure 2-9). Prior to the plateau, the current decay data is very reproducible as shown. Also, shown in Figure 5-1 is the reproducibility in the data for the onset of the plateau for the two holds performed at 1.04 V. Interestingly, this behavior appears to be developing in the data of Moffat et.al⁷³ but was missed since the potential was held for only a few hours (although their data appears to be some of the longest holds we found in the literature).

Comparison of current-time transients obtained for three different alloys revealed a number of interesting facts. These observations were:

- The steady-state plateau current of both $Ag_{0.20}Au_{0.80}$ and $Ag_{0.25}Au_{0.75}$ is not as leveled (horizontal) as that of $Ag_{0.30}Au_{0.70}$. For both alloys, the plateau current seems to decay for a while until it recovers itself and reaches some sort of an average value.
- The current transients for $Ag_{0.30}Au_{0.70}$ obtained at potentials of 0.79 V, 0.94 V, and 1.02 V, all of which are below the CP, exactly fall upon each other and decay with a slope of approx. -0.75. On the other hand, the slope of the current decay has slightly changed as the applied potential approach to the CP for both $Ag_{0.20}Au_{0.80}$ and $Ag_{0.25}Au_{0.75}$.
- A number of “blips” have been observed in all our current transients obtained at both above and below the critical potential. Interestingly, Erlecbacher⁷⁴ also observed same kind of “blips” in simulated dissolution flux curve at very early times ($t < 10$ sec). He observed two main “blips” before the dissolution flux reached a steady-state. It is proposed that those two bumps are caused by dissolution of the LN atoms from the first and second layers of alloy, respectively.

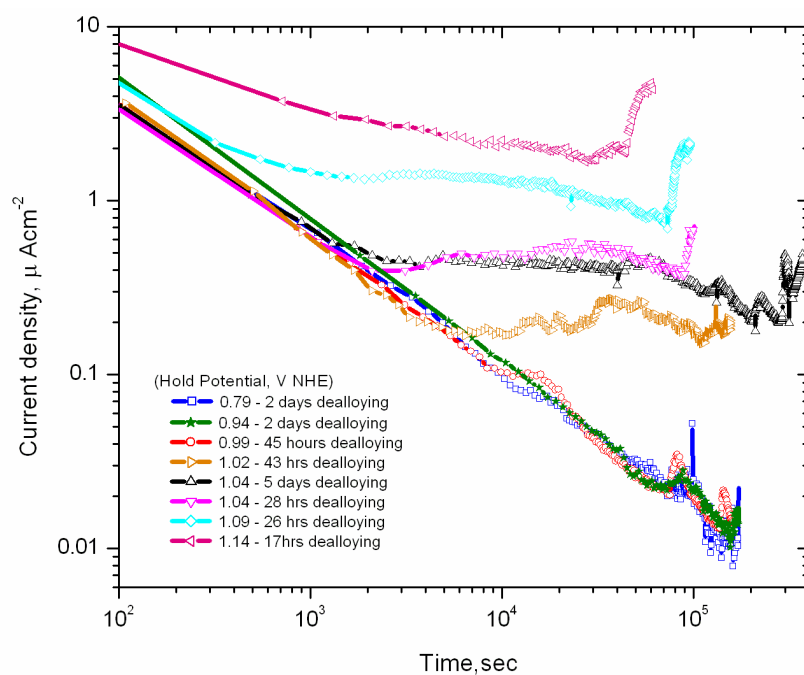


Figure 5-1 Current decay behavior for $\text{Ag}_{0.70}\text{Au}_{0.30}$ held at the indicated potentials (vs NHE) in 0.1 M HClO_4 . The above data shows that the critical potential for this alloy is between 0.99 V and 1.02 V. The two sets of data taken at 1.04 V represent the typical reproducibility of the measurements.

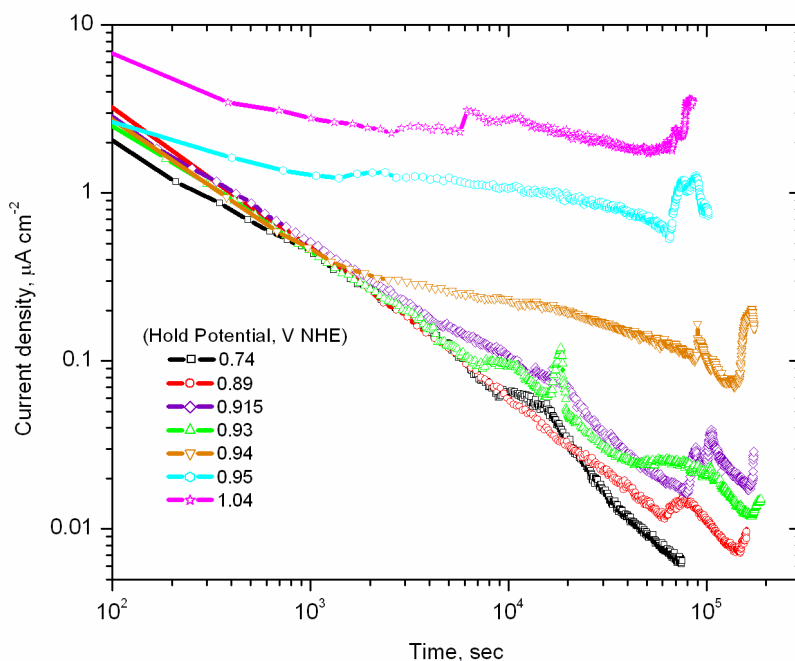


Figure 5-2 Current decay behavior for $\text{Ag}_{0.75}\text{Au}_{0.25}$ held at the indicated potentials (vs NHE) in 0.1 M HClO_4 . The above data shows that the critical potential for this alloy is between 0.93 V and 0.94 V.

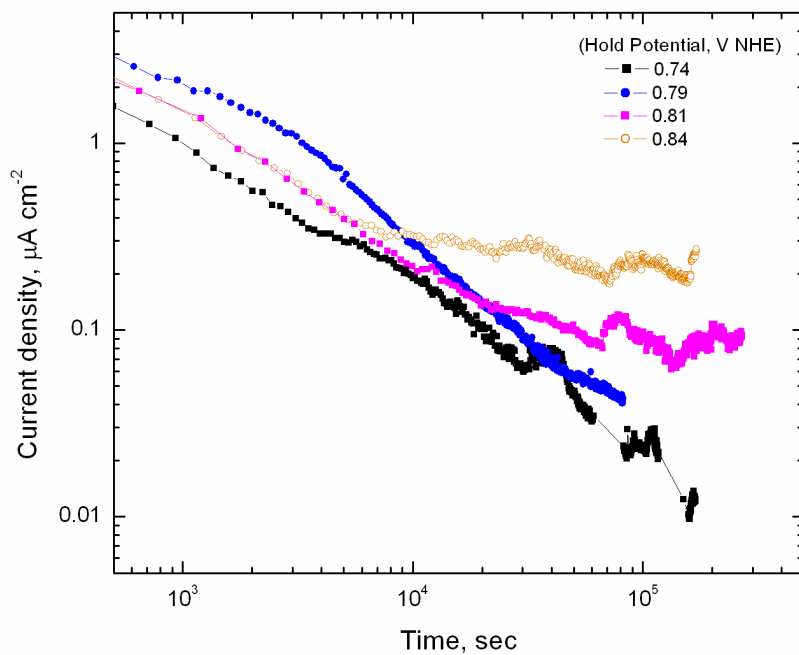


Figure 5-3 Current decay behavior for $\text{Ag}_{0.80}\text{Au}_{0.20}$ held at the indicated potentials (vs NHE) in 0.1 M HClO_4 . The above data shows that the critical potential for this alloy is between 0.79 V and 0.81 V.

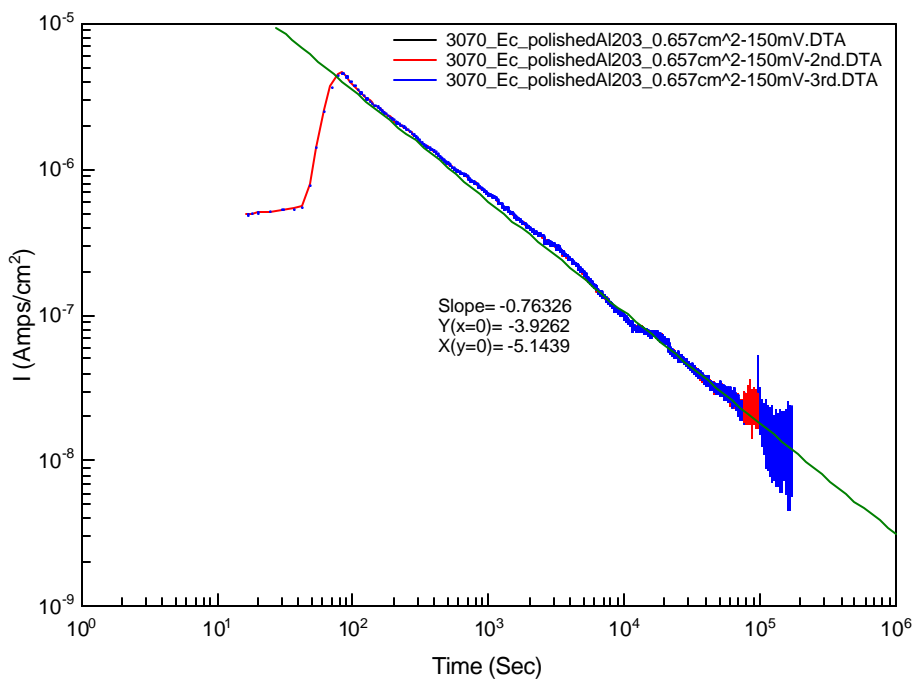
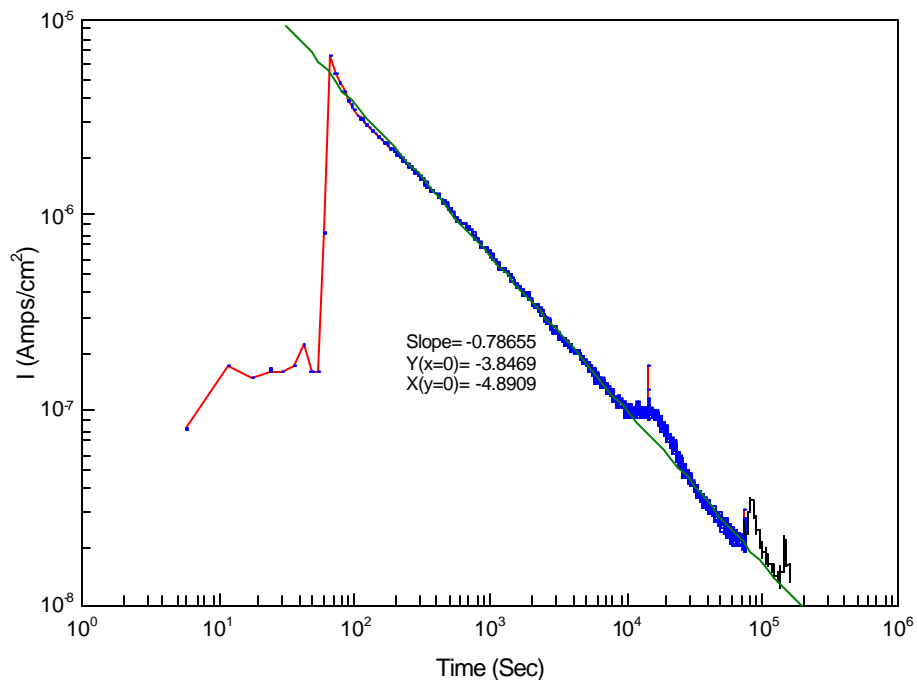


Figure 5-4 Current-time transient for $\text{Ag}_{0.70}\text{Au}_{0.30}$ obtained at (a) $350 \text{ mV}_{\text{MSE}}$ (b) $150 \text{ mV}_{\text{MSE}}$ in 0.1 M HClO_4 .

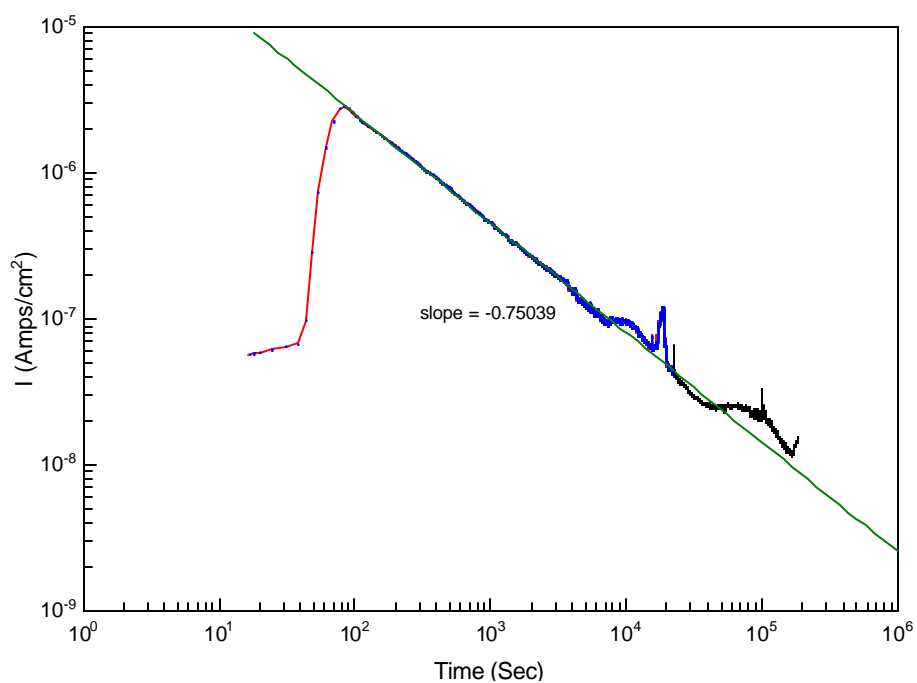
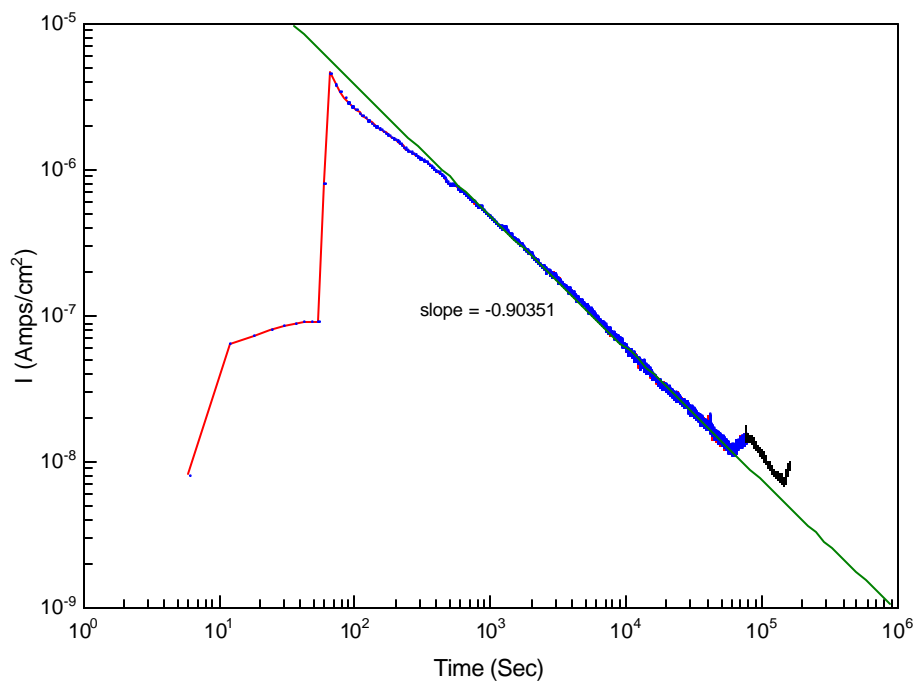


Figure 5-5 Current-time transient for $\text{Ag}_{0.75}\text{Au}_{0.25}$ obtained at (a) $100 \text{ mV}_{\text{MSE}}$ (b) $250 \text{ mV}_{\text{MSE}}$ in 0.1 M HClO_4 .

Figure 5-6, Figure 5-7, and Figure 5-8 show typical alloy polarization curves for $\text{Ag}_{0.70}\text{Au}_{0.30}$, $\text{Ag}_{0.75}\text{Au}_{0.25}$ and $\text{Ag}_{0.80}\text{Au}_{0.20}$ in 0.1 M HClO_4 at a potential scan rate of 1mV sec^{-1} . Multiple curves in each of the figures represent the minimum and maximum difference in the polarization curves that we observed, i.e. the reproducibility in our measurements. Region “B” (1.10 V–1.14 V for $\text{Ag}_{0.70}\text{Au}_{0.30}$, 1.02 V–1.06 V for $\text{Ag}_{0.75}\text{Au}_{0.25}$ and 0.85 V–0.885 V for $\text{Ag}_{0.80}\text{Au}_{0.20}$) in these plots shows the range of critical potential values that one would obtain using the standard method for extrapolating the rapidly rising current. These would represent the values of E_c , typically reported in the literature for this system. Region “A” (0.99 V–1.02 V for $\text{Ag}_{0.70}\text{Au}_{0.30}$, 0.93 V–0.94 V for $\text{Ag}_{0.75}\text{Au}_{0.25}$ and 0.79V–0.81V for $\text{Ag}_{0.80}\text{Au}_{0.20}$) shows the actual location of the critical potential, E_{crit}^* , based on the potential hold experiments displayed in Figure 5-1, Figure 5-2 and Figure 5-3. These data clearly show that the critical potential is being overestimated by approximately 100 mV. The estimated values of conventionally defined critical potential (E_c) determined from the polarization data and “true” critical potentials E_{crit}^* , based on the potential hold experiments are summarized in Table 5-1.

Table 5-1 Critical Potentials values obtained using three different methods

Alloy Composition	Sieradzki’s Critical Potential, $E_{1.0\text{mA/cm}^2}$, V	Conventionally defined Critical Potential, E_c , V	“True” Critical Potential, E_{crit}^* , V
$\text{Ag}_{0.20}\text{Au}_{0.20}$	1.22	0.85-0.885	0.79-0.81
$\text{Ag}_{0.25}\text{Au}_{0.75}$	1.20	1.02-1.06	0.93-0.94
$\text{Ag}_{0.30}\text{Au}_{0.70}$	1.06-1.12	1.1-1.14	0.99-1.02

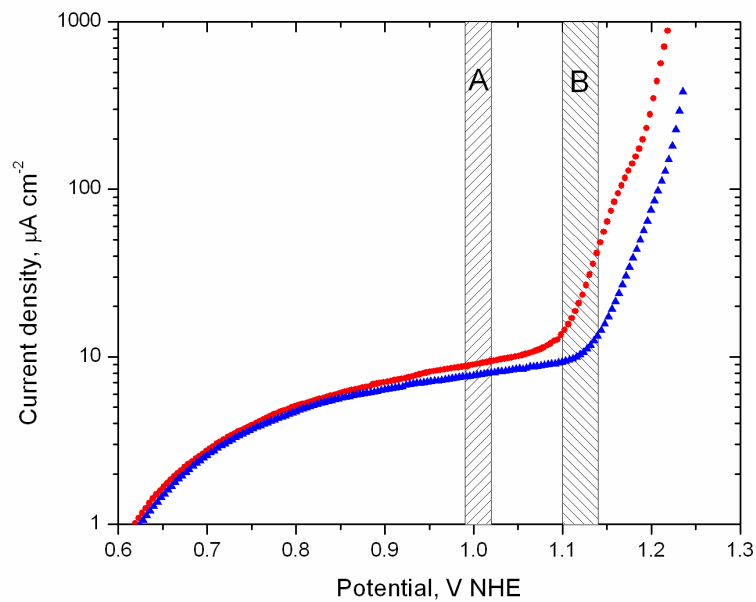


Figure 5-6 Anodic polarization data for $\text{Ag}_{0.70}\text{Au}_{0.30}$ in 0.1 M HClO_4 . Scan rate = 1mV sec^{-1} . Region A (0.99 V – 1.02 V) corresponds to the identified region of the critical potential as determined by the potential hold data of Figure 5-1. Region B (1.1 V – 1.14 V) corresponds to the region of the critical potential determined by the extrapolation of the polarization data.

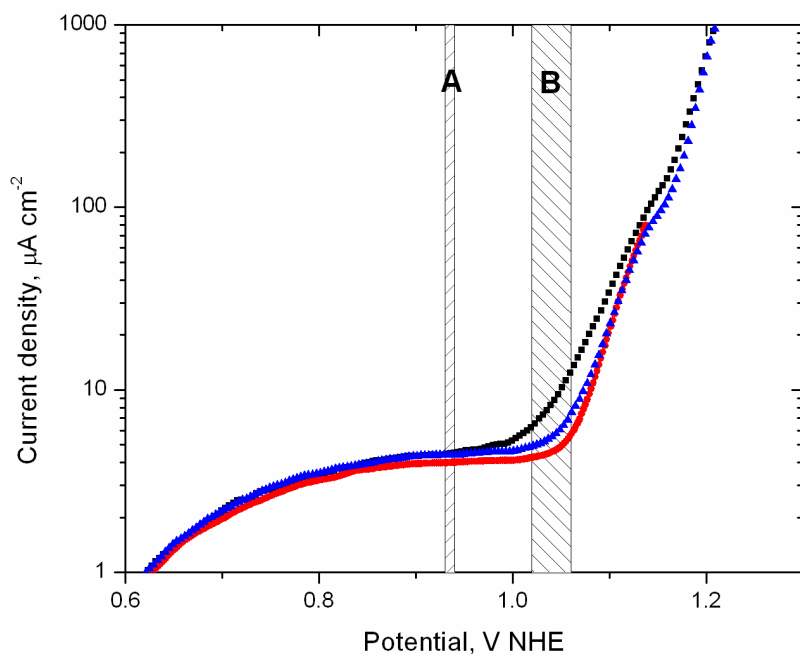


Figure 5-7 Anodic polarization data for $\text{Ag}_{0.75}\text{Au}_{0.25}$ in 0.1 M HClO_4 . Scan rate = 1mV sec^{-1} . Region A (0.93 V – 0.94 V) corresponds to the identified region of the critical potential as determined by the hold data of Figure 5-2. Region B (1.02 V – 1.06 V) corresponds to the region of the critical potential determined by the extrapolation of the polarization data.

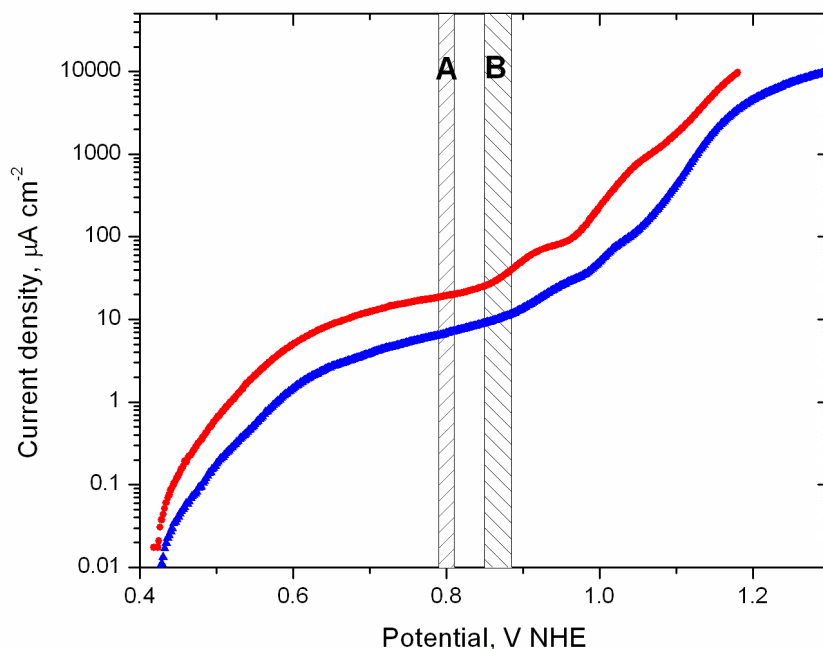


Figure 5-8 Anodic polarization data for $\text{Ag}_{0.80}\text{Au}_{0.20}$ in 0.1 M HClO_4 . Scan rate = 1mV sec^{-1} . Region A (0.79 V – 0.81 V) corresponds to the identified region of the critical potential as determined by the hold data of Figure 5-3. Region B (0.85 V – 0.885 V) corresponds to the region of the critical potential determined by the extrapolation of the polarization data.

5.4 Morphology Above The “True” Critical Potential

Resultant surface morphology of a dealloyed $\text{Ag}_{0.70}\text{Au}_{0.30}$, which is subjected to a constant hold potential at 1.04 V for about 36 hours in 0.1 M HClO_4 , solution is shown in Figure 5-9 (a). The sample was heat treated after dealloying for 10 minutes at $250\text{ }^\circ\text{C}$ to coarsen the pores to a size that is observable with SEM. Interestingly, rather than a bicontinuous porous structure, we observed a pitting like surface morphology. Typically, the pits are characteristic of an alloy surface dealloyed at potentials below the CP. However, when we cracked the alloy and looked below the surface, we confirmed the bicontinuous nature of the porosity that is typical of dealloyed systems.[see Figure 5-9(b) and (c)]. We believe that the observed pitting like surface morphology at this potential ($E^*_{\text{crit}} < E < E_c$), is due to relaxation of the porosity at these low dealloying rates. That is if we consider the 1.04 V potential hold data, we can approximate the plateau current as $0.4\text{ }\mu\text{A cm}^{-2}$ which corresponds to a Ag dissolution rate of 2.2 nm per hour.

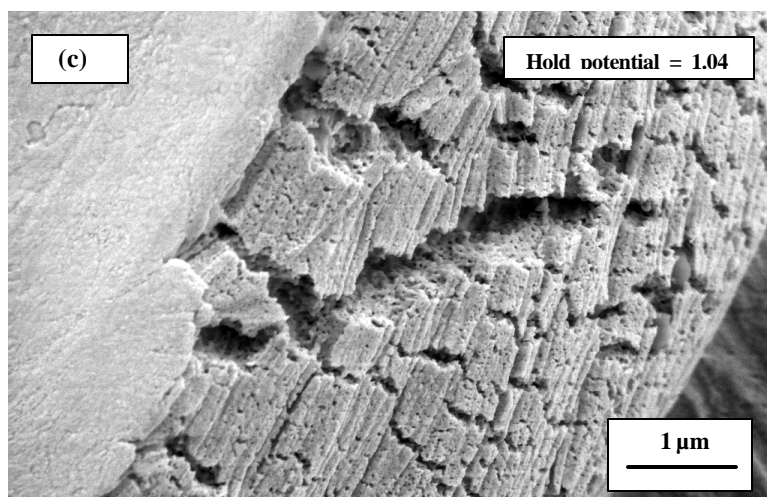
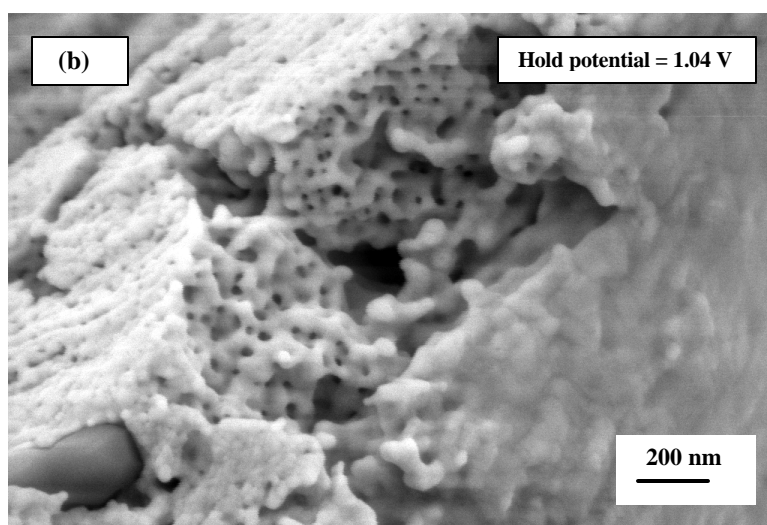
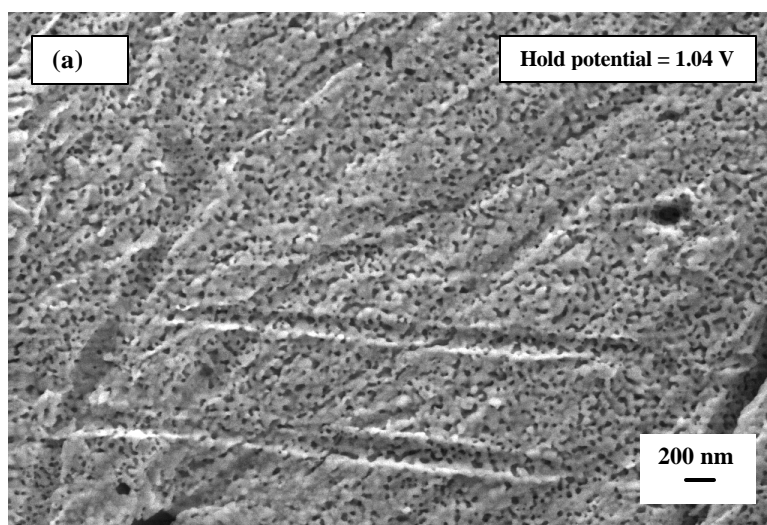


Figure 5-9 Resultant morphology of $\text{Ag}_{0.70}\text{Au}_{0.30}$ after subjected to a potential of $1.04 \text{ V}_{\text{MSE}}$ in 0.1 M HClO_4 .

Similarly, the same pitting morphology was observed on the surface of $\text{Ag}_{0.70}\text{Au}_{0.30}$, dealloyed at 0.79 V which is well below the “true” critical potential, E_{crit}^* . [Figure 5-10]. It is believed that these pits, as opposed to the previous SEM image, represent fluctuations in the composition of the alloy. Because the pits are isolated and no penetration of an interconnected 3-D porous structure was observed. As manifested in our chronoamperometric (current transient) results, the transition from pitting like morphology to morphology with bicontinuous porosity was shown to be marked by a deviation from a current decay to a decay which develops a steady state current. As suggested by Erlebacher⁷⁴ this transition can also be seen in simulated charge vs time plots obtained by integration of current-time transients. [see Figure 5-11]. Simulation results revealed that while the integrated flux (i.e. charge) continues to rise during porosity evolution, it levels off during passivation. Such a measurement eliminates the noise seen in low dissolution currents such as seen in Figure 5-1. For the sake of direct comparison to simulation results, we followed the same procedure for defining the transition from passivation to dealloying. Figure 5-12, Figure 5-13, Figure 5-14 show charge density vs time plots of the three alloy systems. Comparison of Figure 5-1 and Figure 5-12, Figure 5-13, Figure 5-14 reveals that our experimental results agree quite satisfactorily with simulation results.

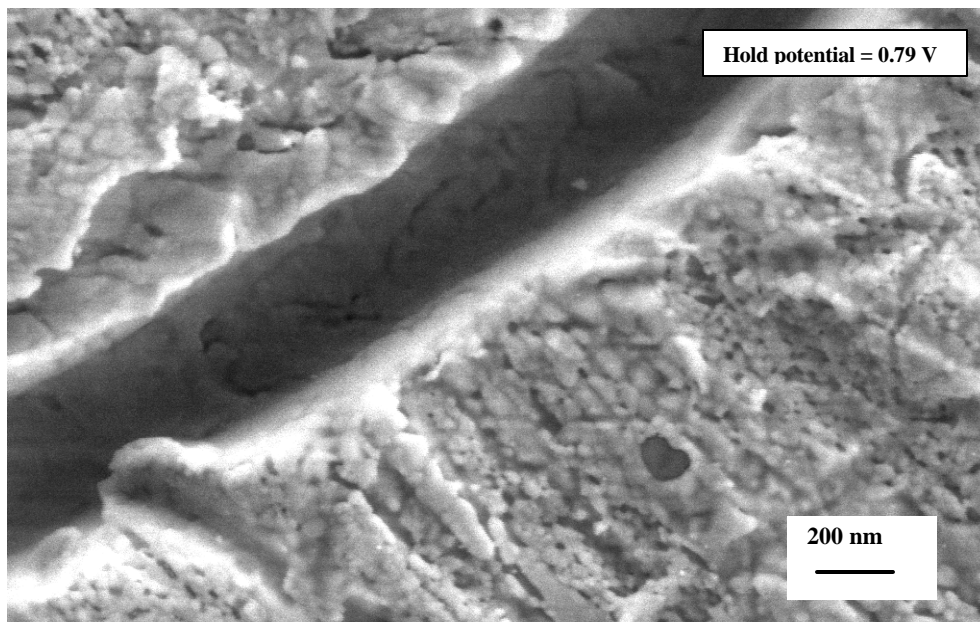


Figure 5-10 Resultant surface morphology of $\text{Ag}_{0.70}\text{Au}_{0.30}$ after subjected to a potential of 0.79 V_{MSE} in 0.1 M HClO_4 .

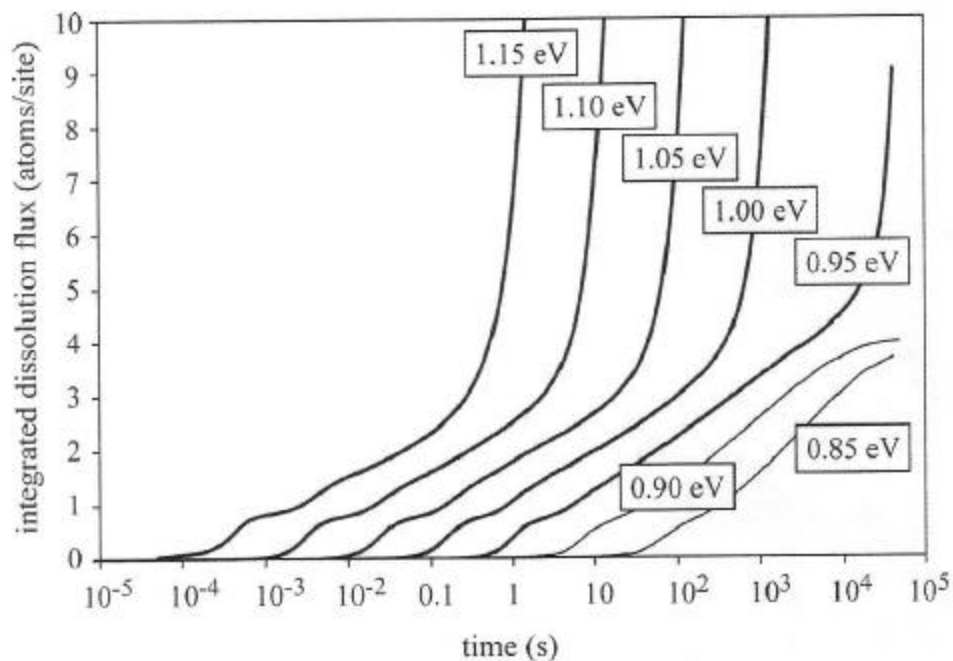


Figure 5-11 Erlebacher simulation result showing integrated dissolution vs. time for $\text{Ag}_{0.75}\text{Au}_{0.25}$ and applied potentials between 1.2 eV and 0.85 eV. The true critical potential sits between 0.90 eV and 0.95 eV.

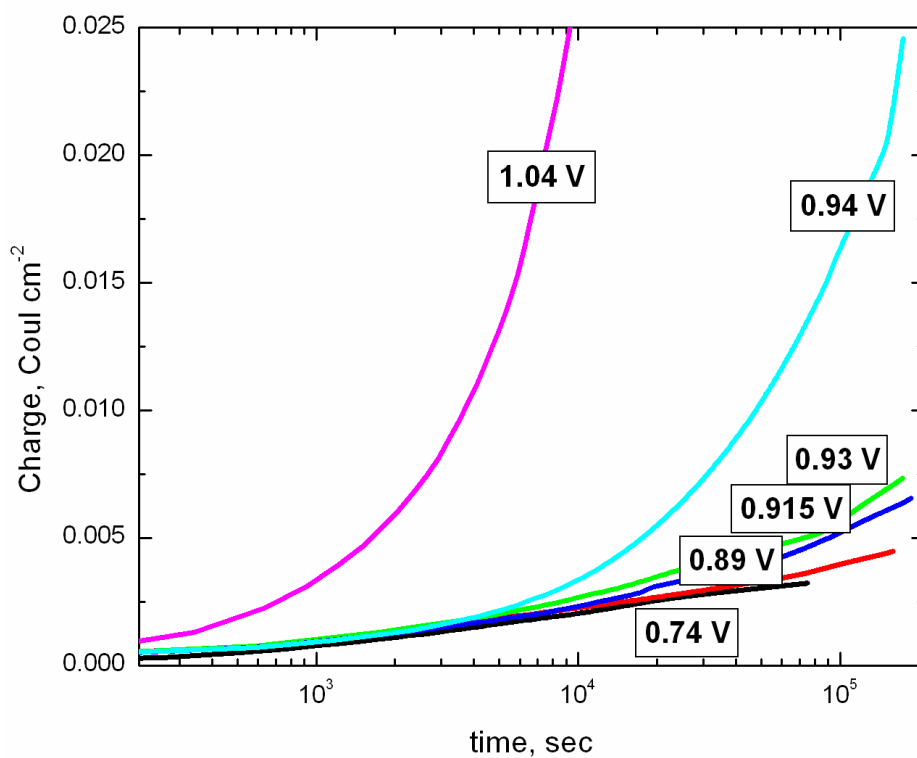


Figure 5-12 Charge density transients for $\text{Ag}_{0.75}\text{Au}_{0.25}$ obtained by integration of the current-time transients in Figure 5-2.

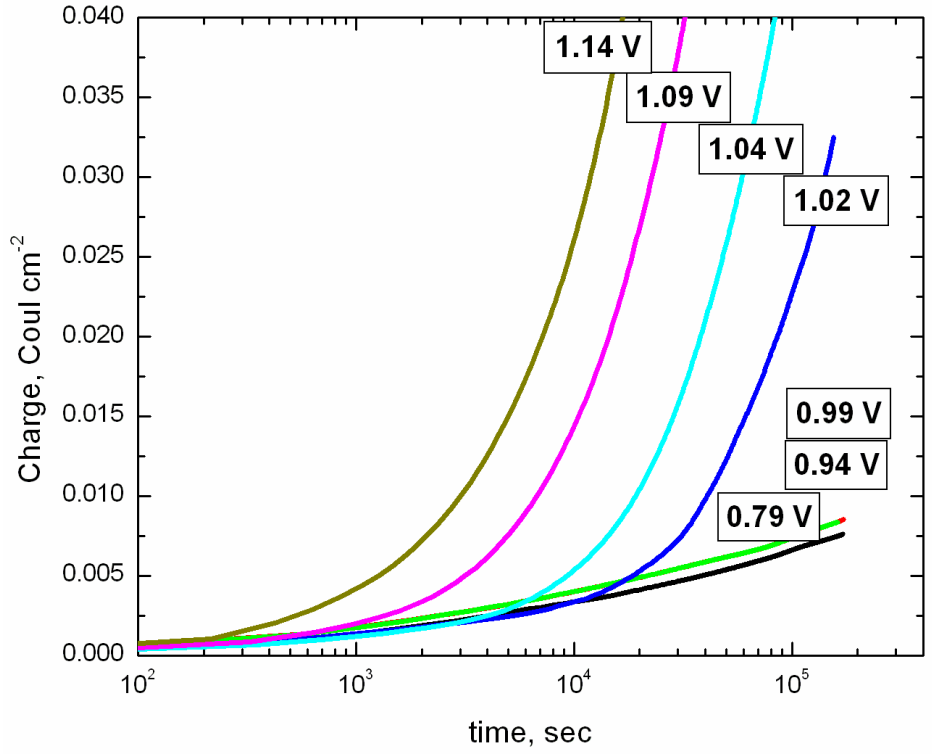


Figure 5-13 Charge density transients for $\text{Ag}_{0.70}\text{Au}_{0.30}$ obtained by integration of the current-time transients in Figure 5-1.

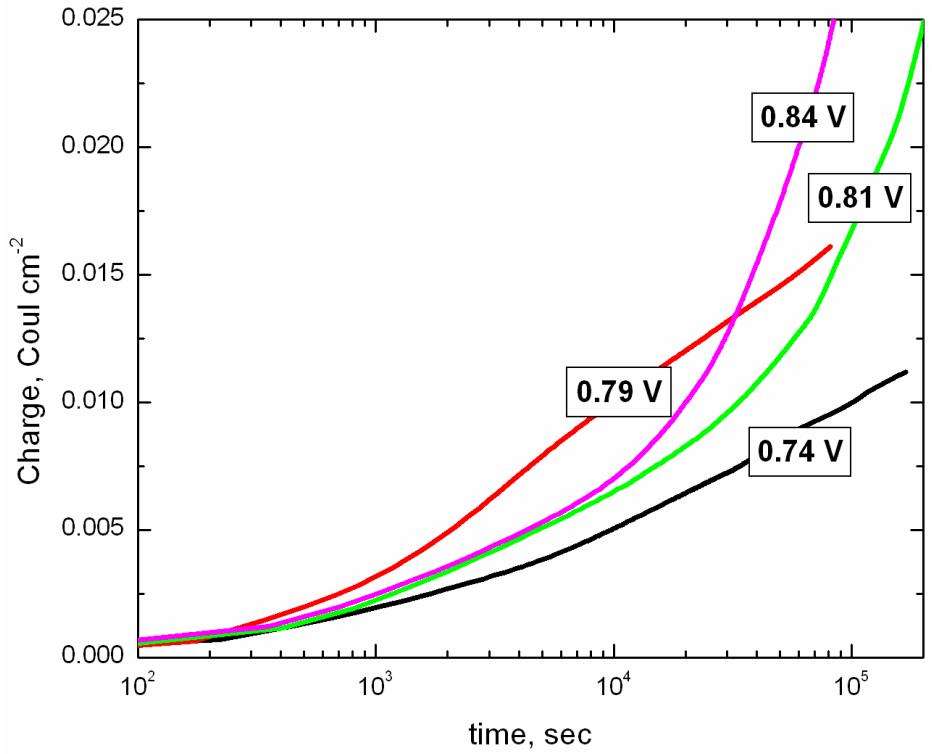


Figure 5-14 Charge density transients for $\text{Ag}_{0.80}\text{Au}_{0.20}$ obtained by integration of the current-time transients in Figure 5-3.

The above results raise some arguments about the critical potential studies performed on alloy systems in the literature. We argue that the experimental systems in the literature were not dealloyed for sufficiently long times as to evolve porosity. As a result of this, no shift was observed from a purely current decay to steady-state behavior in current-transients measured at potentials in the vicinity of CP. This in turn resulted in errors in reported critical potential values. The literature also speculated about the mechanism of dealloying just by analyzing current-time transients in the very early stages of dissolution process. Whereas, our potential hold experiments show that surface evolution during passivation and porosity evolution are very similar at early stages of dealloying. This can also be seen from our current-time plots in which the currents transients measured at potentials both above and below the CP run approximately parallel at the early stages of the dissolution process.

The second argument is that pitting like morphologies observed on the alloy systems using STM technique does not necessarily mean that the porosity is not bicontinuous and does not extend beyond the surface. We observed similar surface morphologies in alloy systems dealloyed at both above and below the CP. However the difference between porosity evolution ($E > E_{crit}^*$) and passivation ($E < E_{crit}^*$) is not observed until we cracked the alloy and looked below the surface.

The main problem with STM is that they do not have the depth of field (owing to tip convolution issues) to distinguish between porosity versus a nanometer roughened surface. Therefore, one is limited to characterizing the surface and then speculating on the relationship to the fully developed 3-dimensional structure. This is a serious issue considering that the surface will relax resulting in a different morphology than expected if we were to take an imaginary 2-dimensional slice through the bulk structure. Comparison of Figure 5-8 (b) and Figure 5-15 shows the difficulties with the STM for use in investigating the morphology of bulk dealloyed materials.

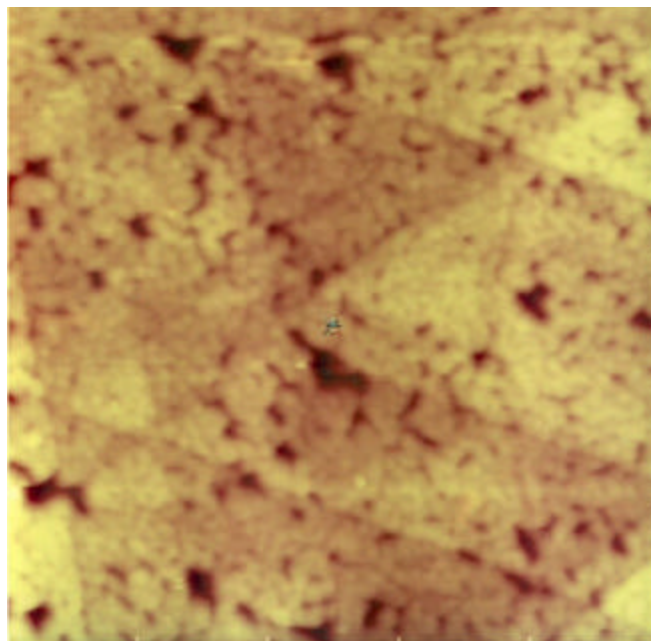


Figure 5-15 STM Images of the resultant surface morphology of a $\text{Ag}_{0.16}\text{Au}_{0.84}$ alloy after selective dissolution of the Ag atoms in 0.1 M HClO_4 . Reprinted from [22]

Although, SEM was good enough for the current study, it also has some drawbacks. First, the dealloyed samples have to be heat treated in order to increase the pore size that is observable under SEM. However, we don't know exactly how these measurements relate back to room temperature. This could be a serious problem especially in determining the pore size and distribution obtained at high overpotentials. The porosity at those potentials is known to be as small as 3 nm which is far beyond the SEM resolution. In order to solve this problem, another characterization technique, namely Small Angle Neutron Scattering (SANS) was used to characterize bulk porosity after dealloying of AgAu systems at different potentials and in different electrolytes. Detailed information about SANS analysis can be found in Chapter 3.

Figure 5-16 and Figure 5-17 show the steady-state plateau currents extracted from Figure 5-1 and Figure 5-2. The anodic polarization curves were also plotted in the same figures. It is found that the steady-state plateau currents closely follow the exponentially rising dissolution currents at potentials above approximately 1.0 V. However, deviation from the polarization curve is observed at low overpotentials. This deviation is believed to be related to coupling effects between surface diffusivity of the more noble element and the sweep rate, i.e, the rate of change of the applied potential. During anodic polarization, at low overpotentials especially in the vicinity of CP, the scan rate is so fast that the alloy system can not responds quickly. That is there is not enough time for gold adatoms, which are formed during the initial potential ramp, to diffuse and close up the silver dissolution sites thereby preventing porosity formation. On the other hand, during potential hold experiments, the gold adatoms have plenty of time to diffuse on the surface to aggregate into Au rich islands and expose new Ag atoms beneath the alloy surface to the electrolyte.

Another reason for this deviation could be due to increase of the Ag ion concentration in the electrolyte during potential hold experiments. Increase in Ag^+ concentration during the selective dissolution process will increase the exchange current density for the Ag dissolution reaction and hence result in an overall increase in the Ag dissolution rate.

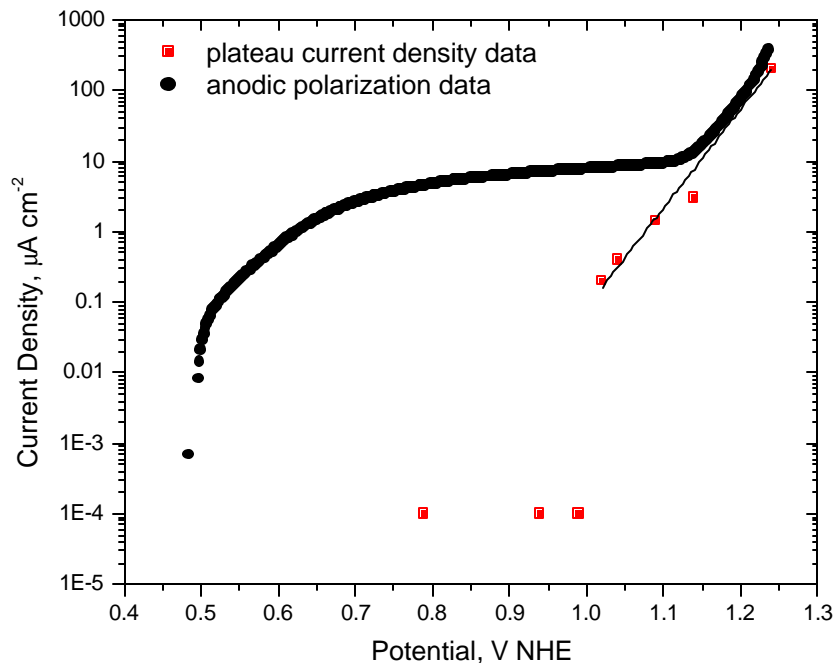


Figure 5-16 Plateau current density as extracted from Figure 5-1 versus potential for $\text{Ag}_{0.70}\text{Au}_{0.30}$. Anodic polarization curve is also shown for comparison. The fit is exponential.

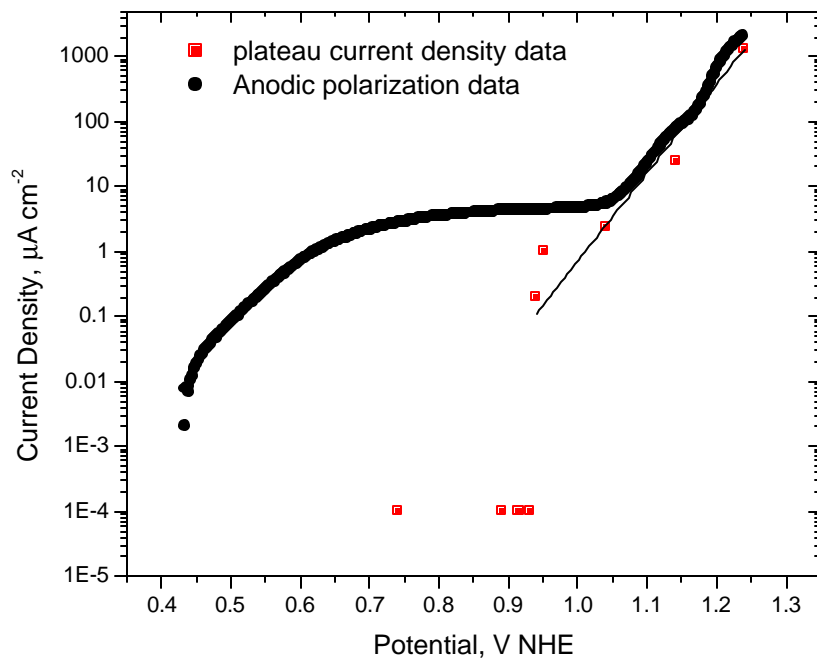


Figure 5-17 Plateau current density as extracted from Figure 5-2 versus potential for $\text{Ag}_{0.75}\text{Au}_{0.25}$. Anodic polarization curve is also shown for comparison. The fit is exponential.

Interestingly, a critical dissolution rate below which no porosity forms, has been observed for both alloy systems as seen in Figure 5-16 and Figure 5-17. This critical dissolution rate is found to be approximately $0.12 \mu\text{A cm}^{-2}$. We believe that this value is a constant cut-off dissolution rate valid for Ag-Au alloy systems as long as silver atom fraction is above the threshold value. This allow us to make an easy and rough approximation of the true critical potential by determining the potential corresponding to this cut-off dissolution rate.

It is worth noting here that the critical potential was defined as the value of the potential corresponding to a current density of 1mA cm^{-2} in “percolation model” developed by Sieradzki³⁰ which is in author’s opinion the most promising mechanism to date. This value however, is much larger than what we have found. The estimated values of Sieradzki’s critical potentials and our true critical potentials are tabulated in Table 5-1.

Taking this fact into account we attempt to have a closer look at the equation (4.3) for the critical overpotential, recently redeveloped by Sieradzki et.al⁵²

For our system (Ag-Au) the variables take the values: $W = 1.685 \cdot 10^{-29} \text{ m}^3$, $q = 1.602 \cdot 10^{-19} \text{ C}$, $n = 1$, $a = 2.880 \cdot 10^{-10} \text{ m}$, $k = 1.381 \cdot 10^{-23} \text{ J K}^{-1}$, $N_s = 1.395 \cdot 10^{19} \text{ m}^{-2}$, $D_s = 2 \cdot 10^{-20} \text{ m}^2 \text{ sec}^{-1}$, $T = 298 \text{ K}$, and $\gamma \cong 1 \text{ Jm}^{-2}$. This leaves δ and J_0 as fitting parameters. Using the above parameter values, our experimentally determined true critical potentials have been fitted to the equation in order to determine the unknown quantities δ and J_0 . Figure 5-18 shows this fit to our data. The two fitting parameters δ and J_0 has been obtained as $1.93 \cdot 10^{-10}$ and $2.0 \cdot 10^{16} \text{ #atoms m}^{-2} \text{ sec}^{-1}$, respectively. Converting this mass flux (J_0) to exchange current density yields a value of $3.2 \cdot 10^{-7} \text{ A cm}^{-2}$. Gerisher and Tischer⁷⁵ reported a value for the exchange current density for the Ag/Ag⁺ electrode in 1N HClO₄ of 0.15 A cm^{-2} for a solution containing 10^{-3} M Ag^+ and 4.5 A cm^{-2} for a solution containing 10^{-1} M Ag^+ .

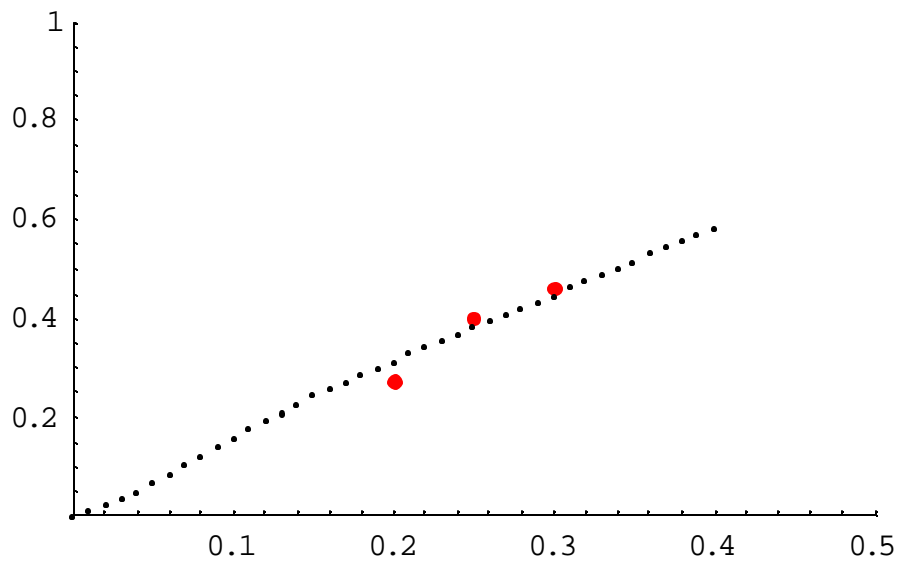


Figure 5-18 Overpotential versus alloy composition data fitted to equation (4.3).

CHAPTER 6 POTENTIAL DEPENDENT COARSENING OF POROUS AG-AU ALLOYS

6.1 Estimation of Surface Diffusivity of Gold as a Function of Dealloying Potential

As it was discussed in section 4.3, we argue that the change in size scale that one may observe with changes in dealloying rate (i.e through changing the dealloying potential) is most likely a result of the potential dependence of the diffusivity.

The surface diffusivity for gold has been measured via relaxation of roughened surfaces and has been shown to depend strongly on the applied potential^{64,66}. The change in the surface diffusivity is attributed to the change in interaction of surface gold adatoms with the species in the electrolyte with applied potential. The diffusion coefficients reported in the literature were in the range of 10^{-15} to 10^{-13} $\text{cm}^2 \text{sec}^{-1}$ depending on the applied potential.

Corcoran et.al¹⁸ used in-situ Small Angle Neutron Scattering (SANS) to characterize the morphological evolution of $\text{Ag}_{0.70}\text{Au}_{0.30}$ alloy under the conditions of selective dissolution in 0.1 M HClO_4 + 1mM Ag^+ . The SANS data were recorded over a period of 39 h. The SANS results showed that the structure, which was dealloyed first at an elevated potential, showed significant coarsening with time when the potential is lowered to 450 mV. The kinetics of the coarsening was found to follow the relationship: ligament size(l) a $t^{0.25}$, which indicates that the coarsening of dealloyed structures is surface dominated.

In order to explore the effect of dealloying potential on the surface diffusivity of Au adatoms hence the resultant porosity in the dealloyed structure, we performed a series of potential hold experiments on both 30Au70Ag and 35Au65Ag alloys in 0.1 M HClO_4 electrolyte. Alloy samples were subjected to five different dealloying potentials, all of which are above the critical potential, for a period of time in the electrolyte.

Table 6-1 and Table 6-2 give the history of electrochemical treatment performed on the samples.

Table 6-1 Effect of Dealloying Potentials on Surface Diffusivities for $\text{Ag}_{0.70}\text{Au}_{0.30}$ alloy. All samples are dealloyed in 0.1 M HClO_4 for the indicated time.

Dealloying Potential, mV	Dealloying time, hr	Ligament size, nm	$D_s \times 10^{-16}, \text{cm}^2 \text{sec}^{-1}$
550	24	17.2	7.57
655	3	2.8	3.8×10^{-2}
685	3		
750	2	2.3	5.7×10^{-2}

Table 6-2 Effect of Dealloying Potentials on Surface Diffusivities for $\text{Ag}_{0.65}\text{Au}_{0.35}$ alloy. All samples are dealloyed in 0.1 M HClO_4 for the indicated time

Dealloying Potential, mV	Dealloying time, hr	Ligament size, nm	$D_s \times 10^{-16}, \text{cm}^2 \text{sec}^{-1}$
450(S1_3)	32.5	16.3	4.5
600(S1_1)	32.5	9.5	0.52
655(S1_5)	15	3.3	1.58×10^{-2}
800(S1_25)	3	1.7	3.12×10^{-3}

Figure 6-1 shows pictures of the samples after dealloying process. The change in the color indicates that they have different size scale of porosity due to different applied potentials. We performed SANS measurements to determine the exact ligament size in these samples. Differently than Corcoran's¹⁸ study, ex-SANS measurements were used after dealloying experiments since the in-situ SANS measurements take longer times and our SANS time was limited to only two days.

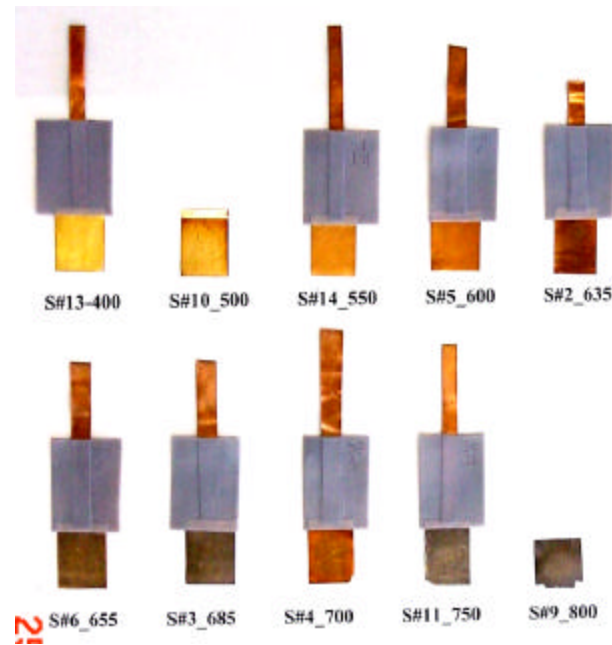


Figure 6-1 $\text{Ag}_{0.70}\text{Au}_{0.30}$ samples dealloyed at the indicated potentials in 0.1 M HClO_4 .

Figure 6-2 and Figure 6-3 show the absolute scattered intensity profiles for both alloys as a function of scattering angle (2Θ) and a wave number q , which is equal to $[(4\pi / \lambda) \sin\Theta]$, where λ = wavelength of the neutron beam in the medium. The peak in the scattering indicates that the porosity (ligament) has a well-defined average size, l .

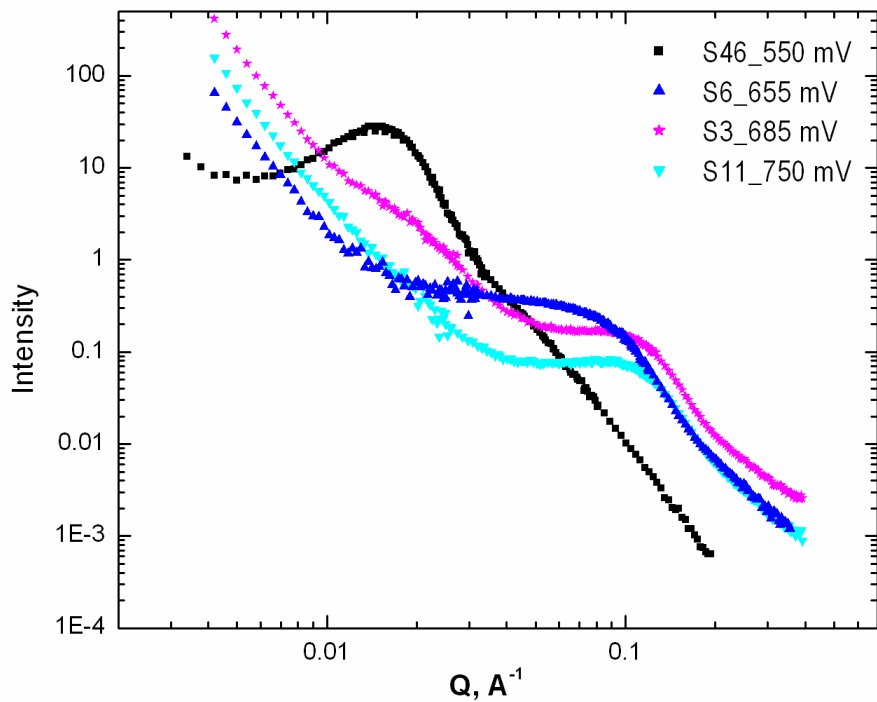


Figure 6-2 Small angle neutron scattering from porous $\text{Ag}_{0.70}\text{Au}_{0.30}$ alloy dealloyed at the indicated potentials in 0.1 M HClO_4 .

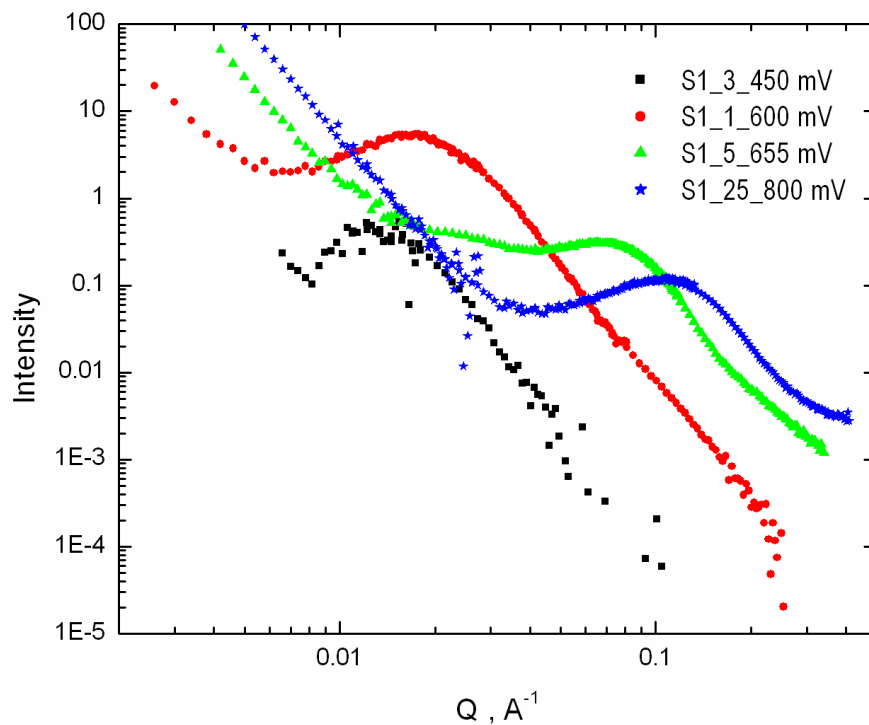


Figure 6-3 Small angle neutron scattering from porous $\text{Ag}_{0.65}\text{Au}_{0.35}$ alloy dealloyed at the indicated potentials in 0.1 M HClO_4 .

Shifting of the peak position to smaller values indicates that the porosity is coarsened with dealloying potentials. The average ligament size in each dealloyed samples was found by analyzing the SANS data using the leveled wave method of Berk⁵⁶. Data fitted with this model can be found in Appendix A. The results are summarized in Table 6-1 and Table 6-2

Based on the fact that the surface diffusivity of the remaining element (Au in our case) dominates the resultant size scale of porosity created during the dealloying, surface diffusivity of gold was determined using equation(4.1). The present results show that diffusivity of gold decreases with applied potential.

The decrease in diffusivity with potential is seemingly in contrast to the literature^{64,66}. However, the maximum potential used in the literature was 194 mV_{MSE} which is much lower than the potentials we used during dealloying. Therefore, no reliable quantitative comparison of surface diffusivity data is possible. In the next sections, coarsening of these dealloyed structures have also been studied at much lower potentials.

What was most surprising about these results is that no significant coarsening is observed at the elevated dealloying potentials of 750 mV, 685 mV and 655 mV for Au_{0.30}Ag_{0.70} and at potentials of 800 mV, 655 mV for Au_{0.35}Ag_{0.65}. The average ligament width was found to be in the range of 1.7 to 3.3 nm at these high potentials. The initial pore size is approximated by percolating cluster size, x , and found to be 1.6 nm and 1.4 nm for Ag_{0.3}Au_{0.7} and Ag_{0.35}Au_{0.65}, respectively. One possible explanation for the “freezing” of the porosity at these elevated potentials could be the gold oxidation at these potentials. The presence of oxide layer prevents adsorption of ions from electrolyte to the Au adatoms and decreases the mobility of Au surface atoms resulting in a decrease in diffusivity.

Interestingly, a dramatic increase in the ligament size was observed at potential of 600 mV for both alloy systems. We believe that this potential is the onset of the coarsening process for Ag-Au systems.

6.2 Potential Dependent Coarsening of Porous Gold

6.2.1 System: Ag₇₀Au₃₀

In the above study we studied the effect of applied potential on the coarsening of porous gold structures. Surface diffusivity was found to be a strong function of applied potential. It is also found that the structures start to coarsen at a certain potential, which we call it as “onset” potential. Between the initial potential which was 450 mV and this so-called “onset” potential, surface diffusivities of gold found to decrease with potential.

The potentials used in the above study, however, were above the critical potential. That is, as the dealloyed morphology undergoes coarsening, the less noble element is continuously leached from the alloy. In order to eliminate the effect of the dissolution rate on coarsening of dealloyed structures, we performed a series of potential hold experiments on pre-dealloyed Ag_{0.70}Au_{0.30} samples at potentials well below the dealloying potentials.

First the alloys were subjected to a constant applied potential of 750 mV_{MSE} for 2 hours in 0.1 M HClO₄ electrolyte. After preparation of porous structures with an average ligament size of 2.3 nm, the samples were subjected to 5 different coarsening potentials (-600 mV, -420 mV, -20 mV, 90mV, and 185 mV) with respect to the negative and positive zero charge potential of the polycrystalline gold ($E_z = -0.420 \text{ V}_{\text{MSE}}$) in 2 different electrolytes (0.1 M HClO₄, and 0.5 M H₂SO₄). The average ligament size in each coarsened samples was found by analyzing the SANS data using the leveled wave method of Berk⁵⁷. The fits to the SANS data can be found in Appendix A.

Figure 6-4 and Figure 6-5 show the absolute scattered intensity profiles for Ag_{0.70}Au₀ alloy after coarsening at the indicated potentials in 0.1 M HClO₄ and 0.5 M H₂SO₄, respectively.

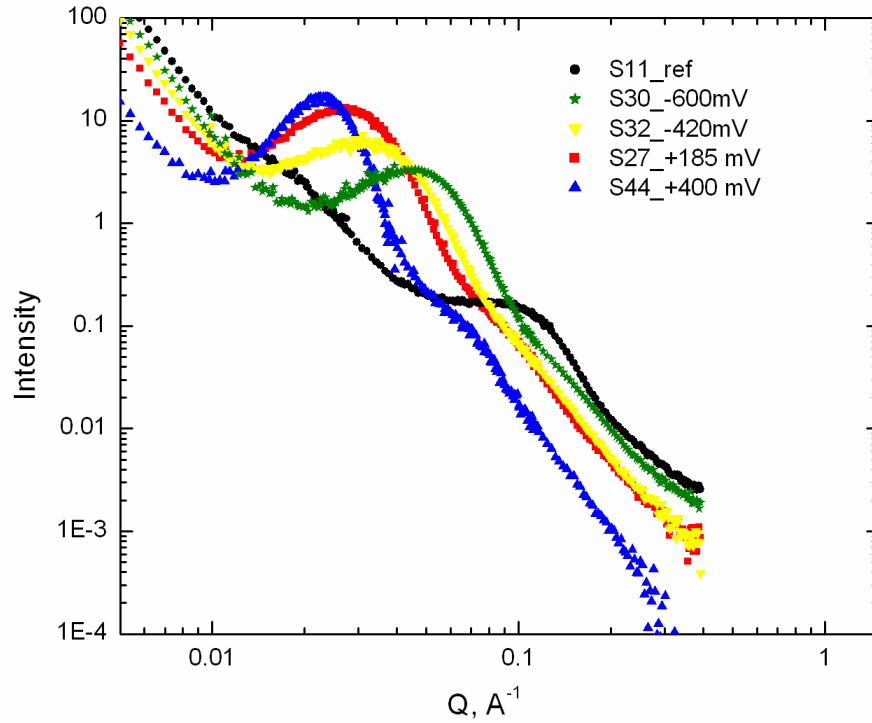


Figure 6-4 Small angle neutron scattering from porous $\text{Ag}_{0.70}\text{Au}_{0.30}$ alloy coarsened at the indicated potentials in 0.1 M HClO_4 .

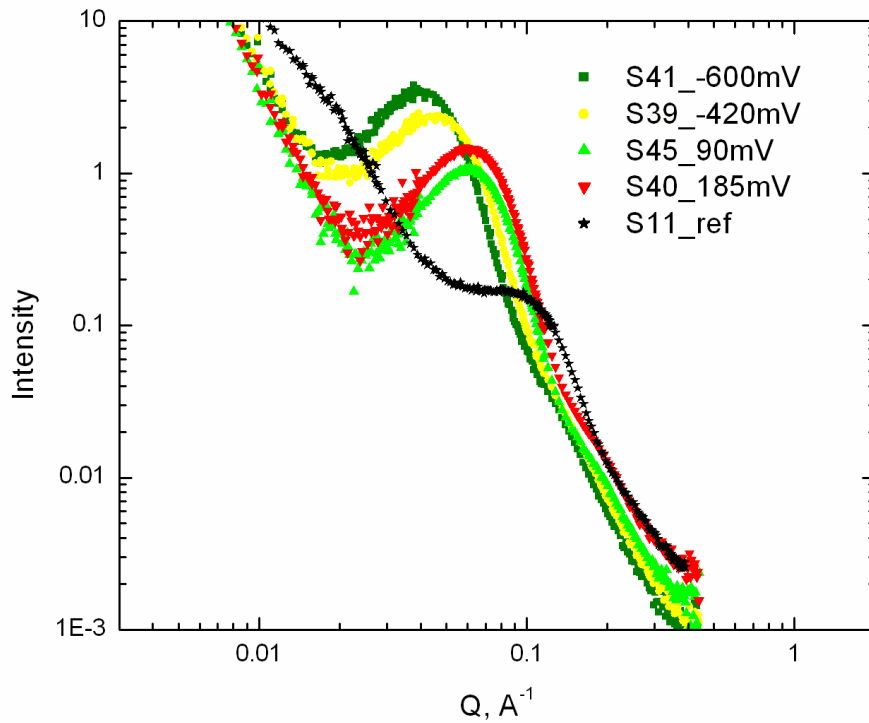


Figure 6-5 Small angle neutron scattering from porous $\text{Ag}_{0.70}\text{Au}_{0.30}$ alloy coarsened at the indicated potentials in 0.5 M H_2SO_4 .

Surface diffusivity of Au at 5 different coarsening potentials was determined using equation (4.1). Table 6-3 shows the values of the surface diffusion coefficients for gold adatoms.

Table 6-3 Values of the Surface Diffusion Coefficients of Gold Adatoms Measured at Different Coarsening Potential Values, in the indicated solutions for $\text{Ag}_{0.30}\text{Au}_{0.70}$

	0.1 M HClO_4		0.5 M H_2SO_4	
Coarsening Potential (V_{MSE})	Ligament size, nm	$D_s \times 10^{-16}$ $\text{cm}^2 \text{sec}^{-1}$	Ligament size, nm	$D_s \times 10^{-16}$ $\text{cm}^2 \text{sec}^{-1}$
-600	5.4	0.34	6.15	0.58
-420	6.95	0.96	5.24	0.30
90	-		4.36	0.14
185	8.95	2.6	4.17	0.12
400	12.3	9.5	-	

The results indicate that surface diffusivity, D_s , increases exponentially with the potential in 0.1 M HClO_4 . However, opposite effect of potential on D_s is observed in 0.5 M H_2SO_4 .

The difference in behavior of D_s with the potential value in two electrolytes can be understood in terms of adsorbability of the species in the electrolyte to the electrode surface. According to Somorjai⁷⁶, electrode surfaces undergo restructuring as a result of adsorption in the electrolyte of the species to the electrode surface, which results in an outward relaxation of surface atoms, causing enhanced or decreased mobility of them. This modification in the mobility of surface atoms then should be reflected in the values of the surface diffusion coefficients of the surface atoms on the surface (Au in our case).

In the case of HClO_4 , the interaction of ClO_4^- ions with the species, participating in the surface diffusion process, results in a decrease in the strength of the interactions of surface atoms with metal atoms in the bulk (outward relaxation of surface metal atoms). Such a process implies an increase in the surface diffusion coefficient thereby increase in coarsening kinetics of our porous structures. From the above results, we can conclude that the perchlorate (ClO_4^-) ions have the effect of increasing the mobility of gold adatoms over that of the bisulfate ions (SO_4^{2-}). Same behavior was found for Pt system in a study performed by Pugh⁷⁷.

The higher the applied coarsening potential be, the higher the strength of the interaction with surface atoms hence the higher the surface diffusivity until the formation of the Au oxide coverage. This behavior can clearly be seen in surface diffusivities determined in HClO_4 electrolyte. The maximum diffusivity was found at $400 \text{ mV}_{\text{MSE}}$.

CHAPTER 7 SUMMARY AND CONCLUSIONS

The critical overpotential for dealloying is highly sensitive to the presence of halides in the electrolyte for the Ag-Au system. The reduction of the critical potential observed for the halide containing electrolytes was not simply due to the decreasing equilibrium potential for Ag dissolution in the halide electrolytes. For example, the equilibrium potential for Ag in 0.1 M HClO₄ + 0.1 M KI is -0.077 V NHE which represents a reduction of 0.522 V from that of Ag in 0.1 M HClO₄ electrolyte. However, the respective critical potentials measured for the Au_{0.35}Au_{0.65} alloy in the same electrolytes is 0.558 V NHE (halide) and 1.309 V NHE (no halide) which represents a reduction in the critical potential of 0.751 V. These results are best represented in polarization data of current density versus overpotential.

The addition of halides also greatly influences the size scale of the resultant porosity produced during the dealloying process. We found that the porosity in the iodide containing electrolyte was 9 times larger than that observed in the absence of halides (67 nm compared to 7.8 nm). We expect the porosity created immediately after the dealloying process to be of order 2 nm and therefore all the porosity observed in this investigation after 5 hours of dealloying represents a highly coarsened structure. Using a simple surface diffusion coarsening model, we calculated the surface diffusivity in the various electrolytes as $2 \times 10^{-16} \text{ cm}^2 \text{ sec}^{-1}$ (0.1 M HClO₄), $3 \times 10^{-15} \text{ cm}^2 \text{ sec}^{-1}$ (KBr or KCl) and $8 \times 10^{-13} \text{ cm}^2 \text{ sec}^{-1}$ (KI). These values are consistent with those in the literature^{64,66}.

Based on the model proposed Sieradzki et al.³⁰, a reduction in overpotential is expected when the ratio of the surface diffusivity of the more noble element to the exchange current density of the more active element, D_s/J_o , decreases. Based on our results, this would mean that the exchange current density must be increasing at a much faster rate than the increasing surface diffusivity. Using the measured critical potential and the calculated value of diffusivity, we estimated an exchange current density of $3.2 \times 10^{-7} \text{ mA cm}^{-2}$ for Ag dissolution in 0.1 M HClO₄. In order to validate this number

Electrochemical Impedance Spectroscopy (EIS) studies, which can provide fundamental information on reaction kinetics, has been performed on pure Ag electrode. The idea was to determine from the impedance plots the charge transfer resistance (R_{CT}), which is inversely proportional to the rate of reaction. However, some problems have been encountered due to the nature of our electrolyte used in the present study. Since the electrolyte did not contain pre-dissolved Ag^+ ions, we obtained impedance plots which were not repeatable and different from one experiment to another. Next step would be to perform EIS measurements to determine the exchange current density in ion containing electrolytes and extrapolate it to a Ag ion concentration of 10^{-6} (approximating our electrolytes).

Detailed electrochemical study has been presented aimed at examining the behavior of AgAu alloys at potentials below the critical potential. A more accurate method has been proposed for the determination of the critical potential in binary alloys. The method includes performing a series of potential hold experiments in the vicinity of the critical potential in order to accurately determine the transition from a purely current decay to a steady state current behavior. Alloys held at or above the critical potential display a constant dealloying current while alloys held below the critical potential display rapidly decaying currents. This transition is approximately 150 mV less than that measured based on anodic polarization curves. Interesting enough, Monte Carlo simulation of dealloying process developed by Erlebacher et.al⁷⁴ revealed critical potentials quite close to our experimental results. In the light of these results, one may need to reinterpret the results of slow strain rate tests which find stress corrosion cracking below the conventionally measured value of E_c ⁷⁸.

The method also eliminates the ambiguities in defining the critical potential based on anodic polarization curves that arise owing to the sensitivity of alloy polarization data on scan rate. The existence of three-dimensional bi-continuous porosity and its expected brittle nature was also confirmed by field emission scanning electron microscopy.

The potential hold experiments demonstrated the presence of a potential dependent region below the conventionally defined critical potential as opposed to the literature. The comparison of the polarization curve and the one obtained from the steady state current studies revealed a constant cut-off current value ($0.6 \mu\text{A cm}^{-2}$) corresponding to the “true” critical potential below which dealloying does not occur. This value is much lower than that is reported in the literature.

The electrochemical current-time transients yield a current decay with a slope between -0.75 and -1.0. The observed data can not be explained with the existing models based on volume diffusion and solid state diffusion model of Pickering and Wagner⁴⁰. Although the measured decay rate seems to be in agreement with the experimental results of Laurent and Landolt⁶⁹ further studies needs to be done in order to satisfactorily simulate the present experimental data.

The coarsening of dealloyed structures is surface diffusion dominated i.e. displays $t^{0.25}$ kinetics at long times. This is in agreement with the literature for the relaxation of the roughened gold surfaces. Using a similar analysis along with the Small Angle Neutron Scattering measurements, surface diffusivities of Au has been calculated in different media and at different potential values.

The effect of dealloying potential on the surface diffusivity of Au adatoms has been explored for two different AgAu alloy system. For both systems, surface diffusivity of gold was found to decrease with potential to a value as low as $10^{-19} \text{ cm}^2 \text{ sec}^{-1}$. This low diffusivity correlated with “freezing” of the porosity at elevated potentials is attributed to Au oxidation which prevents adsorption of ions from the electrolyte to the gold adatoms.

Pre-dealloyed porous AgAu structures coarsened in 0.1 M HClO₄ increased the surface diffusivity of Au over those coarsened in 0.5 M H₂SO₄. Same behavior was found for the Pt system in a study performed by Pugh⁷⁷. The author attributed this to the presence of possible chloride contamination of the electrolyte. We believe that this is due to the difference in adsorbability of the species in the electrolyte.

The surface diffusivity of Au adatoms in 0.5 M H₂SO₄ was found to be 10⁻¹⁶ cm² sec⁻¹. This value is however two orders of magnitude lower than the one reported in [64]. Our values seem to be more reasonable when we compare these results with the one obtained at elevated temperatures. Our preliminary results indicate that the D_s for Au at 250 C is 10⁻¹⁴ cm² sec⁻¹ which is on the same order of magnitude reported in the literature.

REFERENCES

1. R.W. Ertenberg, B. Andraka, Y. Takano, *Physica B*, 284-288, 2022-2023 (2000)
2. Jongsoo Yoon and Moses H.W. Chan, *Physical Review Letters*, 78(25), 4801-, (1997)
3. Gabor A.Csathy, Darly Tulimieri, Jongsoo Yoon, *Physical Review Letters*, 80(20), 4482-4485 (1998)
4. K.Sieradzki and R.C. Newman, "Brittle Behavior of Ductile Metals during Stress-Corrosion Cracking," *Philosophical Magazine A* 51 (1), 95-132 (1985).
5. R. C. Newman, R. R. Corderman, and K. Sieradzki, "Evidence for Dealloying of Austenitic Stainless Steels in Simulated Stress Corrosion Crack Environments," *British Corrosion Journal* 24 (2), 143-148 (1989).
6. D. E. Williams, R. C. Newman, Q. Song, and R. G. Kelly, "Passivity Breakdown and Pitting Corrosion of Binary-Alloys," *Nature* 350 (6315), 216-219 (1991).
7. Howard W. Pickering and Y. S. Kim, *Corrosion Science* 23, 1107 (1983).
8. J. S. Chen, M. Salmeron, and T. M. Devine, *Corrosion Science* 34, 2071 (1993).
9. T. B. Cassagne, W. F. Flanagan, and B. D. Lichter, "On the Failure Mechanism of Chemically Embrittled Cu₃Au Single Crystals," *Metallurgical Transactions A* 17A, 703-710 (1986).
10. H. Moore, S. Beckinsale, and Clarice E. Mallinson, "The Season-Cracking of Brass and Other Copper Alloys," *Journal of the Institute of Metals* 25, 35-153 (1921).
11. M.B. Vukmirovic, N. Dimitrov, K. Sieradzki, "Dealloying and Corrosion of Al Alloy 2024-T3", *JECS*, 149(9) B248-B439 (2002)

-
12. N. Dimitrov, J. A. Mann, M. Vukmirovic, and Karl Sieradzki, "Dealloying of Al₂CuMg in Alkaline Media," *Journal of the Electrochemical Society* 147 (9), 3283-3285 (2000).
 13. R. G. Buchheit, R. P. Grant, P. F. Hlava, B. McKenzie, and G. L. Zender, "Local dissolution phenomena associated with S phase (Al₂/CuMg) particles in aluminum alloy 2024-T3," *Journal of the Electrochemical Society* 144 (8), 2621-8 (1997).
 14. A. D. Tomsett, H. E. Curry-Hyde, M. S. Wainwright, D. J. Young and A. J. Bridgewater. Structural Changes During the Leaching of Copper-Based Raney Catalysts. *Applied Catalysis* 33, 119-127 (1987).
 15. A. J. Smith, T. Tran and M. S. Wainwright. Kinetics and Mechanism of the Preparation of Raney Copper. *Journal of Applied Electrochemistry* 29, 1085-1094 (1999).
 16. A. J. Forty and P. Durkin. A Micromorphological Study of the Dissolution of Silver - Gold Alloys in Nitric Acid. *Phil. Mag. A* 42, 295 (1980).
 17. S. G. Corcoran, K. Sieradzki and D. Wiesler. An In Situ Small Angle Neutron Scattering Investigation of Ag_{0.7}Au_{0.3} Dealloying. *Materials Research Society Symposium Proceedings* 376, 377 (1994).
 18. S. G. Corcoran, D. G. Wiesler and K. Sieradzki. An In Situ Small Angle Neutron Scattering Investigation of Ag_{0.7}Au_{0.3} Dealloying Under Potential Control. *Materials Research Society Symposium Proceedings* 451, 93-98 (1997).
 19. S. G. Corcoran. "The Morphology of Alloy Corrosion" in *Proceedings of the Symposium on Critical Factors in Localized Corrosion III* (eds. K. R. G., G. S. Frankel, P. M. Natishan and R. C. Newman) 500-507 (The Electrochemical Society, Pennington, NJ, 1999).
 20. K. Sieradzki and R.C. Newman, *J. Phys. Chem. Solids* 48, 1101 (1987)

-
21. R.P. Tischer and H. Gerischer, *Zeitschrift für Electrochemie Berichte Der Bunsengesellschaft für Physikalische Chemie*(in German), 62, 50 (1958)
 22. Corcoran G. Sean, "The Morphology of Alloy Corrosion"
 23. M.J.Pryor and J.C. Fister, *JECS*, 131, 1230-1235 (1984)
 24. H.W. Pickering. In *Fundamental Aspects of Stress Corrosion Cracking*(eds.R.W. Staehle, A.J. Forty and D. Van Rooyen) 159-177 (NACE, Ohio State Univ.,1967)
 25. B. Kabius, H. Kaiser and H. Kaesche. In *Surfaces, Inhibition, and Passivation: Proceedings of an international symposium honoring Doctor Norman Heckerman on his seventy-fifth birthday* 562-573 (Electrochemical Society,1986)
 26. B.G.Ateya, J.D. Fritz and H.W. Pickering, *JECS*, 144, 2606-2613 (1997)
 27. J.I. Gardiazabal and J.R. Galvele, *JECS*, 127, 255-258 (1980)
 28. R.Li and K. Sieradzki, *Physical Review Letters*, 68, 1168-1171 (1992)
 29. R.G.Kelly, A.J. Young and R.C. Newman, *The Characterization of the Coarsening of Dealloyed Layers by EIS and Its Correlation with Stress-Corrosion Cracking*. In *Electrochemical Impedance: Analysis and Interpretation*, ASTM STP 1188(eds.J.R.Scully,D.C.Silverman and M.W.Kendig)94-112(American Society for Testing and Materials Philadelphia,1993)
 30. K. Sieradzki, *JECS*, 140(10), 2868-2872 (1993)
 31. G.Z. Chen, D.J. Fray and T.W. Farthing, *Nature* 407, (2000)
 32. D.J. Fray, *Materials Research Society Bulletin*, 25, 11-12 (2000)
 33. A.J.Forty, *Gold Bull.*, 14, 25 (1981)
 34. H.W.Pickering and P.J. Byrne, *JECS*, 118, 209 (1971)

-
35. M.J.Pryor and Kar-Kheng Giam., JECS, 129, 2157 (1982)
 36. H.W.Pickering, "Characteristic Features of Alloy Polarization Curves", Corrosion Science, 23, 1107-1120 (1983)
 37. R.C.Newman, S.G. Corcoran, J. Erlebacher, M.J. Aziz, and K. Sieradzki, MRS Bulletin, July, 24- (1999)
 38. Ralph B. Abrams, Transactions of the American Chemical Society, 42, 39-55 (1922)
 39. G.D.Bengough, R.M. Jones, and Ruth Pirre, "Fifth Report to the Corrosion Committee of the Institute of Metals," J.Inst.Metals, 23, 65-158 (1920)
 40. H.W.Pickering and C. Wagner, JECS, 114(7), 698-706 (1967)
 41. C.Wagner, JECS, 101, 225 (1954)
 42. H.Gerisher Korrosion XIV Korrosionsschutz durch Lagieren, Verlag Chemie, Weinheim, (1962)
 43. Harrison and Wagner, Acta Metall., 7, 722 (1959)
 44. A.J.Forty and G. Rowlands, Philosophical Magazine A, 43(1), 171-188 (1981)
 45. A. Dursun, D.V. Pugh and S.G. Corcoran, JECS, accepted for publication (2002)
 46. K.Sieradzki, J.S. Kim, J.S. Cole et.al., JECS, 134, 1635, (1987)
 47. Dietrich Stauffer and Amnon Harmony, Introduction to Percolation Theory, 2nd ed. (Taylor and Francis, London, 1991).
 48. W.W. Mullins, Metal Surfaces: Structure, Energetics and Kinetics, (Am.Soc. of Metals, Metal Park, Ohio, 1963) p.17.

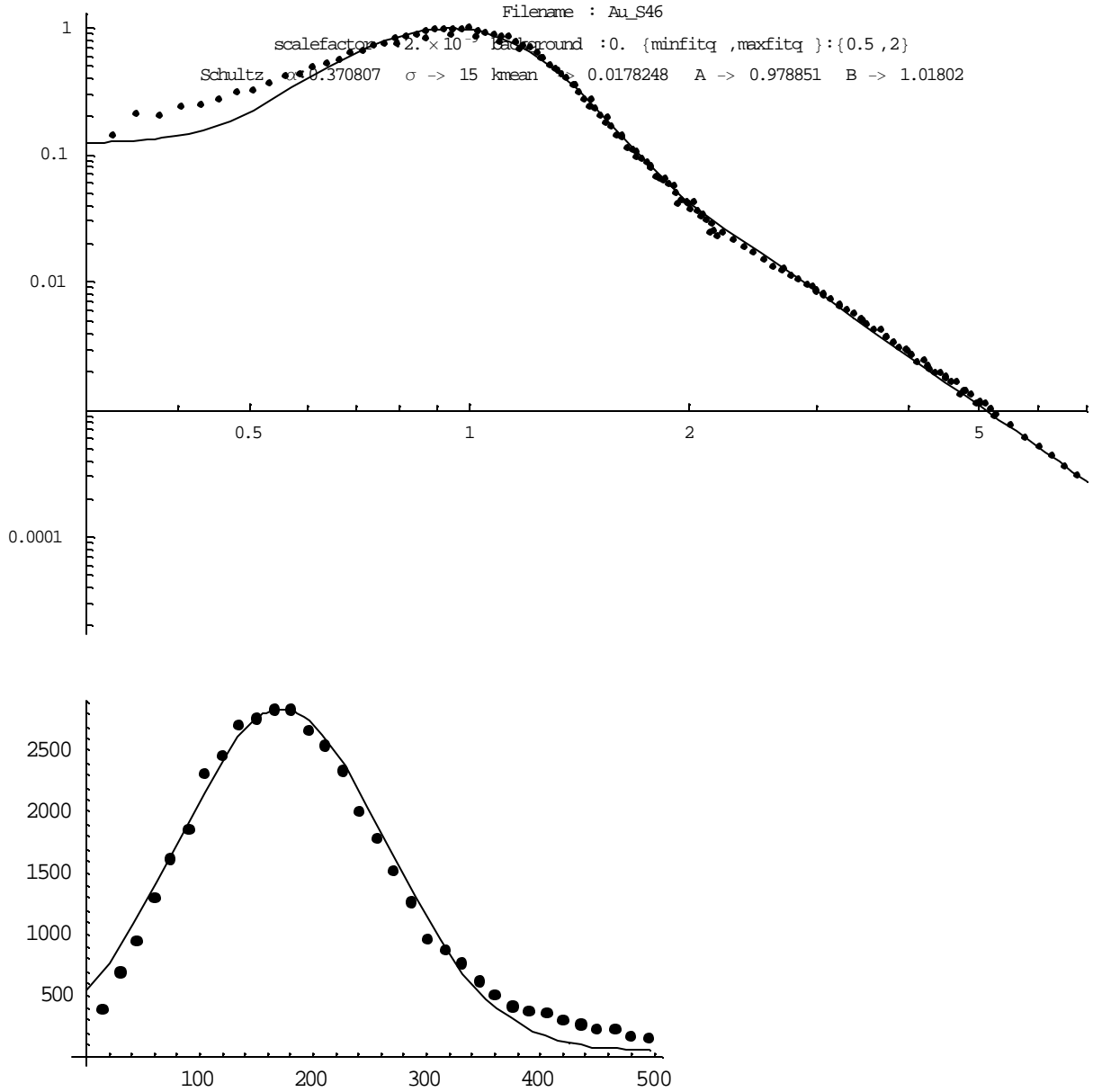
-
49. K.Sieradzki, R.R. Corderman, K. Shukla and R.C. Newman, *Phil. Mag. A*, **59**, 713 (1989)
50. J. Erlebacher and et.al., “ Evolution of Nanoporosity in Dealloying”, *Nature* **410**, 450-3 (2001)
51. B.W. Parks, Jr., J.D. Fritz, and H.W. Pickering, *Scripta Metall.*, **23**, 951, (1989)
52. K.Sieradzki and et.al., “The De-alloying Critical Potential”, *JECS*, **149**(8), B370-B377 (2002)
53. S.G. Corcoran, David Wiesler, John Barker, K. Sieradzki, *Mat.Res.Soc.Symp.Proc.*, **376**, 377-382 (1995)
54. M. Teubner and R. Strey, *American Institute of Physics* **5**, 3195-3200 (1987)
55. J.W. Cahn, *J. Chem. Phys.*, **42**, 93 (1965)
56. N.F. Berk, *Physical Review Letters*, **58** (25) 2718- (1987)
57. N.F. Berk, *Physical Review Letters A*, **44** (8), 5069- (1991)
58. S.H. Chen, S.L. Chang and R. Strey, *Progress in Colloid&Polymer Science*, **81**, 30-35 (1990)
59. S.H.Chen and S.L. Chang, *Journal of Applied Crystallography*, **24**, 721-731 (1991)
60. J.R.Galvele, I.A. Maier and S.A. Fernandez *Corrosion Science* **52** 326-330 1996
61. H.P. Bonzel, *Surface Physics of Materials* (edited by J. Burke, N. Reed and W. Weiss), p.271. Syracuse University Press, New York (1967)
62. J. Gonzalez-Velasco. A Theoretical Explanation of the Surface Diffusion Mechanism in Metal Electrodes in Contact with Electrolytes. *Surface Science* **410**, 283-289 (1998).

-
63. G.Andreasen, M. Nazzarro, J. Ramirez, R. C. Salvarezza and A. J. Arvia. Kinetics of Particle Coarsening at Gold Electrode/Electrolyte Solution Interfaces Followed by In Situ Scanning Tunneling Microscopy. *Journal of the Electrochemical Society* 143, 466-471 (1996).
64. J. M. Dona and J. Gonzalez-Velasco. Mechanism of Surface Diffusion on Gold Adatoms in Contact with an Electrolytic Solution. *Journal of Physical Chemistry* 97, 4714-4719 (1993).
65. M. P. Garcia, M. M. Gomez, R. C. Salvarezza and A. J. Arvia. Effect of the Solution Composition and the Applied Potential on the Kinetics of Roughness Relaxation at Gold Electrodes in Slightly Acid Electrolytes. *Journal of Electroanalytical Chemistry* 347, 237-246 (1993).
66. C. Alonso, R. C. Salvarezza, J. M. Vara and A. J. Arvia. The Surface Diffusion of Gold Atoms on Gold Electrodes in Acid Solution and its Dependence on the Presence of Foreign Adsorbates. *Electrochimica Acta* 35, 1331-1336 (1990).
67. J. Gniewek, J. Pezy and J. O'M. Bockris, *J. electrochem.Soc.* 125, 17 (1978)
68. K. Wagner, S. R. Brankovic, N. Dimitrov, and Karl Sieradzki, "Dealloying Below the Critical Potential," *Journal of the Electrochemical Society* 144 (10), 3545-3555 (1997).
69. J. Laurent and D. Landolt, *Electrochim. Acta*, 36, 49(1991).
70. B.G. Ateya and H.W. Pickering, *Corros.Sci.*, 38, 1245 (1996)
71. A.I. Marshakov, A.P. Pchel'nikov and V.V. Losev, *Elektrokhimiya* 21, 949 (1985)
72. J.D.Fritz and H.W.Pickering, *JECS*, 138, 3209 (1991)
73. T.P.Moffat, F.-R.F.Fan, and A.J.Bard, *JECS*, 138, 3224 (1991)

-
74. Jonah Erlebacher, "An Atomistic Description of Dealloying: Porosity Evolution, the Nature of the Critical Potential, and Rate Limiting Behavior" in preparation
75. R.P. Tischer and H. Gerischer, *Z. Elektrochem*, 62, 50, (1962)
76. G.S. Somorjai, *J. Phys. Chem.* 94 (1990) 1013-.
77. Pugh V. Dylan, Ph.D Thesis, Virginia Polytechnic Inst.& State University (2003)
78. G.S. Duffo and J.R. Galvele. " Stress Corrosion Cracking of Ag-20Au in HClO₄, AgClO₄,and KCl Solutions by Surface Mobility. *Metallurgical Transactions A* 24A, 425-433 (1993)

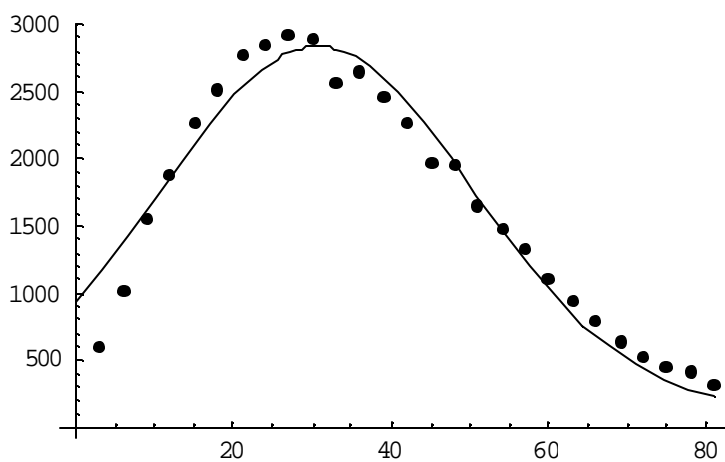
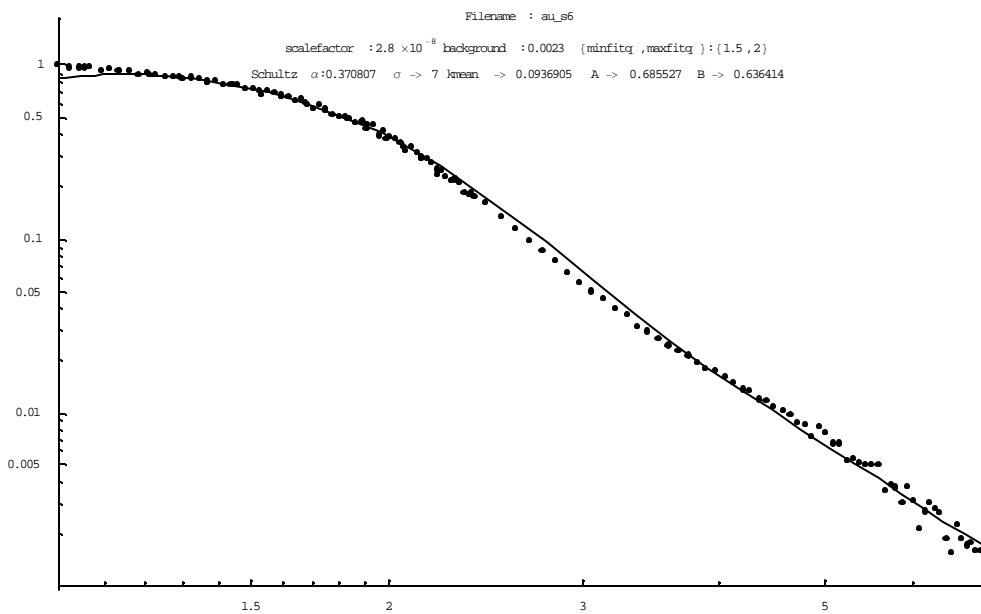
APPENDIX A

SANS DATA FITTED TO LEVELED-WAVE METHOD OF BERK.



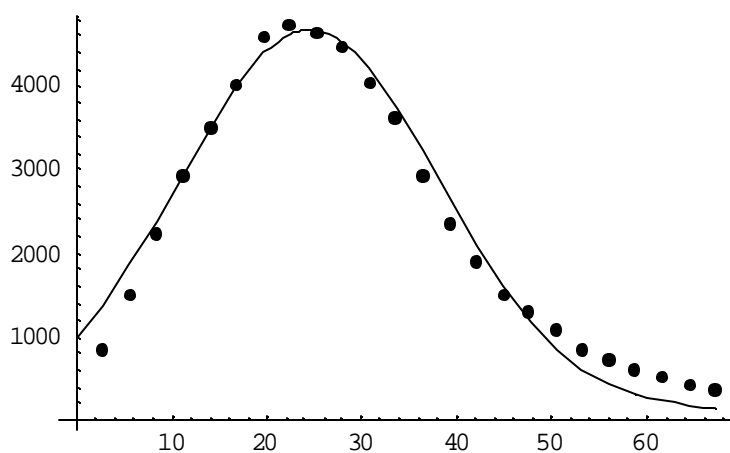
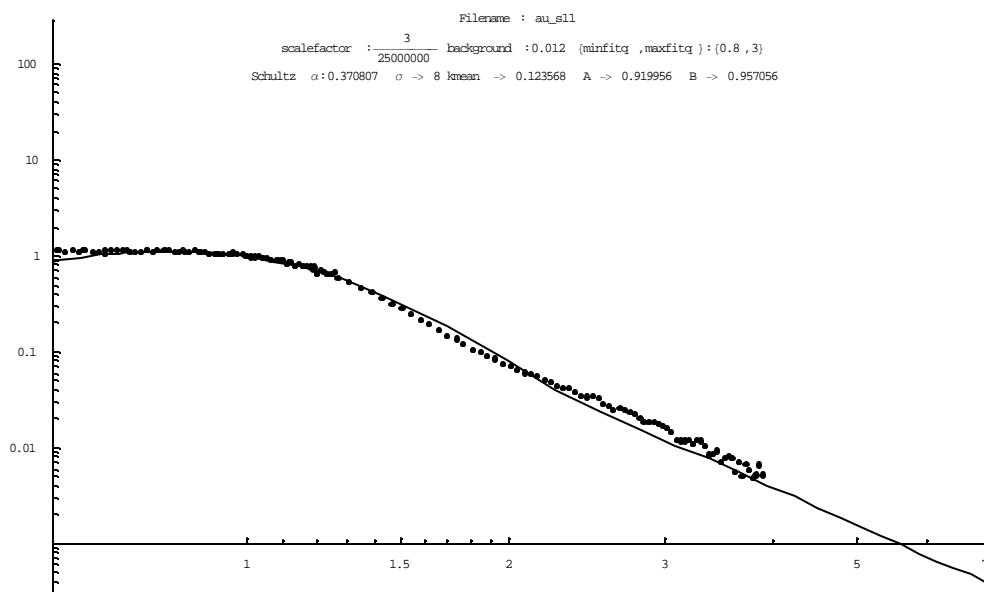
Ligament width = 17.2 nm

Figure A. 1 Ex-situ SANS data and the fit to that data for porous $\text{Ag}_{0.70}\text{Au}_{0.30}$. Ligament width was determined by Gaussian fit to ligament data (second curve). The sample was dealloyed at 550 mV_{MSE} for 24 hours in 0.1 M HClO_4 .



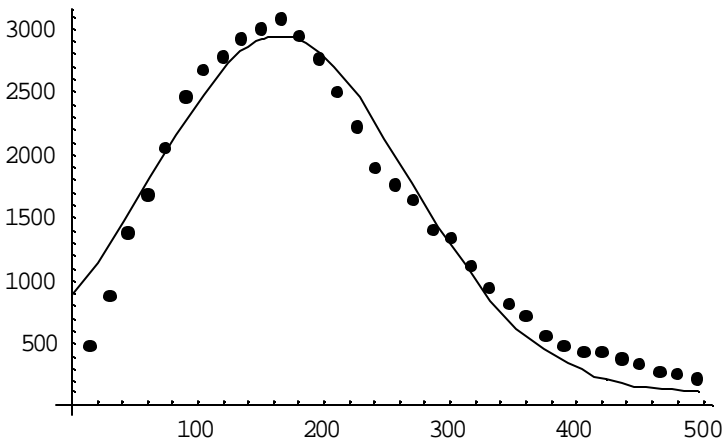
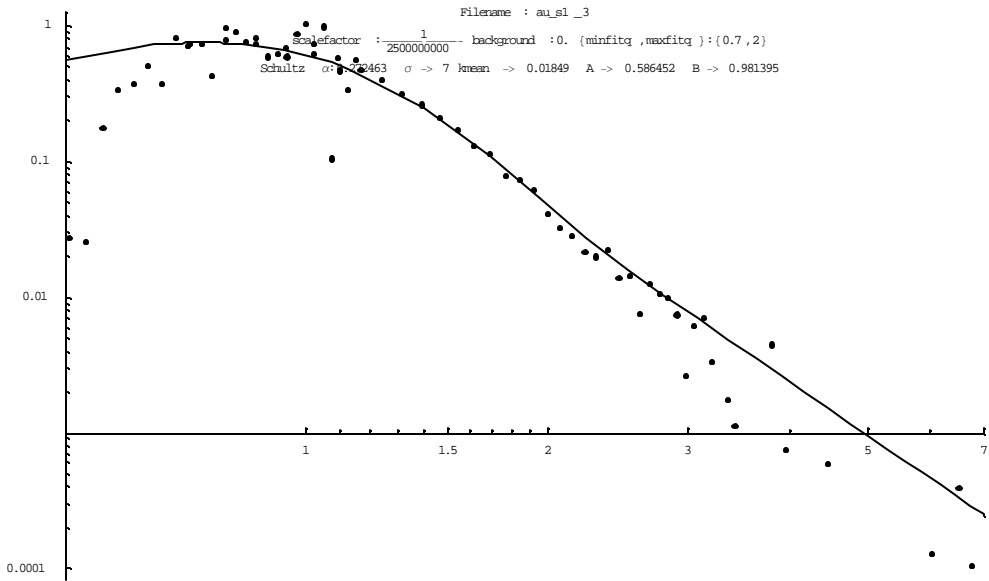
Ligament width = 2.8 nm

Figure A. 2 Ex-situ SANS data and the fit to that data for porous $\text{Ag}_{0.70}\text{Au}_{0.30}$. Ligament width was determined by Gaussian fit to ligament data (second curve). The sample was dealloyed at 655 mV_{MSE} for 3 hours in 0.1 M HClO_4 .



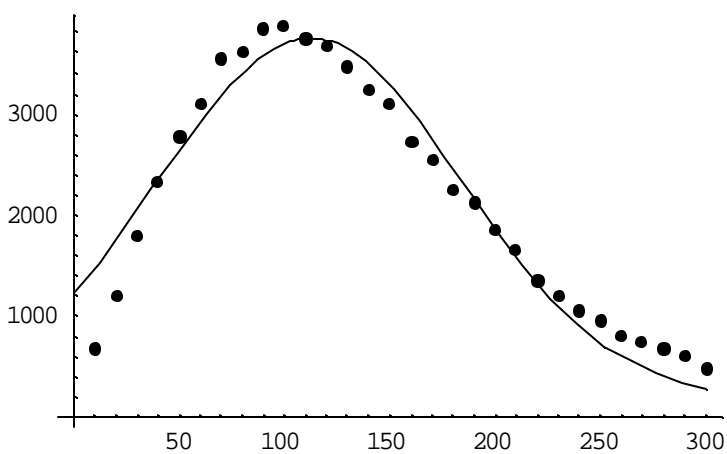
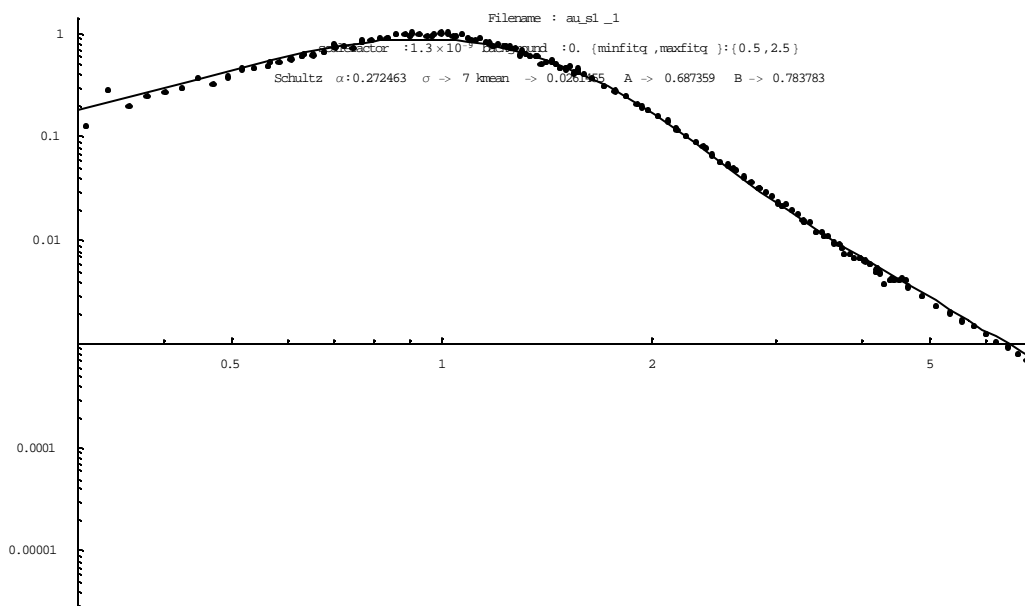
Ligament width = 2.3 nm

Figure A. 3 Ex-situ SANS data and the fit to that data for porous $\text{Ag}_{0.70}\text{Au}_{0.30}$. Ligament width was determined by Gaussian fit to ligament data (second curve). The sample was dealloyed at $750 \text{ mV}_{\text{MSE}}$ for 2 hours in 0.1 M HClO_4 .



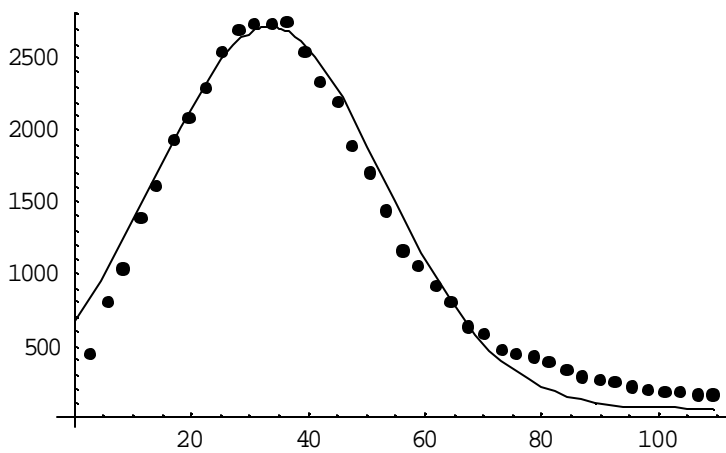
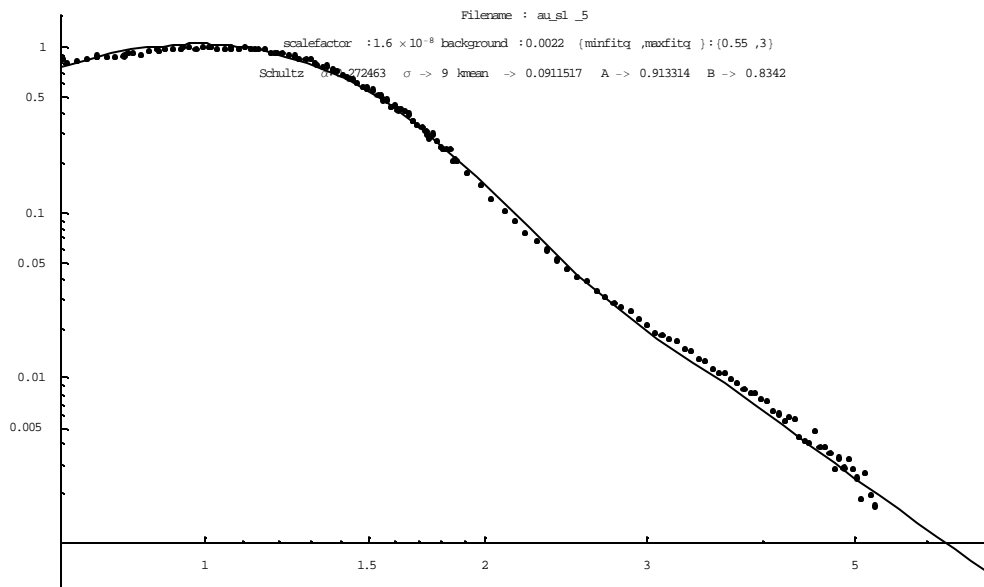
Ligament width = 16.3 nm

Figure A. 4 Ex-situ SANS data and the fit to that data for porous $\text{Ag}_{0.65}\text{Au}_{0.35}$. Ligament width was determined by Gaussian fit to ligament data (second curve). The sample was dealloyed at 450 mV_{MSE} for 32.5 hours in 0.1 M HClO₄.



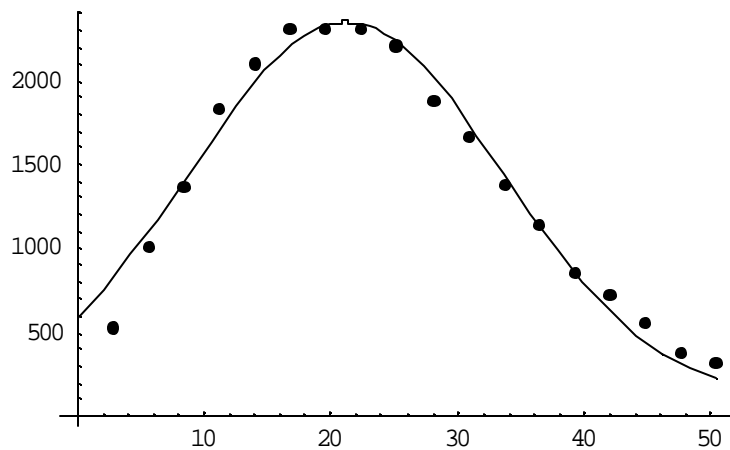
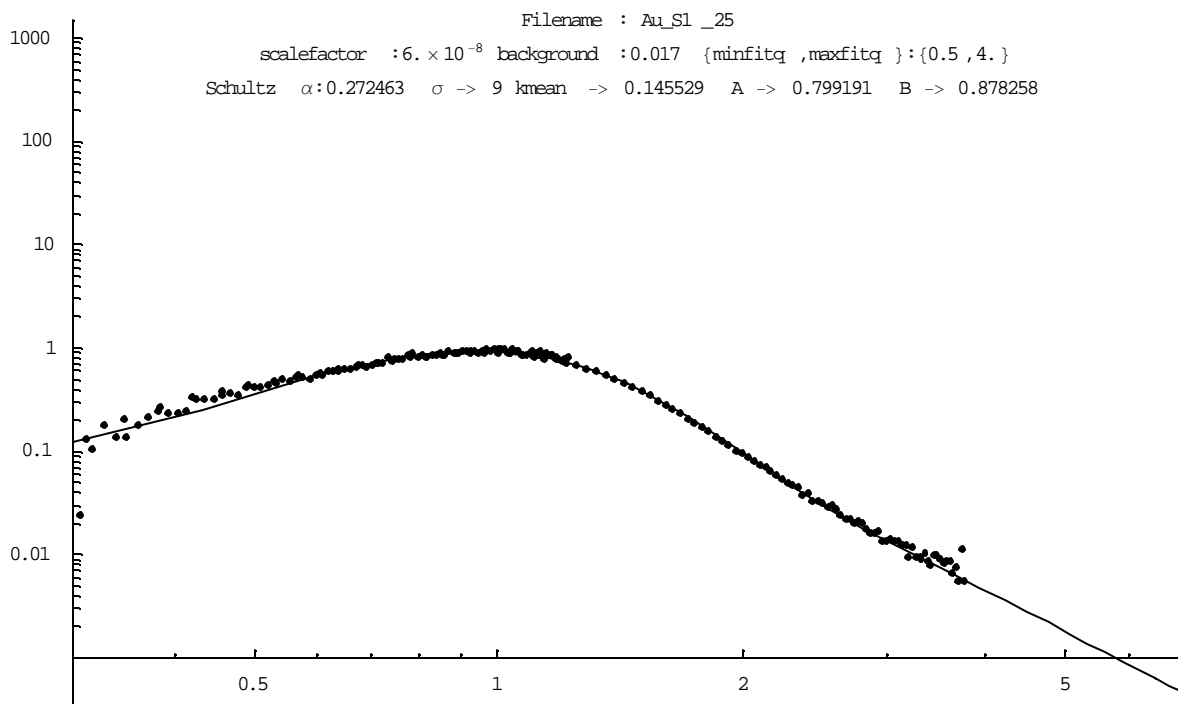
Ligament width = 9.5 nm

Figure A. 5 Ex-situ SANS data and the fit to that data for porous $\text{Ag}_{0.65}\text{Au}_{0.35}$. Ligament width was determined by Gaussian fit to ligament data (second curve). The sample was dealloyed at 600 mV_{MSE} for 32.5 hours in 0.1 M HClO_4 .



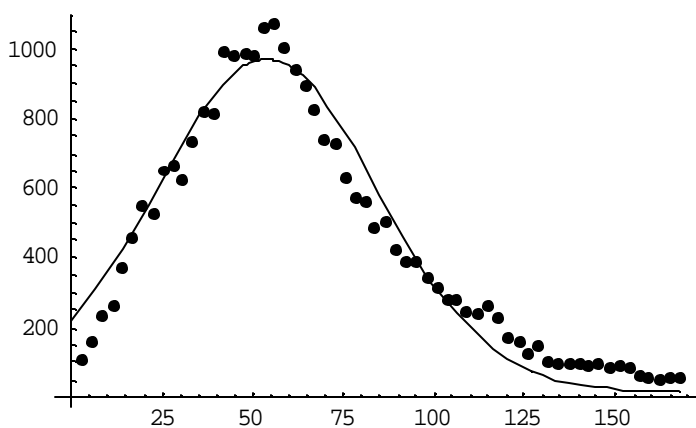
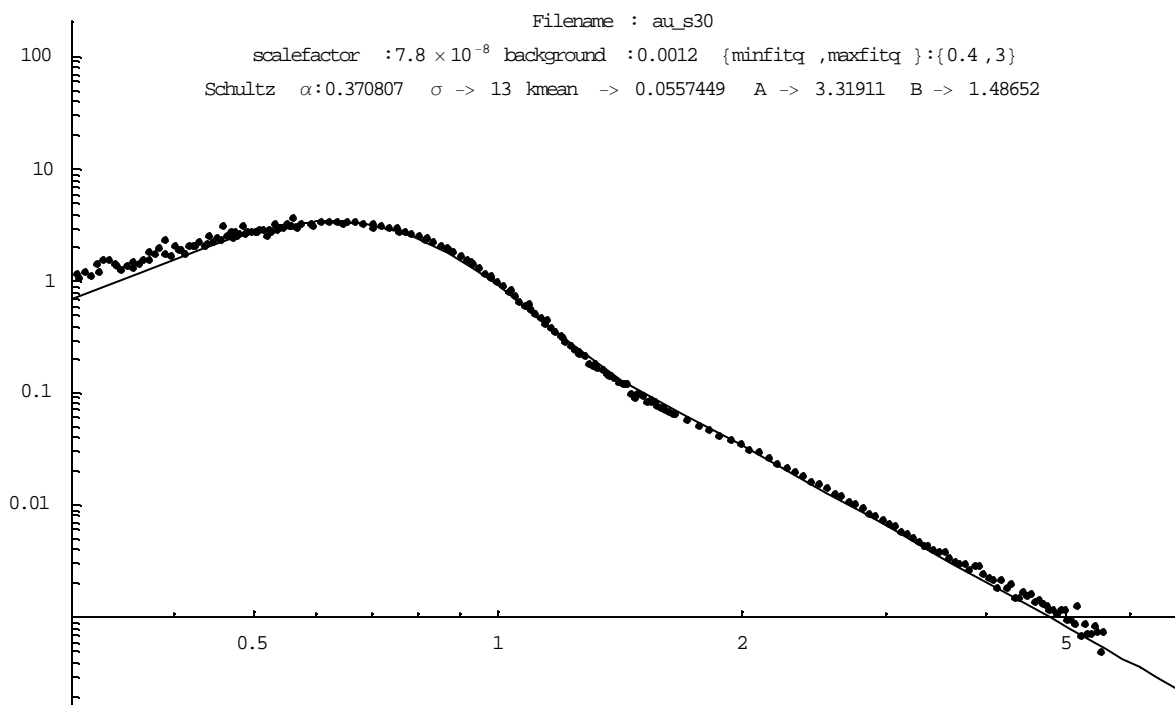
Ligament width = 3.3 nm

Figure A. 6 Ex-situ SANS data and the fit to that data for porous $\text{Ag}_{0.65}\text{Au}_{0.35}$. Ligament width was determined by Gaussian fit to ligament data (second curve). The sample was dealloyed at $655 \text{ mV}_{\text{MSE}}$ for 15 hours in 0.1 M HClO_4 .



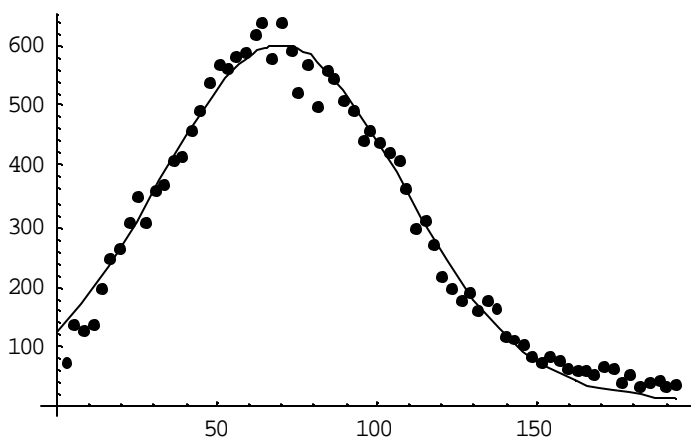
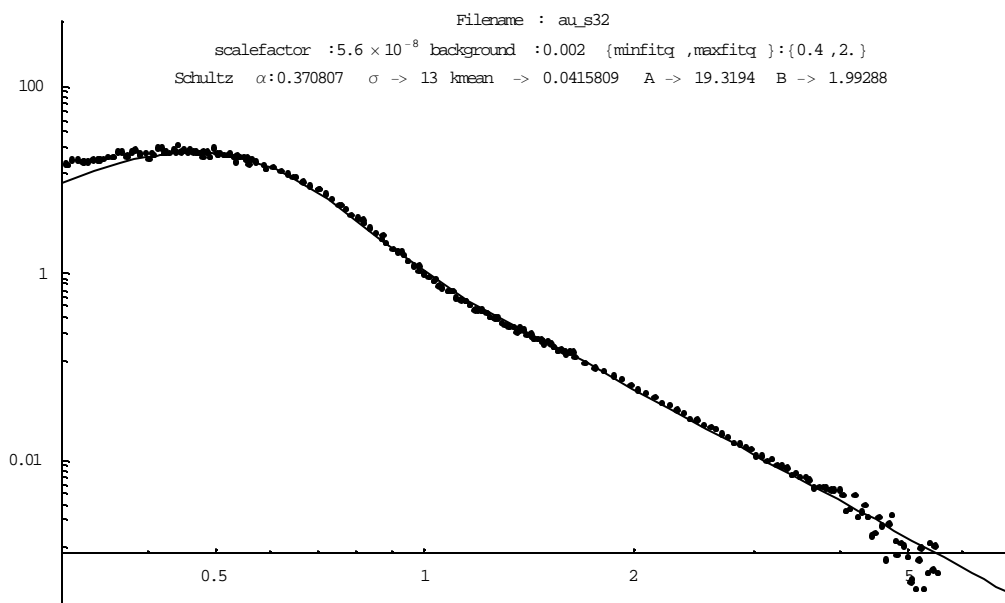
Ligament width = 1.7 nm

Figure A. 7 Ex-situ SANS data and the fit to that data for porous $\text{Ag}_{0.65}\text{Au}_{0.35}$. Ligament width was determined by Gaussian fit to ligament data (second curve). The sample was dealloyed at $800 \text{ mV}_{\text{MSE}}$ for 3 hours in 0.1 M HClO_4 .



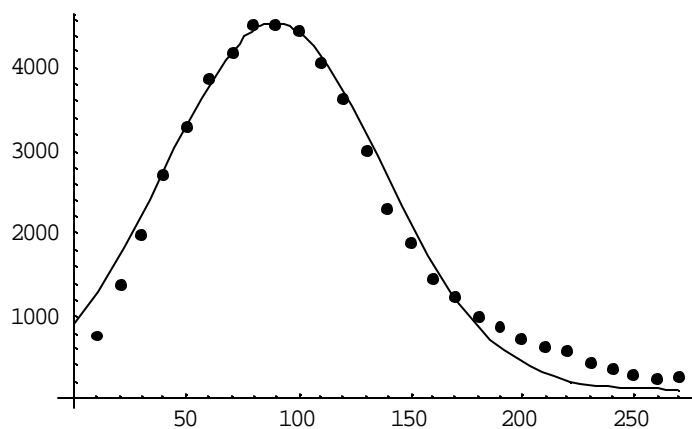
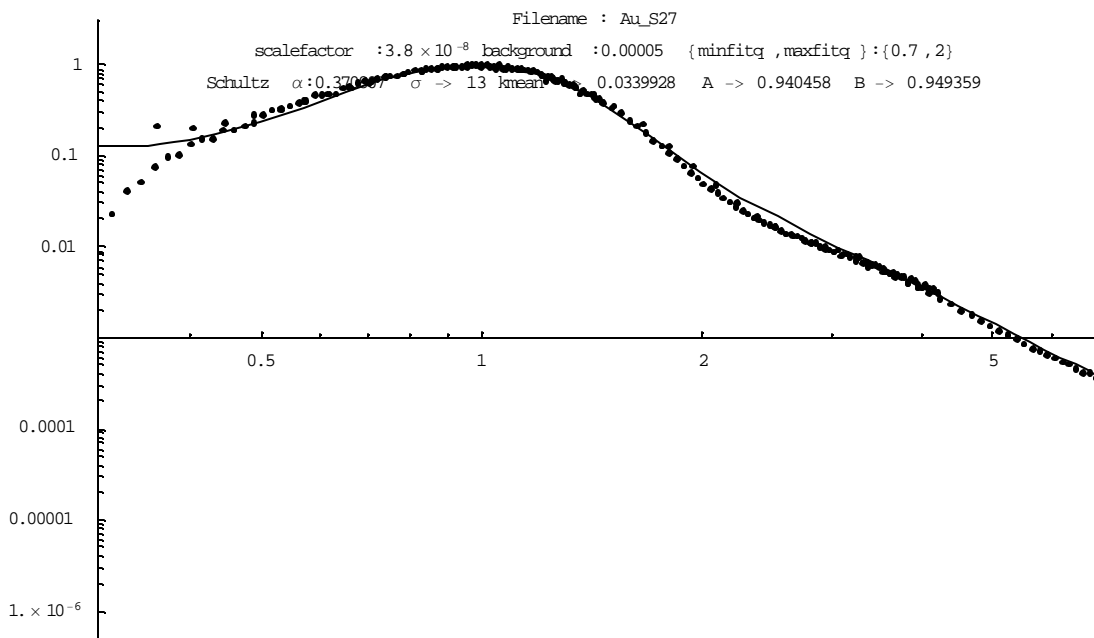
Ligament width = 5.4 nm

Figure A. 8 Ex-situ SANS data and the fit to that data for porous $\text{Ag}_{0.70}\text{Au}_{0.30}$. Ligament width was determined by Gaussian fit to ligament data (second curve). After the sample was dealloyed at $750 \text{ mV}_{\text{MSE}}$ for 1.5 hours in 0.1 M HClO_4 , it was subjected to a coarsening potential of $-600 \text{ mV}_{\text{MSE}}$ in 0.1 M HClO_4 .



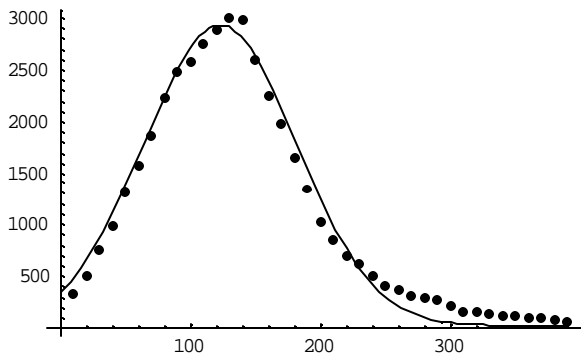
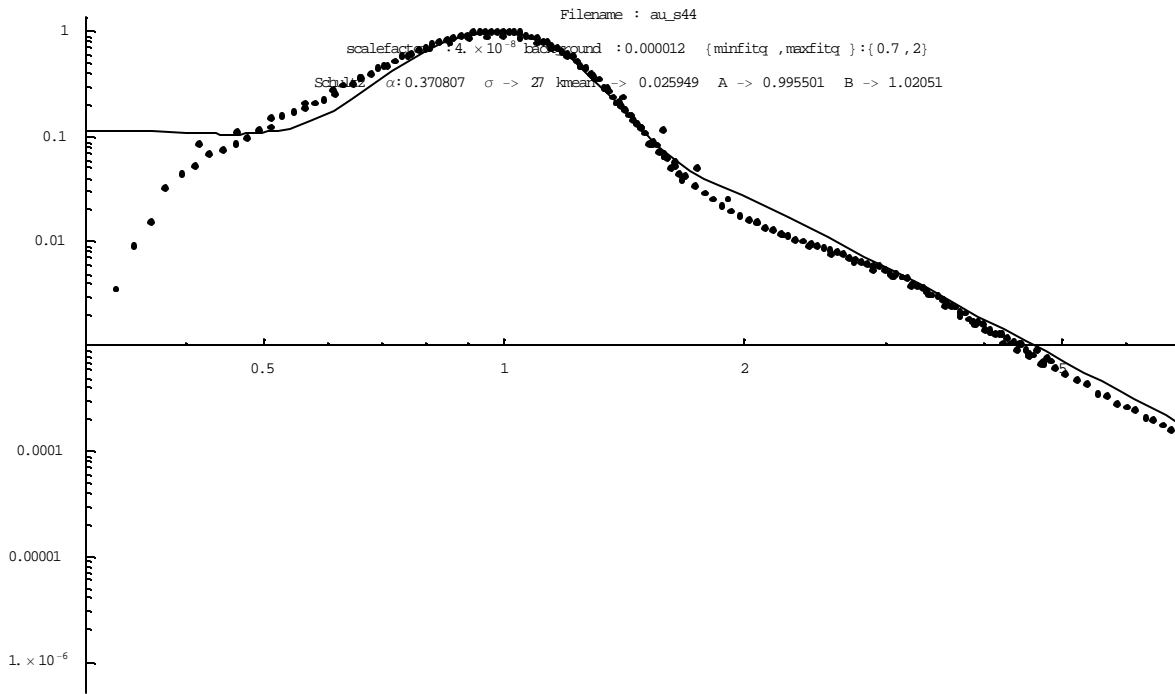
Ligament width = 6.95 nm

Figure A. 9 Ex-situ SANS data and the fit to that data for porous $\text{Ag}_{0.70}\text{Au}_{0.30}$. Ligament width was determined by Gaussian fit to ligament data (second curve). After the sample was dealloyed at 750 mV_{MSE} for 1.5 hours in 0.1 M HClO_4 , it was subjected to a coarsening potential of -420 mV_{MSE} in 0.1 M HClO_4 .



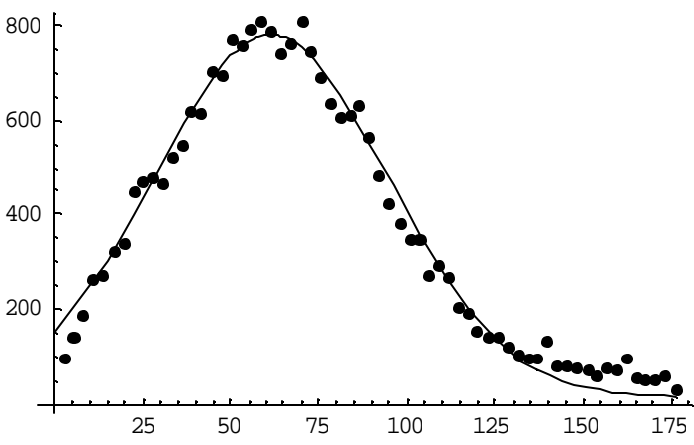
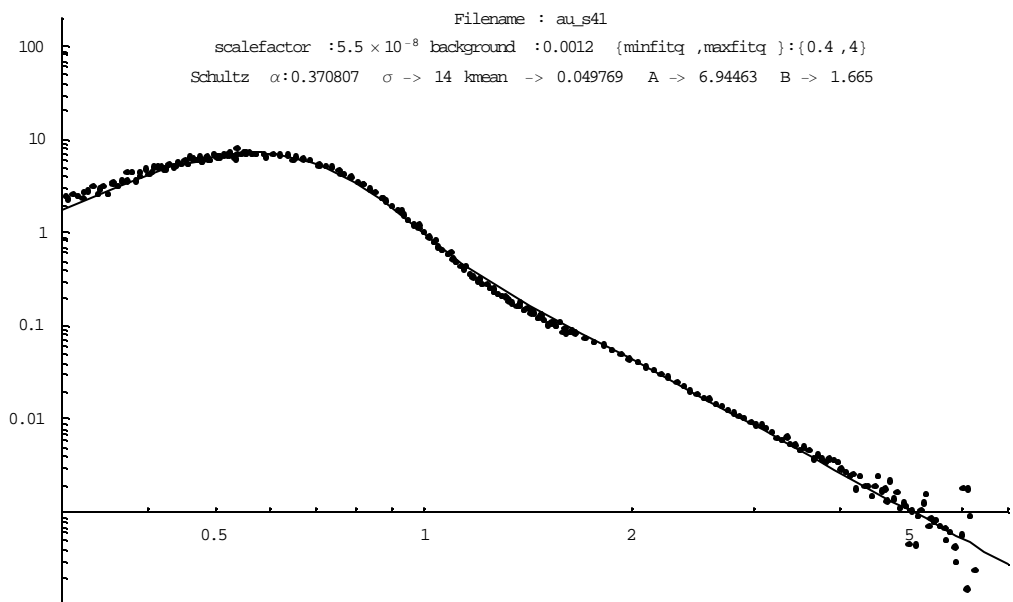
Ligament width = 8.95 nm

Figure A. 10 Ex-situ SANS data and the fit to that data for porous $\text{Ag}_{0.70}\text{Au}_{0.30}$. Ligament width was determined by Gaussian fit to ligament data (second curve). After the sample was dealloyed at 750 mV_{MSE} for 1.5 hours in 0.1 M HClO_4 , it was subjected to a coarsening potential of 185 mV_{MSE} in 0.1 M HClO_4 .



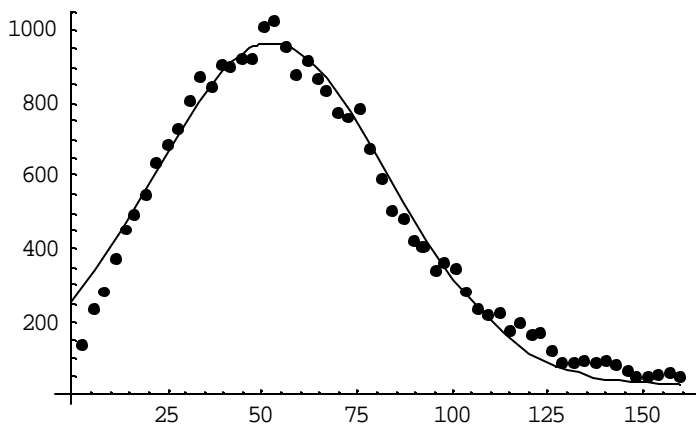
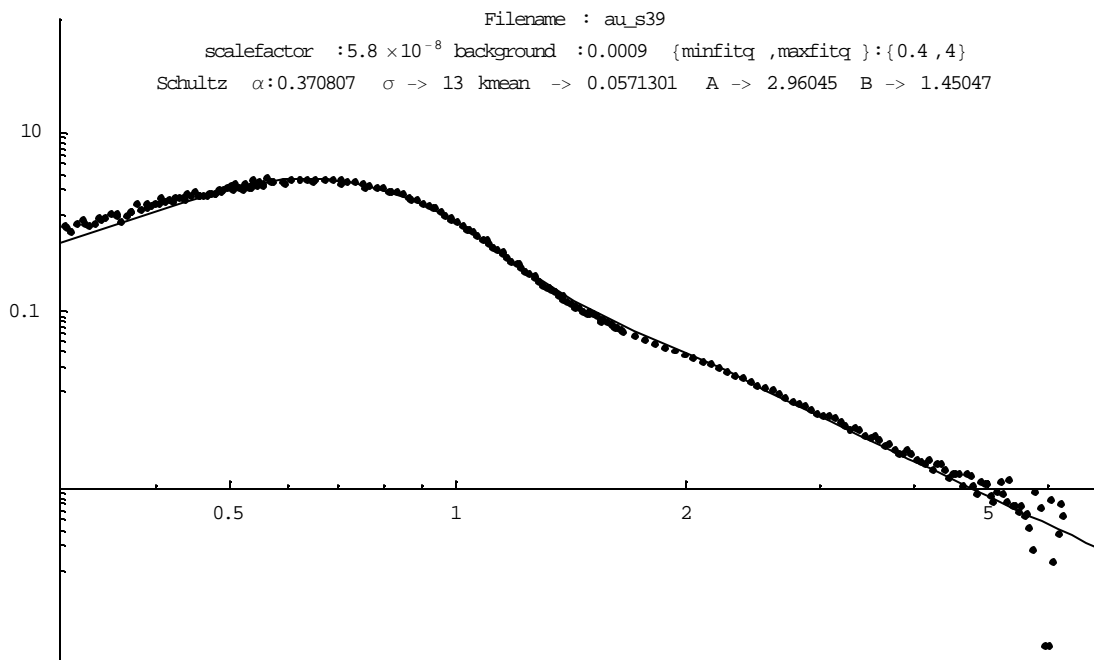
Ligament width = 12.3 nm

Figure A. 11 Ex-situ SANS data and the fit to that data for porous $\text{Ag}_{0.70}\text{Au}_{0.30}$. Ligament width was determined by Gaussian fit to ligament data (second curve). After the sample was dealloyed at $750 \text{ mV}_{\text{MSE}}$ for 1.5 hours in 0.1 M HClO_4 , it was subjected to a coarsening potential of $400 \text{ mV}_{\text{MSE}}$ in 0.1 M HClO_4 .



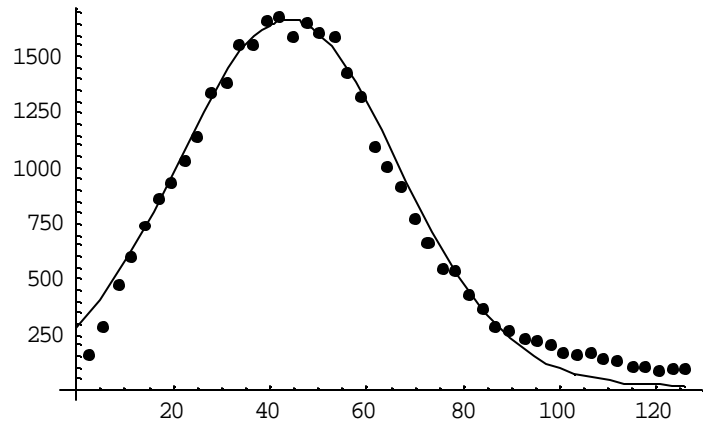
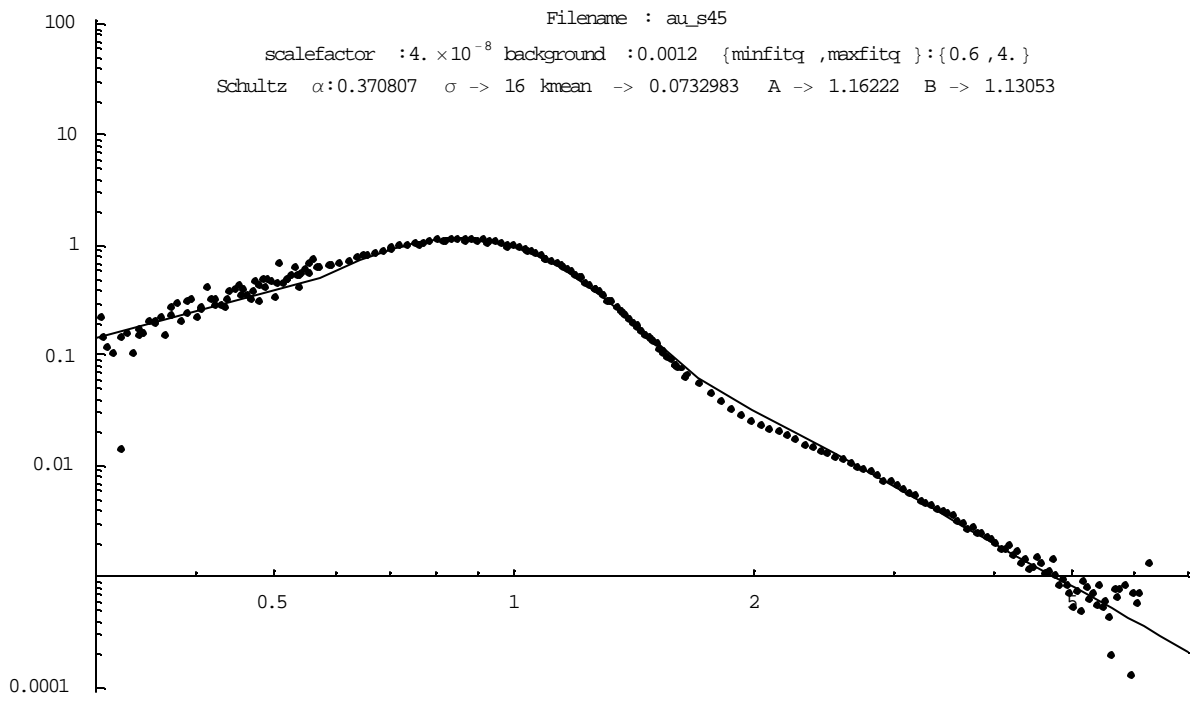
Ligament width = 6.15 nm

Figure A. 12 Ex-situ SANS data and the fit to that data for porous $\text{Ag}_{0.70}\text{Au}_{0.30}$. Ligament width was determined by Gaussian fit to ligament data (second curve). After the sample was dealloyed at 750 mV_{MSE} for 1.5 hours in 0.1 M HClO_4 , it was subjected to a coarsening potential of -600 mV_{MSE} in 0.5 M H_2SO_4 .



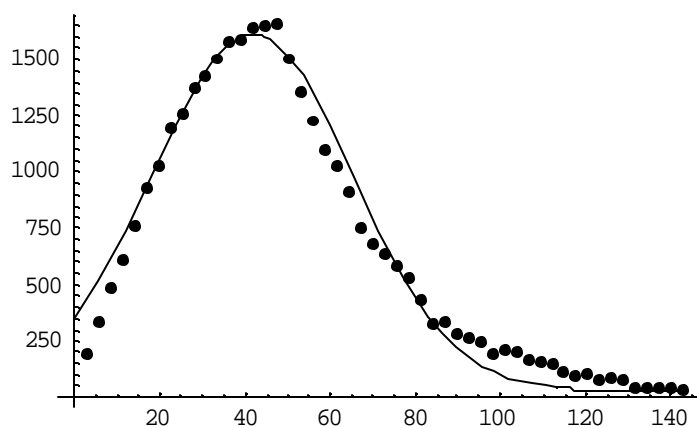
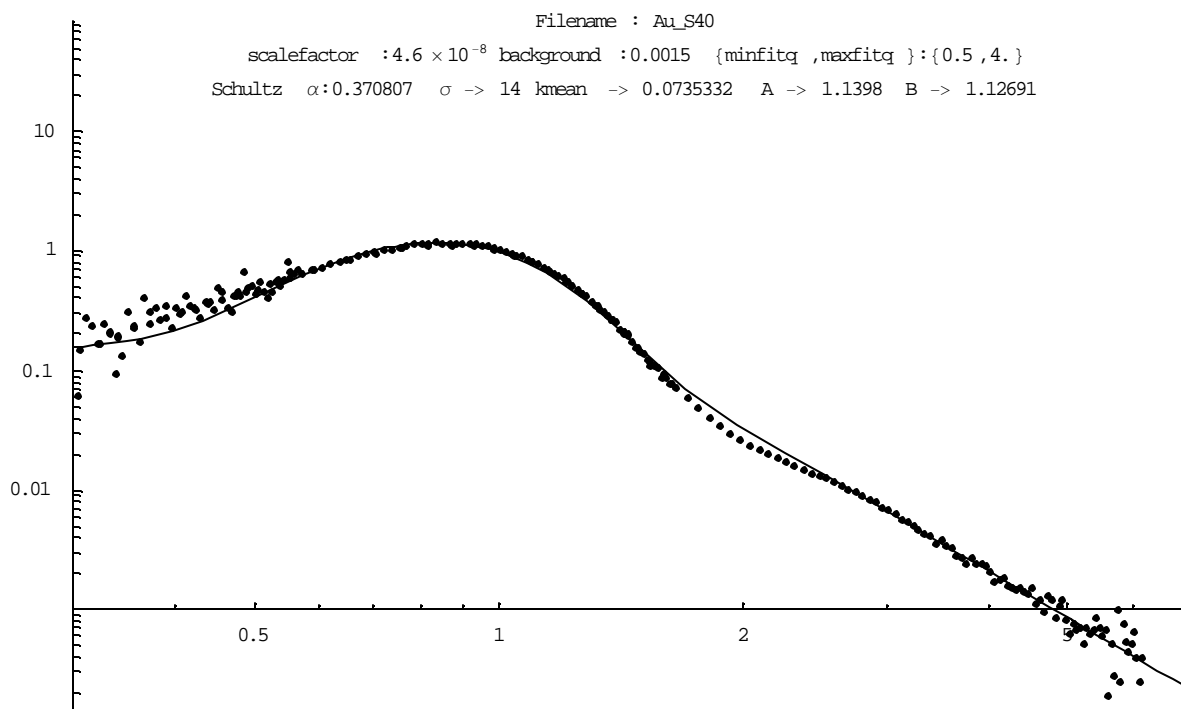
Ligament width = 5.24 nm

Figure A. 13 Ex-situ SANS data and the fit to that data for porous $\text{Ag}_{0.70}\text{Au}_{0.30}$. Ligament width was determined by Gaussian fit to ligament data (second curve). After the sample was dealloyed at 750 mV_{MSE} for 1.5 hours in 0.1 M HClO_4 , it was subjected to a coarsening potential of -420 mV_{MSE} in 0.5 M H_2SO_4 .



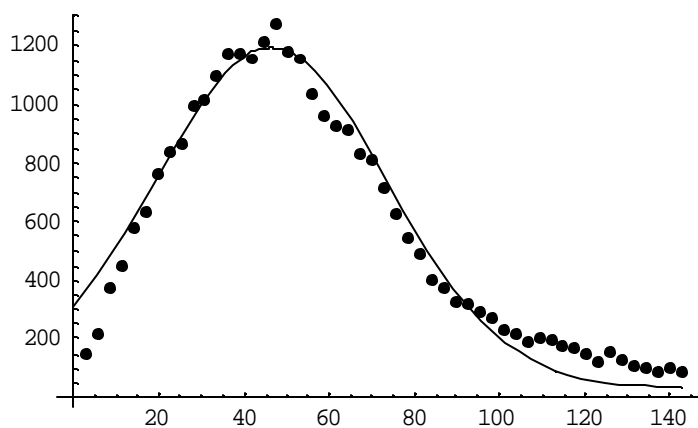
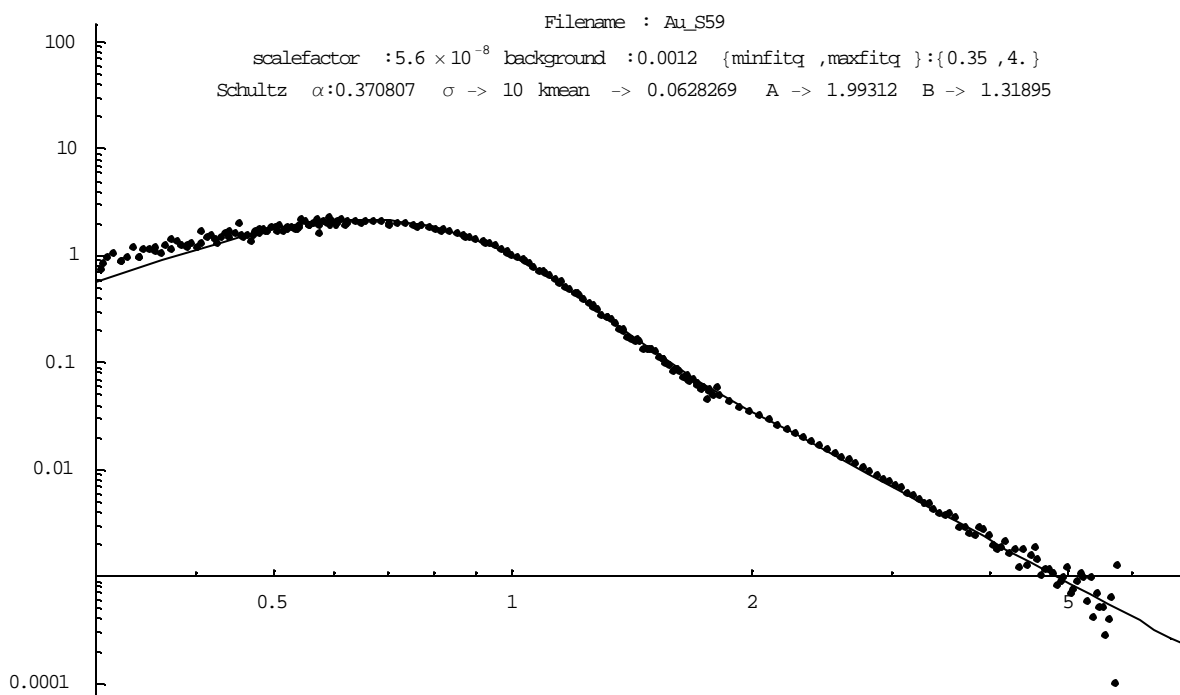
Ligament width = 4.36 nm

Figure A. 14 Ex-situ SANS data and the fit to that data for porous $\text{Ag}_{70}\text{Au}_{0.30}$. Ligament width was determined by Gaussian fit to ligament data (second curve). After the sample was dealloyed at 750 mV_{MSE} for 1.5 hours in 0.1 M HClO_4 , it was subjected to a coarsening potential of 90 mV_{MSE} in 0.5 M H_2SO_4 .



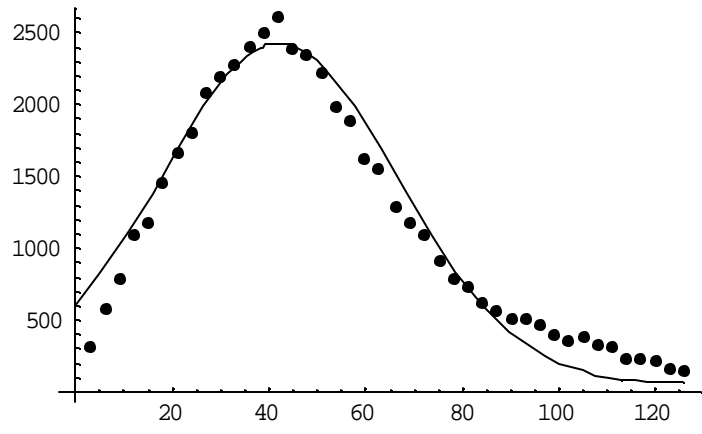
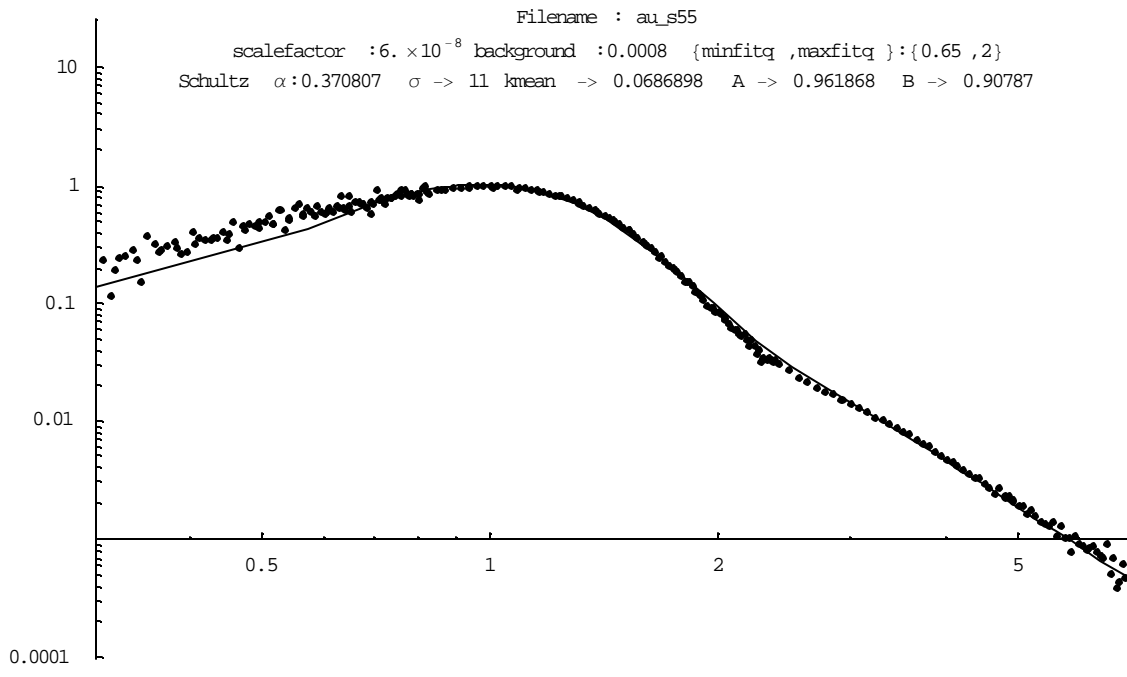
Ligament width = 4.17 nm

Figure A. 15 Ex-situ SANS data and the fit to that data for porous $\text{Ag}_{0.70}\text{Au}_{0.30}$. Ligament width was determined by Gaussian fit to ligament data (second curve). After the sample was dealloyed at $750 \text{ mV}_{\text{MSE}}$ for 1.5 hours in 0.1 M HClO_4 , it was subjected to a coarsening potential of $185 \text{ mV}_{\text{MSE}}$ in $0.5 \text{ M H}_2\text{SO}_4$.



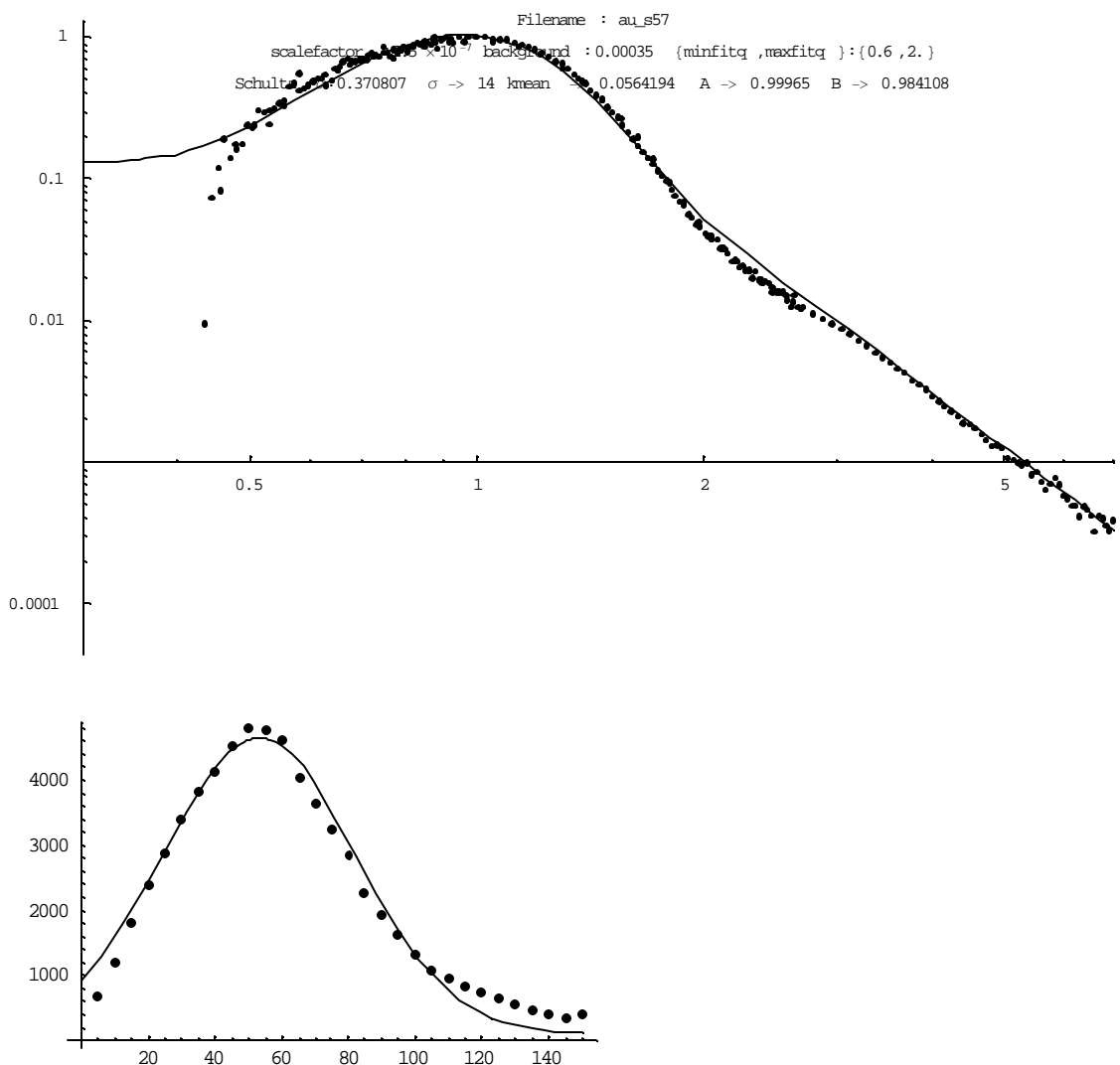
Ligament width = 4.63 nm

Figure A. 16 Ex-situ SANS data and the fit to that data for porous $\text{Ag}_{0.70}\text{Au}_{0.30}$. Ligament width was determined by Gaussian fit to ligament data (second curve). After the sample was dealloyed at $750 \text{ mV}_{\text{MSE}}$ for 1.5 hours in 0.1 M HClO_4 , it was subjected to a coarsening potential of $-600 \text{ mV}_{\text{MSE}}$ in 1 M HClO_4 .



Ligament width = 4.21 nm

Figure A. 17 Ex-situ SANS data and the fit to that data for porous $\text{Ag}_{0.70}\text{Au}_{0.30}$. Ligament width was determined by Gaussian fit to ligament data (second curve). After the sample was dealloyed at 750 mV_{MSE} for 1.5 hours in 0.1 M HClO₄, it was subjected to a coarsening potential of -420 mV_{MSE} in 1 M HClO₄.



Ligament width = 5.33 nm

Figure A. 18 Ex-situ SANS data and the fit to that data for porous $\text{Ag}_{0.70}\text{Au}_{0.30}$. Ligament width was determined by Gaussian fit to ligament data (second curve). After the sample was dealloyed at 750 mV_{MSE} for 1.5 hours in 0.1 M HClO₄, it was subjected to a coarsening potential of 185 mV_{MSE} in 1 M HClO₄.

VITA

Aziz Dursun was born in Ankara, TURKEY, on February 5, 1974. He graduated from Ankara High School in Ankara, TURKEY in 1991 with honors. He attended the Middle East Technical University in Ankara where he received the Bachelor of Engineering Science degree in the field of Metallurgical and Materials Engineering. In July, 1999 he received the Master of Science and Engineering degree in the same department. While a graduate student he received a scholarship from Baris Electric Ind. Company. He is currently a candidate for the Ph.D degree in Materials Science and Engineering at Virginia Polytechnic Institute and State University. He is a member of MRS.